



LIBRARY
Michigan State University

This is to certify that the

thesis entitled

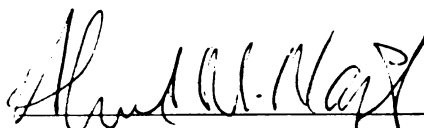
SIMULTANEOUS WALL-PRESSURE ARRAY AND PIV
MEASUREMENTS IN A SEPARATING/REATTACHING
FLOW REGION

presented by

Laura Michele Hudy

has been accepted towards fulfillment
of the requirements for

MS degree in Mechanical Engineering


Major professor

Date 8/23/01

PLACE IN RETURN BOX to remove this checkout from your record.
TO AVOID FINES return on or before date due.
MAY BE RECALLED with earlier due date if requested.

DATE DUE	DATE DUE	DATE DUE

ABSTRACT

SIMULTANEOUS WALL-PRESSURE ARRAY AND PIV MEASUREMENTS IN A SEPARATING/REATTACHING FLOW REGION

By

Laura Michele Hudy

SIMULTANEOUS WALL-PRESSURE ARRAY AND PIV MEASUREMENTS IN A SEPARATING/REATTACHING FLOW REGION

By

Laura Michele Hudy

AN ABSTRACT OF A THESIS

Submitted to
Michigan State University
in partial fulfillment of the requirements
for the degree of

MASTER OF SCIENCE

Department of Mechanical Engineering

2001

Professor Ahmed Naguib

ABSTRACT

SIMULTANEOUS WALL-PRESSURE ARRAY AND PIV MEASUREMENTS IN A SEPARATING/REATTACHING FLOW REGION

By

Laura Michele Hudy

A database of simultaneous wall-pressure array and particle image velocimetry (PIV) measurements was compiled for the investigation of the surface-pressure and the velocity signature of the structure within a separated/reattaching flow region. The experimental setup consisted of a long, splitter plate instrumented with an array of 80 flush-mounted microphones located within the wake of a fence. Data were acquired for two Reynolds numbers of 7885 and 10513, based on the fence height. Two distinctive regions, defined based on their location relative to the position of the mean reattachment point (x_r) of the shear layer, emerged from the spatio-temporal analysis of the surface pressure measurements. Upstream, from the fence to $\frac{1}{4}x_r$, the surface-pressure signature was dominated by large time scale disturbances and an *upstream* convecting velocity of $0.21U_\infty$. Beyond the $\frac{1}{4}x_r$, turbulent structures with small time scales and a downstream convection velocity of $0.57U_\infty$ generated most of the pressure fluctuations. There was evidence that these structures began to form around $\frac{1}{4}x_r$ and grew in strength and size with downstream distance before reattaching on the plate. Only the time-averaged results from the microphones at the lower Reynolds number have been examined hitherto and will be presented.

ACKNOWLEDGEMENTS

I would like to acknowledge the support of the Advanced Measurement and Diagnostics Branch at NASA Langley Research Center in Hampton, Virginia. The branch sponsored the grant for the Graduate Student Research Program, which enabled this research. I would also like to thank William M. Humphreys and Scott Bartram from the Advanced Measurement and Diagnostics Branch for all their support during this project.

Dr. Ahmed Naguib,
thank you

an

The

wh

an

all

ACKNOWLEDGEMENTS

I would like to acknowledge the support of the Advanced Measurement and Diagnostics Branch at NASA Langley Research Center in Hampton, Virginia. The branch sponsored the grant for the Graduate Student Research Program, which enabled this research. I would also like to thank William M. Humphreys and Scott Bartram from the Advanced Measurement and Diagnostics Branch for all their support during this project.

LIST OF TABLES	vii
LIST OF SYMBOLS	xii
1 INTRODUCTION	1
1.1 Background	1
1.2 Literature Review	2
1.3 Literature Review	8
1.4 Flow Control and Surface Measurements	21
1.5 Motivation and Objectives	24
2 EXPERIMENTAL SET-UP AND PROCEDURE	26
2.1 Experimental Set-up	26
2.1.1 Wind Tunnel Facility	26
2.1.2 Model	28
Fence	34
Instrument Plate	41
Middle Plate	42
Tail Plate	42
Endplates	43
2.1.3 Instruments for Measurement	46
Static Pressure System	46
Microphones	48
Particle Image Velocimetry	56
2.2 Experimental Procedure	56
2.2.1 Static Pressure System	56
Acquisition Time	56
Acquisition Time Delay	58
Alignment	59
2.2.2 Microphones	63
Cross Talk Check	63
Data Acquisition Parameters	64
Noise Cancellation Microphones	67

LIS

LIS

LIS

1

2

TABLE OF CONTENTS

LIST OF TABLES	vii
LIST OF FIGURES	viii
LIST OF SYMBOLS	xii
1 INTRODUCTION.....	1
1.1 Background	1
1.2 Canonical Geometries for Studying Separating/Reattaching Flows	2
1.3 Literature Review.....	8
1.4 Flow Control and Surface Measurements.....	21
1.5 Motivation and Objectives.....	24
2 EXPERIMENTAL SET-UP AND PROCEDURE.....	26
2.1 Experimental Set-up	26
2.1.1 Wind Tunnel Facility	26
2.1.2 Model	28
Fence	34
Instrument Plate	41
Middle Plate	42
Tail Plate	42
Endplates	43
2.1.3 Instruments for Measurement.....	46
Static Pressure System	46
Microphones	48
Particle Image Velocimetry	56
2.2 Experimental Procedure.....	56
2.2.1 Static Pressure System.....	56
Acquisition Time.....	56
Acquisition Time Delay	58
Alignment	59
2.2.2 Microphones	63
Cross Talk Check	63
Data Acquisition Parameters	64
Noise Cancellation Microphones.....	67

3

4

AP

AP

AP

AP

BIB

	Laser Noise	71
	Airfoil	74
	Base Microphone Run	77
	2.2.3 Data Collected	78
3	RESULTS AND DISCUSSION	80
3.1	Reattachment Length	80
3.2	Mean Pressure Distribution	82
3.3	Root-Mean-Squared Pressure Fluctuations	86
3.4	Auto-correlation Analysis	94
3.5	Power Density Spectra	103
3.6	Cross-Correlation with respect to measurements at reattachment.....	110
3.7	Phase, Coherence, and more on Convection Speeds.....	116
3.8	Inviscid Analysis on Vortical Structures in the Shear Layer	137
4	CONCLUSIONS AND FUTURE WORK	139
4.1	Conclusions.....	139
4.2	Future Work	142
APPENDIX A:	Microphone Coordinates	144
APPENDIX B:	Particle Image Velocimetry	145
B.1	Experimental Set-up	147
B.2	Experimental Procedure	151
	Synchronization of Microphone and PIV	151
	Dot Card	153
	Ruler.....	155
	Background Run	156
	Zero-Pulse Separation.....	157
APPENDIX C:	Microphone Contamination Testing	158
APPENDIX D:	Error Estimation for Integral Time scales.....	159
BIBLIOGRAPHY		162

LIST OF TABLES

1	Time series lengths tested and C_p values	57
2	Acquisition time values used to test convergence of C_p	66
3	Test matrix used for the experiment	78
4	Microphone matrix for microphone only tests – C = ADC channel and M = microphone number	79
5	Microphone matrix for microphone and PIV tests – C = ADC channel, M = microphone number, and T = Trigger	79
6	Microphone positions used in cross-correlation analyses	111
7	Convective velocities for various frequencies	125
8	Static pressure distribution for all three tested fences – model was not aligned in the test section at this point	38
9	Fence configuration used in experiment	39
10	Instrument plate lay-out consisting of microphones and static pressure taps	41
11	Tail plate used on the model; isometric view and side view	43
12	Spanwise reattachment lines reproduced from Castro and Haque (1987) – $x_{re} = x$, along the centerline	45
13	Circuit design used to control the spanwise	47
14	Typical WM-60A Frequency Response Curve – Panasonic data sheet	49
15	Schematic of the circuit used to drive the microphones and amplify the output signal	50
16	Actual circuit used to drive the microphones	50

19 Op-amp board used to drive the microphones – two microphones per op-amp circuit. (Twenty shown)	51
LIST OF FIGURES	
20 Microphone calibration unit	52
21 Distribution of microphone sensitivities	54
1 Typical separating/reattaching flow geometries and their ideal two-dimensional flow field: (a) backward-facing step, (b) blunt-face splitter plate, and (c) splitter plate with fence	3
2 Subsonic Basic Research (Wind) Tunnel at NASA Langley	27
3 Splitter-plate-with-fence configuration	29
4 Flow characteristics surrounding the splitter-plate-with-fence configuration: x_r = reattachment length	30
5 Flow field around backward-facing step - reproduced from Eaton and Johnston (1981)	31
6 Skeleton used to support the model and to house cables and tubes	33
7 Schematic of actual model	34
8 Dependence of reattachment distance on blockage ratio	35
9 The three fence configurations tested	37
10 Static pressure distribution for all three tested fences – model was not aligned in the test section at this point	38
11 Fence configuration used in experiment	39
12 Instrument plate lay-out consisting of microphones and static pressure taps	41
13 Tail plate used on the model: isometric view and side view	43
14 Spanwise reattachment lines reproduced from Castro and Haque (1987) – $x_{r0} = x_r$ along the centerline	45
15 Circuit design used to control the scanivalve	47
16 Typical WM-60A Frequency Response Curve – Panasonic data sheet	49
17 Schematic of the circuit used to drive the microphones and amplify the output signal	50
18 Actual circuit used to drive the microphones	50

19 Op-amp board used to drive the microphones – two microphones per op-amp circuit. (Twenty shown here).....	51
20 Microphone calibration unit.....	52
21 Distribution of microphone sensitivities.....	54
22 Distribution of microphone time delays.....	55
23 Mean pressure values at six different tested time series.....	58
24 Typical step response of the tubing/pressure transducer system.....	59
25 Vertical alignment of model in the tunnel in the streamwise direction.....	61
26 Check for two-dimensionality of the mean flow in the spanwise direction – $C_{p0} = C_p$ at x along the centerline.....	62
27 Power Spectrum sampled at 12,000 Hz for the microphone closest to reattachment.....	65
28 RMS pressure fluctuations – 5 different time series.....	67
29 Schematic showing position of noise cancellation microphones.....	68
30 Power spectra for microphone #0 with and without noise cancellation.....	70
31 Auto-correlation for microphone #0 without and with noise cancellation.....	71
32 Surface-pressure power spectra at microphones #2, 14, and 26.....	73
33 Static pressure data with and without airfoil in tunnel.....	75
34 Auto spectra of microphone data with and without airfoil.....	77
35 The pressure coefficient distribution for six different studies.....	81
36 Mean pressure distribution of present data.....	82
37 Mean streamwise pressure distributions for the current study compared to Castro and Haque (1987) and Cherry <i>et al.</i> (1984).....	83
38 Streamwise distribution of the coefficient of RMS pressure fluctuations.....	87
39 Surface-pressure RMS distribution in the spanwise direction.....	91
40 Comparison of the auto-correlation function computed in the time and frequency domain.....	96

41 Auto-correlation function for microphones # 0, 4, 7, 21, and 27	97
42 Contour map of the auto-correlation function for all 28 microphones along the centerline of the model	98
43 Streamwise variation of the integral time scale	101
44 Streamwise variation of the integral time scale	103
45 Power Spectra for microphones # 0, 4, 7, 21, and 27	105
46 Power Spectra in logarithmic form for the first 27 microphones along the centerline of the model – streamwise direction is from top to bottom.....	109
47 Power Spectra for selected microphones covering the measurement range - streamwise direction is from top to bottom.....	110
48 Cross-correlation results at five different locations	112
49 Cross-correlation color contour map for all 28 centerline microphones (reference microphone closest to reattachment)	114
50 Convection velocity plot for the cross-correlation contour plot from Figure 3.15	116
51 Coherence plot for four different microphones referenced to microphone #0	119
52 Coherence plot for four neighboring pairs of microphones.....	120
53 Streamwise development of the phase angle for five different frequencies (reference microphone at $x/x_r = 0.023$)	123
54 Phase angle plot at $f(2H)/U_\infty = 0.2$ with and without phase angle change due to systematic error	127
55 Cross-correlation color contour plot for all 28 (reference microphone at $x/x_r = 0.26$)	129
56 Cross-correlation color contour plot for all 28 (reference microphone at $x/x_r = 0.26$) – filtered data	130
57 Cross-correlation color contour plot for all 28 (reference microphone at $x/x_r = 0.023$)	131
58 Individual cross-correlation plots for the first 12 microphones (reference microphone $x/x_r = 0.26$) – filtered	132

59

60

61

62

63

64

65

66

67

68

69

70

71

72

73

74

75

76

77

78

79

80

81

82

83

84

85

59 Plot of positive-inclined-lobe peak locations from contour map in Figure 3.22	134
60 Microphones and static pressure tap dimension spreadsheet (all dimensions are in meters) – streamwise dimensions reference upstream edge of I-plate to center of microphone or tap hole and spanwise dimensions reference centerline of I-plate to center of microphone or tap hole (Mics = microphones and Taps = static pressure taps)	144
61 Example of set-up for a typical PIV system [Humphreys 2000]	146
62 Camera set-up used in experiment	148
63 Optics set-up used for PIV system	151
64 Flow regions captured by the two camera positions used	154
65 Sample of the dot card used to align the two pairs of cameras	154
66 Image of ruler used in calibration of PIV system	156
67 Parabola	159

f	frequency
f_s	sampling frequency
H	half the height of the fence
h	step height for backward-facing step configuration
h_f	fence height above the splitter plate
I	reverse-flow intermittency
i	record index
k	frequency index
K_{ms}	microphone sensitivity
k_t	time index
m	camera magnification for PIV images
m_{Δ}	slope
N	total number of points measured in a time record
n	time shift or delay index
n_{\max}	largest time shift or delay value
N_r	total number of records
p_r	reference mean pressure
p_s	surface mean pressure
P^*	FFT of p^* signal
p^*	sampled wall-pressure signal
p'^*_{RMS}	RMS of sampled signal
Re_h	Reynolds number based on step height
Re_{δ}	Reynolds number based on momentum thickness

LIST OF SYMBOLS

R_{xx}	normalized auto-correlation function
r_{xx}	auto-correlation function
R_{xy}	normalized cross-correlation function
r_{xy}	cross-correlation function
A	amplitude of traveling wave
b	$= 2\pi/\lambda$ = wave number
C	$\frac{1}{2}$ curvature of parabola
c	wave, or convection, speed
C_k	Discrete Fourier Transform coefficients in frequency domain
C_p	mean pressure coefficient
C_{p0}	mean pressure coefficient along centerline
C_p'	RMS pressure-fluctuation coefficient
$C_{p'0}$	RMS pressure-fluctuation coefficient along centerline
D	thickness of splitter plate
d	displacement vector for PIV analysis
D_t	half the height of the test section
E_{pp}	energy in B&K microphone pressure spectral peak
E_{vv}	energy in Panasonic microphone voltage spectral peak
f	frequency
f_s	sampling frequency
H	half the height of the fence
h	step height for backward-facing step configuration
h_f	fence height above the splitter plate
I_r	reverse-flow intermittency
j	record index
k	frequency index
k_m	microphone sensitivity
k_t	time index
m	camera magnification for PIV images
m_s	slope
N	total number of points measured in a time record
n	time shift or delay index
n_{max}	largest time shift or delay value
N_j	total number of records
p_r	reference mean pressure
p_s	surface mean pressure
P'	FFT of p' signal
p'	sampled wall-pressure signal
p'_{rms}	RMS of sampled signal
Re	Reynolds number based on step height
Re_θ	Reynolds number based on momentum thickness

R_{CD}
 r_{CD}
 $R_{\text{CD},\text{CD}}$
 $r_{\text{CD},\text{CD}}$
 t
 U_z
 U_x
 V
 W
 x
 x_i
 x_{CD}
 y
 z

 $\tilde{\alpha}_i$
 θ_{CD}
 $\theta_{\text{CD},\text{CD}}$
 θ
 γ
 η
 λ
 τ
 τ^*
 v
 θ
 ρ
 ΔT
 Δz
 \emptyset
 $\Gamma_{\text{CD},\text{CD}}$
 \vdots
 \vdots

$R_{p'p'}$	normalized auto-correlation function
$r_{p'p'}$	auto-correlation function
$R_{p'1p'2}$	normalized cross-correlation function
$r_{p'1p'2}$	cross-correlation function
t	time
U_c	convection velocity
U_∞	free stream velocity
V	velocity vector
W	width between endplates
x	streamwise distance along splitter plate
x_r	reattachment length
x_{ro}	centerline reattachment length
y	normal distance from the splitter plate
z	spanwise direction
δ_s	boundary layer thickness
$\phi_{p'p'}$	power spectrum of p'
$\phi_{p'1p'2}$	cross spectrum of p'_1 and p'_2
Θ	momentum thickness
γ	$= [4\phi_{p'p'}(2H)]/[p'^2 U_\infty^5]$
η	$= \tau U_\infty / 2H$
λ	wavelength
τ	$= n/f_s =$ time shift
τ^*	time delay between two negative peaks in auto-correlation function
ν	kinematic viscosity
θ	phase angle
ρ	fluid density
ΔT	laser pulse separation
$\Delta \tau$	change in time delay
ω	$= 2\pi f =$ wave angular frequency
$\Gamma_{p'1p'2}$	coherence
ξ	$= (x - x_r)/x_r$

real

met

tech

com

pre

rang

des

com

de

perf

sur

wing

dep

the

take

that

air

for

1 INTRODUCTION

1.1 Background

For many years, researchers have studied the physics of separating and reattaching flows created by various geometries utilizing flow visualization methods, velocity and surface pressure measurements, and shear stress techniques to name a few. The physics of this particular class of flows is complicated, thus making the quantitative details of the flow challenging to predict. Separating/reattaching flows are found in a variety of applications ranging from aircraft flight, to building construction, to muffler and air conditioning design, to automobile aerodynamics. Predicting the flow characteristics in these complex applications can lead to improvement in component design and to the development of control techniques that change the flow state to enhance the performance of devices.

A good example of the advantage of being able to predict the flow pattern and therefore are more difficult to analyze. Three simple models typically used surrounding an object during changing conditions is the wing of an airplane. The wing is a complex geometry that has a variable flow state above the surface depending on flight conditions. That is, the flow separation on the suction side of the wing changes its location as the plane navigates through the air, including take-off and landing. Separation along the wing produces a low-pressure wake that increases drag and reduces lift, thus requiring more energy to maneuver the aircraft, or allowing a smaller payload. Being able to predict separation allows for the adjustment of the wing geometry, which, in turn reduces the effect of the

wake

des

or a

iden

utic

red

veh

sep

pre

con

per

1.2
Flo

sep

and

the

blu

the

ge

Fig

ten

Sym

wake. Another example can be seen in building construction and in automotive design. In both cases, separated flows can produce vibrations that cause fatigue or audible disturbances. Therefore, it is pertinent to study these flows in order to identify characteristics that can be used both to predict flow conditions and ultimately to control the flow. Controlling separated flows can enhance lift and reduce drag in aircraft as well as minimize vibrations and acoustic noise in vehicles and in buildings, amongst many other benefits. Hence, researching separated/reattaching flow geometries can provide useful information not only for predicting the flow and related heat, mass, and momentum transport but also for controlling the flow conditions, resulting in characteristic improvement in performance.

1.2 Canonical Geometries for Studying Separating/Reattaching Flows

Over the years, several geometries have been used to generate and study separating/reattaching flow regions. Some are more complicated than others and therefore are more difficult to analyze. Three simple models typically used when studying separating/reattaching flows include the backward-facing step, the blunt-face splitter plate, and the splitter plate with fence. These geometries have the advantage of possessing a well-defined separation point. The three geometries and typical, average, flow patterns above the surface are shown in Figure 1.1. The flow features among the three geometries vary only slightly in a few areas such as the separation angle, reattachment length, and flow symmetry. Generally, for all three models, the flow separates from the model at

the

reatt.

char

along

the f

the sharp edge of the step, corner, or fence, creating a shear layer that reattaches at some point farther downstream. Beneath the shear layer there is a characteristic re-circulation region, as it reaches the sharp edge of the step. At

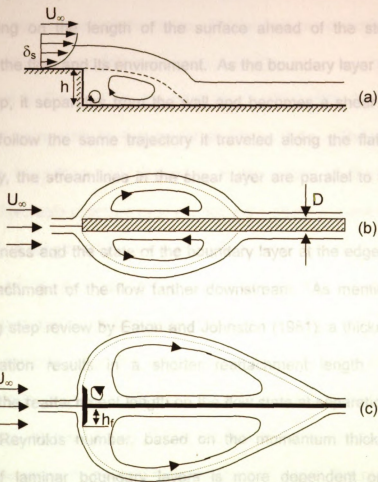


Figure 1.1 Typical separating/reattaching flow geometries and their ideal two-dimensional flow field: (a) backward-facing step, (b) blunt-face splitter plate, and (c) splitter plate with fence

Starting with the backward-facing step (Figure 1.1a), the free stream flows along the top surface of the step creating a boundary layer due to the viscosity of the fluid and the 'no-slip' condition at the wall. The boundary layer is

char

wall

layer

this

state

distu

edge

layer

there

sepa

affec

back

layer

depe

relate

reac

num

the

reat

regio

of the

characterized by a steep, velocity gradient causing high shear stresses on the wall. Growing in thickness as the flow moves across the top part of the step, the layer has a definite thickness (δ_s) as it reaches the sharp edge of the step. At this point, the layer may be laminar, turbulent, or in transition between the two states, depending on the length of the surface ahead of the step and the disturbances in the flow and its environment. As the boundary layer reaches the edge of the step, it separates from the wall and becomes a shear layer. The layer tends to follow the same trajectory it traveled along the flat plate; and therefore initially, the streamlines in the shear layer are parallel to the plate at separation.

The thickness and the state of the boundary layer at the edge of the step affect the reattachment of the flow farther downstream. As mentioned in the backward-facing step review by Eaton and Johnston (1981), a thicker boundary layer at separation results in a shorter reattachment length. Also, the dependence of the reattachment length on the flow state at separation is directly related to the Reynolds number, based on the momentum thickness. The reattachment of laminar boundary layers is more dependent on Reynolds number than turbulent boundary layers [Eaton and Johnston 1981]. Increasing the Reynolds number within the laminar region causes an increase in the reattachment length, whereas, increasing the Reynolds number in the turbulent region has no effect on the reattachment distance.

Finally, once the flow separates, vortical structures begin to form because of the instability of the shear layer. These structures grow in strength and size

as th

Beyo

and i

There

bubb

also

seca

appr

Beca

short

point

gene

distan

region

intern

using

al/ (1\$

althou

stude

attach

the fe

as they move downstream and are strongest at the point of reattachment. Beyond reattachment, the structures diffuse and decay. Beneath the shear layer and its convective vortices there is a re-circulating region as seen in Figure 1.1a. There is also another separation point associated with a secondary re-circulating bubble in the corner just behind the fence. Similar features described here are also seen in the other two models.

The model in Figure 1.1b, the blunt-face splitter plate, has a different separation point compared to the model in Figure 1.1a. The free stream approaches the blunt-face and separates at the edges of the front face. Because of the favorable pressure gradient along the blunt-face and the typically short development length ($D/2$), the boundary layer is thin at the separation point. Similar to the backward-facing step, the resulting thin shear layer generates turbulent structures that grow in strength and size with downstream distance before reattaching on the splitter plate. There is also a re-circulating region formed under the separation bubble. By calculating the reverse-flow intermittency (I_r equals the fraction of time the flow is in the upstream direction) using the discrete-vortex model and measuring I_r with a split film probe, Kiya *et al.* (1982 and 1983) suggested the formation of a secondary, separation bubble; although, evidence of this is difficult to find in other blunt-face-splitter-plate studies.

Finally, the model shown in Figure 1.1c is the splitter plate with a fence attached perpendicular to the plate. The splitter plate is parallel to the flow, and the fence is perpendicular to the flow. As with the blunt-face plate, a favorable

pres

laye

dist.

vibra

with

a tra

bag

struc

reat

deve

assoc

prev

boun

geor

This

exan

dista

step

to th

step

mea

and

pressure gradient on the front face of the fence results in a thin, laminar shear layer at separation. The shear layer is highly unstable, and the slightest disturbance can cause it to become turbulent. These disturbances could be from vibrations in the tunnel, acoustic noise, free stream turbulence, and/or interaction with the wall at reattachment. Between the laminar and turbulent stages, there is a transition state where the disturbances start to affect the shear layer. At the beginning of transition, low-energy structures start to form. The energy of these structures amplifies, and they grow in size as they convect downstream before reattaching on the splitter plate. Beneath the shear layer, a re-circulating region develops; and as in the backward-facing step, a second separation point and associated re-circulating region form.

There are slight differences among the three geometries. For example, as previously explained, the backward-facing step flow state is affected by the boundary layer conditions at separation. This is not the case in the other two geometries where a thin shear layer forms at separation instead of a thick one. This layer is substantially smaller than the overall scale of the flow field, for example, the fence height. Another example concerns the reattachment distance. With the backward-facing step, the reattachment length divided by the step height is shorter compared to the other two geometries. This could be due to the angle of the separation streamline from the edge. On the backward facing step, the flow separates parallel with the plate and the incoming flow. This means that the peak height of the separation bubble is at the point of separation and beyond that point the shear layer bends downward toward the wall until it

realt:

90° t

short

realt:

betw

(nom

2H v

sepa

fence

know

the p

mode

short

plate

geom

which

flow

must

flow o

while

from

reattaches. In the other two geometries, the near-wall separation streamline is 90° to the splitter plate and to the incoming flow, reaching a peak height at a short distance downstream of separation and then curving toward the reattachment point. This causes the difference in the reattachment lengths between model (a) on one hand and models (b) and (c) on the other.

Between models (b) and (c), reattachment on the blunt-face splitter plate (normalized by D) is shorter than on the splitter plate with fence (normalized by $2H$, which is the total height of the fence). The reason being that once the flow separates on the blunt-face model, it is closer to the splitter plate wall than in the fence/splitter plate model. In model (c), the flow separates from the fence at a known distance above the splitter plate. Since the separation occurs closer to the plate in model (b) than in model (c), it is expected that the shear layer in model (b) would reattach before the shear layer in model (c) because it has a shorter distance to travel before impinging on the plate. As a result, the splitter plate with fence model will have the longest reattachment length out of the three geometries. Finally, flows for models (b) and (c) are symmetric top and bottom, which is not the case in backward-facing steps. As a result, the symmetry of the flow surrounding the blunt-face splitter plate and the splitter plate with fence must be checked prior to collecting data.

The advantages of these simple types of geometries are that they create flow characteristics similar in nature to what is seen in more complex geometries while providing a more controllable setting. These simple geometries have a known separation point and a mean flow field that is fairly well documented in

the l
due
sepa
use
influ
sepa
also
desc
in th

1.3

spitt
of co
geon
a nu
This
reve
fence
class

cara
and e
their

the literature. Instantaneous characterization, however, of the flow is challenging due to the complexity of the flow structures produced by the three simple separating/reattaching flow models. The splitter plate with fence model was used in this study because it has the longest reattachment length, minimal influences of the boundary layer details at separation on the flow field, known separation point, and rich flow characteristics. Ruderich and Fernholz (1986) also used the splitter plate with fence configuration for the same reasons described. They were the first researchers to scrutinize the flow structure details in this geometry.

1.3 Literature Review

As will be seen later, the present study makes use of the fence-and-splitter-plate geometry to establish a separated/reattaching flow for the purpose of collecting surface pressure measurements beneath the flow. Because this geometry is one of the classic separating/reattaching flow geometries, there are a number of studies that have characterized the flow surrounding this model. This is also true for the other two geometries described. Hence, studies reviewed here will be limited to those pertaining to either a splitter-plate-with-fence geometry, or unsteady, surface-pressure measurements in the other two classical configurations.

Aire and Rouse (1956) studied the two-dimensional flow over a series of parallel fence-with-splitter-plate models in a uniform flow using computational and experimental techniques in an attempt to model the separation bubble. In their studies, they were able to determine an approximate pattern of the

stre

the

to n

Ran

reg

Are

fals

fas

equ

wal

How

mot

arc

anal

of th

on th

split

Fig

distr

Proc

date

featu

streamlines surrounding the fence, identifying the dividing streamline between the shear layer and the re-circulating region. From this analysis, they attempted to model the flow surrounding the plate using potential flow theory over a Rankine oval. The Rankine oval represented the standing eddy, or re-circulation region, seen in the characterization of the streamlines surrounding the fence. Arie and Rouse (1956) used the results from the potential-flow analysis to add falsework to the walls of the test section. These pieces curved in the same fashion as the streamlines produced by the model and were placed at a distance equal to the calculated, boundary-layer-displacement thickness at the tunnel walls in an effort to remove the boundary layer and its effects on the flow. However, because the falsework was designed based on the assumption of irrotational flow, the tunnel did not simulate infinite-flow-domain conditions around the plate as originally presumed. They attributed this to the potential flow analysis that did not take into account the wake farther downstream at the edge of the standing eddy (re-circulation zone), where turbulence is prominent.

Smits (1982) looked at a number of kinematic conditions and their effect on the time-average characteristics of a separation bubble, created by placing a splitter plate in the wake of a two-dimensional bluff body (similar to that seen in Figure 1.1c). Static pressure taps were used to determine the mean pressure distribution along the splitter-plate surface, and a Pitot tube and a disc static probe were used to measure the velocities and pressures within the separation bubble. Smits (1982) examined the relationship between blockage ratio and reattachment length based on the step height. Step height, h_r , is the height of

the t

heig

mea

This

woul

dista

sp'it

Rous

to be

was

conc

by le

50%

effec

betwe

rever

press

plate

meas

lapan

dimer

the bluff body above the splitter plate. The blockage ratio is defined as the step height divided by half the height of the test section, h_f/D_t . A large blockage ratio means the distance between the bluff body and the test section ceiling is small. This causes an increase in the acceleration of the flow around the fence, which would shift the reattachment length.

Smits (1982) found that as the blockage ratio increased, the reattachment distance decreased (shown in Figure 2.7). He also investigated the effect of the splitter plate length on the flow, confirming work previously done by Arie and Rouse (1956). According to Arie and Rouse (1956), the splitter plate needs only to be 10 times the total height of the fence, as further lengthening of the plate was found to have no effect on flow conditions. Smits (1982) reaffirmed this conclusion showing the reattachment distance to be the only parameter affected by lengthening the splitter plate. For example, increasing the plate length by 50% resulted in a 7% increase in the reattachment length, which is a fairly small effect. It was also stated in the paper by Smits (1982) that there was a balance between the turbulent eddies in the shear layer moving downstream and the reversed flow in the re-circulating zone. This balance created the mean-pressure distribution observed around the model.

Castro and Haque (1987) studied the turbulent shear layer in a splitter-plate-with-fence configuration using static pressure and skin-friction measurements and pulse-wire anemometry. In their study, they outlined parameters for designing and building a splitter-plate-with-fence model. All their dimensions were normalized by the step height or the total height of the fence,

2H. The total fence height is defined as twice the step height plus the thickness of the splitter plate. Castro and Haque (1987) determined the blockage ratio for their model based on the study done by Smits (1982). However, they did suggest adding sideplates to the model in order to improve the two dimensionality of the flow by creating a new boundary layer that was thinner than the one formed on the walls of the test section. Castro and Haque (1987) showed that a model with a small aspect ratio and endplates has better two dimensionality than a model with a larger aspect ratio and no endplates. Moreover, the length of their splitter plate was $35H$, where H is half the height of the fence.

In a low-turbulence-intensity wind tunnel and at a Reynolds number based on the total fence height of 2.3×10^4 , Castro and Haque (1987) characterized the mean, static-pressure distribution over the splitter plate, finding the minimum pressure around $0.5x_r$. Although they do not attempt to explain this, they do state that the mean pressure distribution is invariable with Reynolds number. Through velocity autocorrelations and associated integral time scales, Castro and Haque (1987) identified a low frequency motion that had a larger time scale than eddies in the shear layer. From this analysis, they found the velocity field to be dominated by large time scales up to about $0.4x_r$ and farther downstream shorter time scales dominated the flow. These large time scales, which were most noticeable near separation, were attributed to the 'flapping' of the shear layer. Also normal and shear Reynolds-stress measurements suggested a 'positive feedback' system within the flow. That is, at reattachment, fluid mass is

return

layer

This

Haqu

mean

reatta

confi

Haqu

strea

and h

on fe

aroun

deter

17 2-

reatta

reatta

reatta

subst

whicn

region

Withn

returned upstream in the re-circulation bubble and re-entrained into the shear layer, which accounts for the vertical, Reynolds stress-component amplification. This amplification was not seen in the spanwise component. Finally, Castro and Haque (1987) found that the shear layer reached a height of $2h_f$; although the mean shear layer streamline had a height of approximately $1.5h_f$. Their reattachment point was at $19.2h_f$ downstream of separation.

Ruderich and Fernholz (1986) also studied a fence with splitter plate configuration but did not observe the flapping frequency described by Castro and Haque (1987). Ruderich and Fernholz (1986) characterized the flow in the streamwise and spanwise directions using oil-flow, surface-streaking pictures and hot- and pulsed-wire anemometry at a Reynolds number of 1.4×10^4 , based on fence height. From the oil-flow pictures, they confirmed the flow symmetry around the model in both the streamwise and spanwise directions and determined the centerline reattachment length of the shear layer to be $17.2 \pm 0.5h_f$. They stated there were two possible reasons for the wide reattachment region: (1) large structures impinging on the splitter plate at reattachment, or (2) the flapping of the shear layer. Near the walls, the reattachment length was reported to be $15h_f$. This demonstrated evidence of substantial three-dimensional effects off the centerline of the flow geometry, which did not have endplates.

Additionally, Ruderich and Fernholz (1986) identified the re-separation region (See Section 3.2 for details) to be within $2.3h_f$ downstream of the fence. Within this region, corner vortices were observed near the sidewalls. These

von

tun

me

ge

pla

bas

3.2

spa

to

don

fun

ana

don

The

incor

reac

reac

gro

wea

sm

was

vortices had little angular velocity but directed the fluid downstream along the tunnel side wall. on the face of the splitter plate). Cherry *et al.* (1984) do not
Cherry *et al.* (1984) made two-point unsteady surface pressure measurements in a separating/reattaching flow region. Their test model geometry was a blunt-face splitter plate, which is similar in nature to the splitter-plate-with-fence geometry. The Reynolds number used in the experiment was based on the thickness of the splitter plate and was held within the range of $3.2 \times 10^4 \pm 0.2 \times 10^2$. Cherry *et al.* (1984) used two microphones set at different spacings along the centerline and in the spanwise direction of the model in order to record the unsteady pressure measurements. A time-averaged analysis was done on these data in terms of RMS fluctuating pressures and cross correlation functions in the streamwise and spanwise directions along with a frequency analysis using power spectra. Instantaneous smoke flow visualization was also done simultaneously with measurements of the fluctuating pressure and velocity. The RMS surface-pressure analysis revealed that the time varying pressure increased in the downstream direction, reaching a peak in the vicinity of reattachment, followed by a gradual decrease farther downstream of reattachment. of three-dimensional effects in the spanwise direction because the

Cherry *et al.* (1984) attributed the increase in fluctuating pressure to the growth of turbulent structures in the shear layer. These structures were initially weak near separation but were strongest near reattachment. Furthermore, using smoke flow visualization, the formation of vortical structures in the shear layer was seen to start around 0.3 times the thickness of the splitter plate, D . This is

upstr

(abou

comm

down

Chern

from

was

positi

the c

move

conve

proce

the p

respe

shear

Finally

was n

reatta

state

scales

proces

upstream of the point where the RMS wall-pressure fluctuations start increasing (about one D from the face of the splitter plate). Cherry *et al.* (1984) do not comment on the reason for this discrepancy. The convective nature of the surface-pressure imprint associated with the downstream motion of the shear layer structures was also demonstrated by Cherry *et al.* (1984) through the cross-correlation analysis between two signals from microphones spaced apart in the streamwise direction. One microphone was fixed near the reattachment and the other was moved to five different positions from upstream to downstream of the fixed microphone. The peak in the cross-correlation function was seen to shift to smaller time delay as the movable microphone was traversed in the downstream direction, indicating the convective nature of the flow structure dominating the wall-pressure generation process. Cherry *et al.* (1984) also observed low- and high-frequency peaks in the power spectrum measured close to separation and near reattachment, respectively. They attributed the low-frequency signature to the flapping of the shear layer associated with the growth and decay of the separation bubble. Finally, it is worth noting that the flow field investigated by Cherry *et al.* (1984) was not free of three-dimensional effects in the spanwise direction because the reattachment line was curved slightly. The flow reached a three-dimensional state shortly after separation; however, they observed that the larger shear-layer scales were free of the 'three-dimensionalizing' effects of the reattachment process. The measurements of Farabee and Casarella (1986) were

sim

the

con

sub

191

fac

sub

bee

the

use

me

are

for

con

cha

sep

late

pre

she

flu

at

Qualitatively, the backward-facing step flow, as explained earlier, has similar flow characteristics to the splitter plate with fence geometry. As a result, the present study was also compared to studies concerned with the back step configuration because these studies provided more information regarding surface pressure measurements within a separating/reattaching flow region. In 1981, Eaton and Johnston reviewed the research done on the classic backward-facing step geometry in effort to summarize the data available at the time and to suggest areas worth investigating. Most of the studies up until that time had been conducted using hot-wire, pulsed-wire, and laser anemometry. Since then there have been a good number of studies in this classic geometry that have used more current techniques such as surface pressure sensors and particle image velocimetry (PIV). Of these, the ones containing surface-pressure data are summarized below.

Farabee and Casarella (1986) studied fluctuating wall pressures in a forward-facing and backward-facing step using a flush-mounted B&K 1/8in. condenser microphone to measure the surface pressure fluctuations. They characterized the backward-facing step as having an "attached shear layer" that separates from the step at the edge and reattaches on the wall a short distance later. From the RMS turbulent pressure values, they observed the surface pressure fluctuations to rise rapidly with increasing streamwise distance as the shear layer structures grew in strength and moved downstream. These fluctuations reached a maximum as the flow impinged on the surface of the plate at reattachment. The measurements of Farabee and Casarella (1986) were

con

val

ed

de

alo

en

con

ma

as

spe

don

Ca

be,

he

de

sep

te

con

pa

Bo

compared to an equilibrium flat plate boundary layer flow. The measured RMS values at reattachment were 5 times larger than those measured in the equilibrium flow farther downstream.

Using frequency domain analysis, Farabee and Casarella (1986) described the characteristics of the wall-pressure field as variable with x distance along the wall. Close to separation, the spectra showed the highest level of energy at very low frequencies; whereas, farther downstream the spectrum containing the largest energy was found at reattachment. This was a manifestation of the increase in the energy of the organized, turbulent structures as the flow convected downstream. A corresponding shift was seen in the spectrum as the dominance of the low-frequency disturbances gave way to the dominance of the high-frequency structures downstream. Farabee and Casarella (1986) also stated that the energized structures diffused and decayed beyond reattachment; however, these structures were still identifiable 72 step heights downstream of the step.

Finally, convection velocity analysis at different positions along the model downstream of the step showed that the pressure fluctuations close to separation were associated with the re-circulating low-speed fluid and not the high-speed fluid in the shear layer. However, Farabee and Casarella (1986) commented that the convection velocity was *always* in the downstream direction, indicating that the pressure fluctuations were not originating from the reverse flow within the re-circulating bubble.

back

shea

type

rese

they

conti

length

the e

They

of ± 1

show

cent

frequ

a po

could

engu

to m

would

ayer

close

high-p

Driver *et al.* (1987) identified two types of fluctuating motion in their backward-facing step study of the time-dependent character of the separated shear layer at a Reynolds number of 37,000, based on the step height. The first type was the flapping of the shear layer that has been identified by many researchers and the second was a quasi-periodic vortical type motion, which, they stated, needed further investigation. Driver *et al.* (1987) noticed abnormal contraction and elongation of the separation bubble due to the shortening and lengthening of reattachment length. This was labeled as the flapping motion of the shear layer with amplitude estimated to be 20% of the shear layer width. They also found the direction of the flow to change intermittently over the range of ± 1 step height from the reattachment point. Surface-pressure measurements along with velocity measurements showed that there was a definite low frequency disturbance in the flow, but that it contributed very little energy to the overall pressure fluctuations. This low frequency was associated with the shear layer flapping. Driver *et al.* (1987) gave a possible explanation for the flapping motion of the shear layer, stating that it could be caused by a vortical structure with enough momentum to escape being engulfed by the separation bubble at reattachment. This might cause the bubble to momentarily collapse because fluid mass supplied to the re-circulating region would be temporarily lost. The collapse would change the shape of the shear layer and the length of the reattachment. The reattachment point would move closer to the separation point causing more curvature of the shear layer and a high-pressure gradient at reattachment. This increased pressure gradient would

ca.
spe
be
pe
he
the
ass
do
circ
at
the
che
for
and
sig
loc

bac
and
con
he
Exc

cause the bubble to inflate again as it would hinder the advancement of the low-speed fluid. The vicinity of reattachment, decaying beyond that point. Pressure

spectr Heenan and Morrison (1998) investigated wall-pressure fluctuations behind a rearward-facing step and passive control of these fluctuations using a permeable surface (at Reynolds number equal to 1.9×10^5 based on the step height). A particularly interesting feature of Heenan and Morrison's study is that they were able to remove the low-frequency surface-pressure signature associated with shear-layer "flapping" by using the permeable surface placed downstream of the step. They attributed this success to inhibiting the recirculating flow responsible for the upstream convection of disturbances formed at reattachment. Although the characteristics of the measured wall-pressure in the non-permeable case were consistent with that summarized earlier in this chapter, one difference existed. More specifically, Heenan and Morrison (1998) found an *upstream* convection velocity close to separation using phase-angle analysis. They identified negative phase angles (with respect to a microphone signal measured immediately behind the step) at low frequencies and at locations from separation up to $0.4x$, in the impermeable case. point Employing

Point Lee and Sung (2001) used a 32-microphone array downstream of a backward-facing step to measure wall-pressure fluctuations in the streamwise and spanwise directions. Spatio-temporal statistics were completed on this comprehensive data set for a Reynolds number of 33,000, based on the step height. Lee and Sung (2001) observed the same phenomenon in their experiment as experienced by earlier investigators of backward-facing step

studies. The RMS pressure fluctuations rose sharply starting around $0.5x$, and peaked in the vicinity of reattachment, decaying beyond that point. Pressure spectra revealed low-frequency dominance close to separation, presumably due to the flapping of the shear layer. Farther downstream, the spectra were dominated by high-frequency components. In terms of the convection velocity, Lee and Sung (2001) calculated a downstream convection velocity of $0.6U_\infty$ at high frequencies and they did not find evidence of an upstream convection velocity. Although from their phase plot, used to determine the convection velocity, there were many singularities (phase discontinuities) at low frequencies. This was not the case at the higher frequencies.

Most recently, Spazzini *et al.* (2001) concentrated their investigation on the low-frequency motion identified in their backward-facing step. In their experiment, using a technique called Forward Flow Probability from skin friction measurements, they observed two important areas beneath the shear layer: (1) the mean reattachment point and (2) a secondary, separation point. Similar to wall-pressure fluctuations, the maximum of the streamwise skin-friction RMS distribution was found slightly upstream of the reattachment point. Employing Fourier analysis, 75% of the total energy in the wall-shear spectra was found to be contained at low frequencies at the location starting from in the vicinity of the step up to 0.4 of the reattachment distance. Farther downstream, this same frequency range contained only 30% of the total energy. At this position, the spectra were dominated by higher frequencies.

mo

fre

nyl

exp

re-

the

of

mo

fro

wit

oth

Thi

rea

sep

for

ge

ste

re

ai

sec

Using a wavelet transform for more detailed analysis of the low frequency motion, Spazzini *et al.* suggested that at a comparable frequency to the flapping frequency there was intense activity in the secondary re-circulation bubble. This hypothesis was examined further using PIV measurements in a water-tunnel experiment. Based on these measurements, it was proposed that the secondary re-circulation bubble was the cause of the low-frequency motion as described in the following paragraph.

Starting at reattachment, the flow was displaced in two directions as part of the flow moved downstream to form a boundary layer and the other part moved upstream to form a re-circulating region. Near the step, the reversed flow from the re-circulation bubble was then divided into two parts. One part stayed with the re-circulation bubble and became part of the shear layer again, and the other part impinged on the wall of the step at a secondary reattachment point. This point fluctuated within 0.7 and 0.9 H (height of the step). At this second reattachment point the flow split into two parts again: (1) that entrained by the separated flow at the step and (2) that directed toward the base of the step forming a vortex. This vortex formed the secondary re-circulation bubble and grew in size and strength until the height of the bubble was comparable to the step height. At that point, or soon after, the bubble experienced break down and the cycle was repeated. It should be noted that although the study of Spazzini *et al.* (2001) did not include wall-pressure measurements, it was summarized here because it offers an interesting hypothesis concerning the origin of the low-

frequency unsteadiness as well as the possible significant role of the recirculation flow in causing these fluctuations.

1.4 Flow Control and Surface Measurements

Controlling separating/reattaching flows is important to the performance of several flow systems as previously explained. Flow control changes the flow conditions surrounding a particular geometry and can be used, for example, to prevent flow separation or to reduce the separation bubble size (e.g., Kiya *et al.* (1999)). Therefore, flow control can be used to optimize the flow state around a defined geometry and as will be seen later, is one of the motivations behind this study.

Research in the area of flow control is relatively new. Over the past decade, however, researchers have been successful in manipulating flows in separating/reattaching flow geometries, with the most effective technique being periodic excitation of the shear layer at the point of separation (Wynanski (1997)). Kiya *et al.* (1997) experimented with single- and double-frequency sinusoidal disturbances and found that a minimum reattachment length was obtained at a particular forcing frequency. The effect of the shorter reattachment length was first shown by Roos and Kegelmann (1986) using periodic disturbances to control separation in a backward-facing step. Chun and Sung (1998) observed similar results by exciting the shear layer from a backward-facing step through sinusoidal oscillation of a slit jet. In response to the success in manipulating flow in simple geometries, research has since been done in effort to apply separation control to gas turbines [Rivir *et al.* 2000], over rotorcraft

ret

20

fic

co

for

fic

mo

inj

ca

pe

Ex

at

on

us

du

a

co

er

at

at

retreating blades [Loerber *et al.* 2000], and in planar diffuser flows [Coller *et al.* 2000]. These are just a few of the many studies that have been completed on flow manipulation, as it is difficult to reference all studies.

There are two ways of controlling flows: passive and active. Passive flow control requires no energy. The flaps found on commercial airline planes are a form of passive control. During take-off, these flaps are extended allowing air to flow through a slit along the wing. The high-pressure flow beneath the wing moves through the slit to the low-pressure side of the wing. Therefore, new air is injected on the top part of the wing. This energizes the flow over the wing, thus causing the flow to remain attached to the wing of the airplane and improving performance by reducing drag and increasing lift.

Active flow control requires energy and is applied only when needed. Examples of active flow control include jets that add energy to the flow; suction at the surface, which removes energy from the flow; and actuators that can change flow conditions. An example of active flow control can be described using an airfoil. At a certain angle of attack, the flow separates from the airfoil due to an adverse pressure gradient on the surface, which produces a wake, or a low-pressure region, which causes large drag. By placing an active flow control mechanism, such as a jet, on the airfoil in the region of separation, energy is added to the flow and separation along the surface changes.

Over the years, there has been extensive research regarding the use of active flow control to manipulate internal and external flows in order to reduce drag, enhance lift, minimize vibrations, and control separation to cite a few

examples. This research has shown a great potential for the use of active flow control due to the advantage of being able to apply the control when needed and to specify the amount of control applied. However, in most, if not all, investigations, active flow control is applied to a priori known flow field. In practice, the details of the flow to be controlled may not be known. For instance, over a wing, control may be applied where separation is expected, not necessarily where it is actually occurring. Therefore, it would be advantageous to have a system that could detect and apply the control to the actual separation point and which can adapt to changing conditions. By integrating a feedback loop into an active, flow-control system, the information about the flow state can be gathered and directed back to the controller. Based on the flow-state information, the level of control and the position to apply the control can be adjusted in response to the flow conditions. This optimizes the device performance, uses energy only when needed and adapts to changing conditions.

In order to implement a feedback control system, there is a need for a methodology to estimate the flow state above the surface using embedded, surface sensors. This is important since, for all practical purposes, sensor arrays cannot be inserted within the flow stream without adversely affecting the performance of a technological device. Therefore, efficient models are necessary to take the information from the surface measurements and deduce the flow state above the surface. Examples of such models are Proper Orthogonal Decomposition (POD) and Stochastic Estimation (SE). Sources of

develop and verify different types of low-order models.

SU

(19

1.1

We

CO

de

ins

ab

fr

inf

th

op

me

sig

mu

acc

De

ea

pro

de,

such work include Corke *et al.* (1994) using the former approach, Guezennec (1989) using the latter, and Glauser *et al.* (1999) using both techniques.

1.5 Motivation and Objectives

This study was done in collaboration with NASA Langley Advanced Measurement and Diagnostics Branch (AMDB). Their interest has been in consolidating data from large sensor arrays into a manageable amount that describes the essential features of the flow state above the surface. For instance, suppose it is desired to track the core coordinates and size of a vortex above a wing. It would be extremely beneficial in processing measurements from, for example, 100 surface sensors to extract and feed *only* the needed information to the monitoring/control system. This would require transmission of three pieces of information (x and y coordinates and diameter of vortex) as opposed to 100 signals, thus simplifying the required complexity and cost of the measurement system significantly.

Since the 'on-board' hardware/software used for processing the sensor signals must be relatively simple and compact, the flow state estimator algorithm must also be relatively simple. Therefore, simplified (low-order), yet sufficiently accurate, models linking surface information to the dominant flow features are needed. Interest in such models for a variety of flow fields began around the early to mid-nineties. However, there are a limited number of investigations that provide surface and flow databases that are sufficiently comprehensive to develop and verify different types of low-order models.

2.1 Experimental Set-up

This study is aimed at characterizing the flow above the surface of a splitter plate with a fence using an 80 surface-microphone array, which has not been done before, although, Lee and Sung (2001) have studied a backward-facing step using a 32-microphone array. The current microphone-array measurements were taken simultaneously with particle image velocimetry (PIV) measurements in order to correlate the flow field above the surface, measured by the PIV, with the wall-pressure measurements, recorded by the microphones.

The specific goals of this study were:

- (1) To design and construct the fence-with-splitter-plate model
- (2) To compile an extensive database and verify its quality against previous experiments whenever possible
- (3) To analyze the space-time character of the surface pressure array data.

Only the time-averaged microphone results are described in this thesis. Instantaneous results for the microphone data as well as PIV results are left for future studies.

In the following sections the experimental set-up and procedure for both the microphone and PIV techniques as well as a detailed description of the model design is given. This is followed by a presentation and discussion of the time-averaged statistics, spectra, and correlations from the microphone data and a summary of findings along with recommendations for future studies.

St:

m

SP

a"

2.

se

Ea

2.

Re

Ha

W

to

re

2 EXPERIMENTAL SET-UP AND PROCEDURE

The subsequent sections describe the experimental set-up used in the study and the procedure followed throughout the investigation. Three types of measurement techniques were used to characterize the flow field surrounding a splitter-plate-with-fence geometry: static pressure taps, surface microphones, and particle image velocimetry.

2.1 Experimental Set-up

The experimental set-up consisted of the wind tunnel facility, the separating/reattaching flow model, and the measuring devices used in the study. Each of these components is described in further detail in this sub-section.

2.1.1 Wind Tunnel Facility

The experiment was completed in the open-circuit, Subsonic Basic Research (Wind) Tunnel (SBRT) at NASA Langley Research Center in Hampton, Virginia. The intake side of the tunnel is surrounded on three sides with a semi-circular, entrance lip that enables the incoming flow to stay attached to the wall. The upper lip is removed due to space constraints inside the tunnel room. A schematic of the tunnel is shown in Figure 2.1, that measures 3.54 m in length. Located downstream of the contraction is a 0.57 m wide by 0.82 m high by 1.85 m long test section. The walls of the test section consist of plywood, Plexiglas, and glass. The glass side is used for high quality flow visualization and particle image velocimetry (PIV).

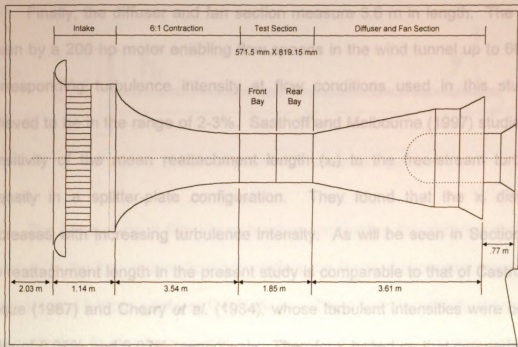


Figure 2.1 Subsonic Basic Research (Wind) Tunnel at NASA Langley

The inlet dimensions are 1.52 m wide by 1.82 m high. Air entering the tunnel flows through 0.2 m of aluminum honeycomb flow straighteners that use 12.7 mm cells designed to remove any flow swirl. The flow then moves through a double row of wire mesh turbulence screens, separated by 76.2 mm. These screens are located approximately 0.2 m downstream of the honeycomb and are shown in Figure 2.2, where x represents the streamwise distance measured from the fence, y is the normal distance from the splitter plate, h represents the step stretches 1.14 m leading into a 6:1 contraction section that measures 3.54 m in length. Located downstream of the contraction is a 0.57 m wide by 0.82 m high by 1.85 m long test section. The walls of the test section consist of plywood, Plexiglas, and glass. The glass side is used for high quality flow visualization and particle image velocimetry (PIV).

drive

Corn

belie

sens

inten

decr

the n

Haq

orde

is be

afec

wind

2.1.2

spitt

show

the fe

neg

to the

Finally, the diffuser and fan section measure 3.6 m in length. The fan is driven by a 200 hp motor enabling flow speeds in the wind tunnel up to 60 m/s. Corresponding turbulence intensity at flow conditions used in this study is believed to be in the range of 2-3%. Saathoff and Melbourne (1997) studied the sensitivity of the mean reattachment length (x_r) to the free-stream turbulent intensity in a splitter-plate configuration. They found that the x_r distance decreases with increasing turbulence intensity. As will be seen in Section 3.1, the reattachment length in the present study is comparable to that of Castro and Haque (1987) and Cherry *et al.* (1984), whose turbulent intensities were on the order of 0.25% and 0.07% respectively. Therefore, based on that comparison, it is believed that the turbulence intensity in SBRT was relatively small and did not affect the mean streamwise measurements. For more details concerning the wind tunnel specifications refer to Howerton (1998).

2.1.2 Model

The model, used for generating the separating/reattaching flow, was a splitter plate with a fence attached upstream perpendicular to the splitter plate as shown in Figure 2.2, where x represents the streamwise distance measured from the fence, y is the normal distance from the splitter plate, h_f represents the step height, and $2H$ represents the total fence height. The splitter plate was parallel to the flow and the fence was perpendicular to the flow.

Flow

Figure

sharp

that re

flow p

circul

down

also c

illustr

dimen

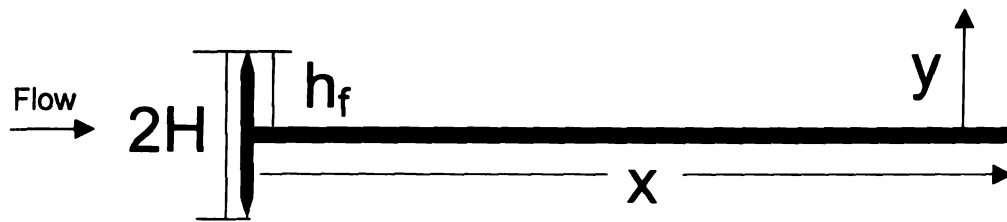


Figure 2.2 Splitter-plate-with-fence configuration

The general mean flow characteristics surrounding the plate are shown in Figure 2.3. As free stream flow approaches the fence, it separates around the sharp top and bottom edges of the fence, creating a highly unsteady shear layer that reattaches farther downstream. It is well known that the long-time, averaged flow pattern in the separating/reattaching flow region is characterized by a re-circulating flow zone upstream of the mean reattachment point (at location x_r downstream of the fence). Additionally, a smaller, secondary, re-circulating flow, also called the re-separation zone, exists in the fence/splitter-plate corner, as illustrated in Figure 2.3. The illustration in Figure 2.3 shows the ideal two-dimensional flow field surrounding the splitter-plate-with-fence configuration.

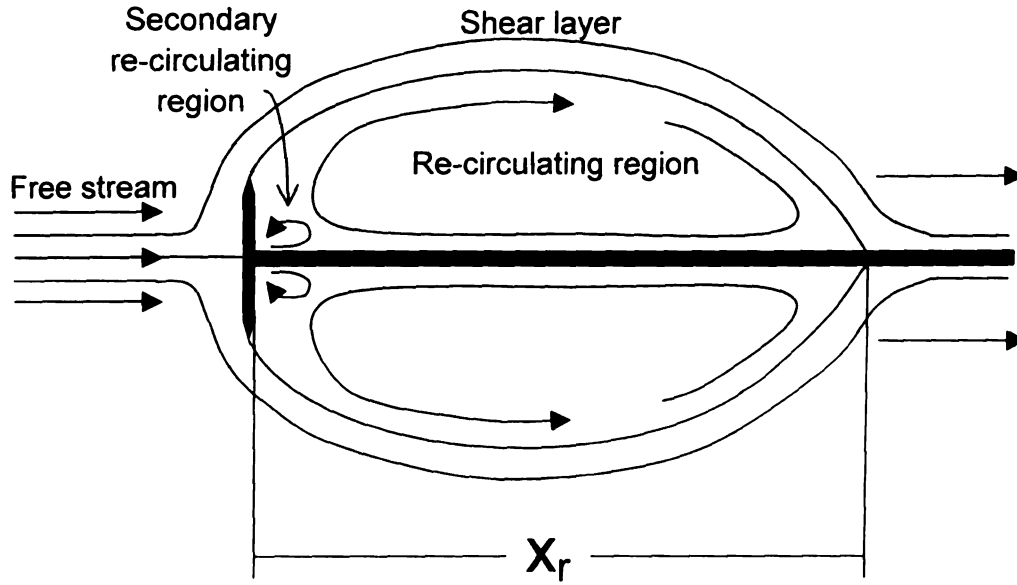


Figure 2.3 Flow characteristics surrounding the splitter-plate-with-fence configuration: x_r = reattachment length

By using the splitter-plate-with-fence configuration, the boundary layer effects seen in backward-facing step studies were eliminated. Beyond the separation point, the general character of the flow field for the two geometries is similar. However, upstream of separation there is a difference. In a backward-facing step, as explained by Eaton and Johnston (1981) who wrote a review on the research of the classic separating/reattaching flow model, an upstream boundary layer separates at the sharp edge of a step forming a free-shear layer. Figure 2.4 shows a backward-facing step flow.

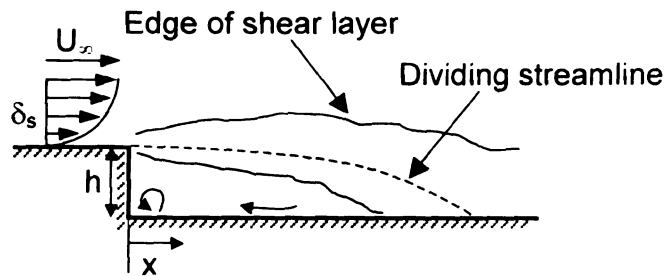


Figure 2.4 Flow field around backward-facing step - reproduced from Eaton and Johnston (1981)

Upstream of the step, the flow moves along the surface forming a natural boundary layer due to the no-slip condition at the wall and the viscosity of the fluid. As a result there is a thin layer (relative to the total flow stream) of moving fluid in which the velocity gradient changes dramatically over a short distance, producing significant shear stresses within this region. The boundary layer develops over the wind-tunnel wall up to the edge of the step, which results in a certain boundary-layer thickness at separation. Eaton and Johnston (1981) re-plotted initial boundary-layer thickness values against reattachment lengths, both normalized by step height, from four similar studies and found a significant connection between the two parameters. An increase in initial boundary-layer thickness resulted in a shorter reattachment length. Eaton and Johnston (1981) also reported that the state of the boundary layer before separation affects the flow structure after separation, leading to a significant effect on reattachment. Laminar boundary layers were found both to be dependent on Reynolds number (based on momentum thickness) and to grow more quickly than turbulent boundary layers, which were independent of Reynolds numbers. The Reynolds number was defined as

$$\text{Re}_\Theta = \frac{U_\infty \Theta}{\nu} \quad (1)$$

where U_∞ is the free stream velocity, Θ is the momentum thickness at separation, and ν is the kinematic viscosity. At the corner, the high shear stress layer separates and forms a free-shear layer similar to that of the splitter plate/fence model. Separation in the splitter-plate-with-fence configuration, as described by Castro and Haque (1987), differs slightly due to the strong favorable pressure gradient near the edge of the fence. This pressure gradient causes a thin laminar boundary layer at separation, after which transition shortly occurs. Because of the thin laminar boundary layer separation, the effects of boundary-layer thickness seen in the backward-facing step are negligible. That is, the boundary-layer thickness is small relative to the overall size of the flow field and therefore is not a significant parameter in this case.

The design of the model was symmetric with respect to top and bottom. It was constructed out of aluminum, measuring 1.6 m long by 0.36 m wide, and was supported by a 12.7 mm thick aluminum skeleton (Figure 2.5) covered with 3.175 mm thick aluminum sheets. The skeleton was also used to house the cabling for the microphones and the tubing for the static pressure taps.

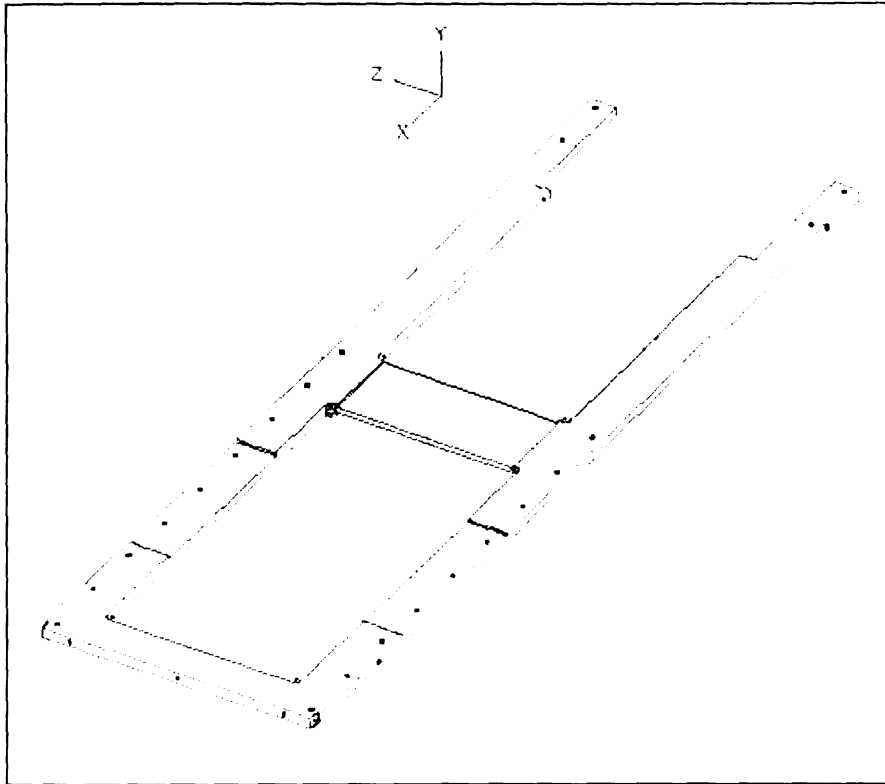


Figure 2.5 Skeleton used to support the model and to house cables and tubes

The model was fixed in the tunnel using posts secured to the sides of the skeleton. The posts protruded out the sides of the wind tunnel and were bolted to the tunnel walls using locknuts. There were several components that made up the splitter-plate-with-fence configuration as shown in Figure 2.6: fence, instrument plate, middle plate, tail plate, endplates, windows, and extensions.

Fe

ab

De

Ca

ne

te

S.

of

et

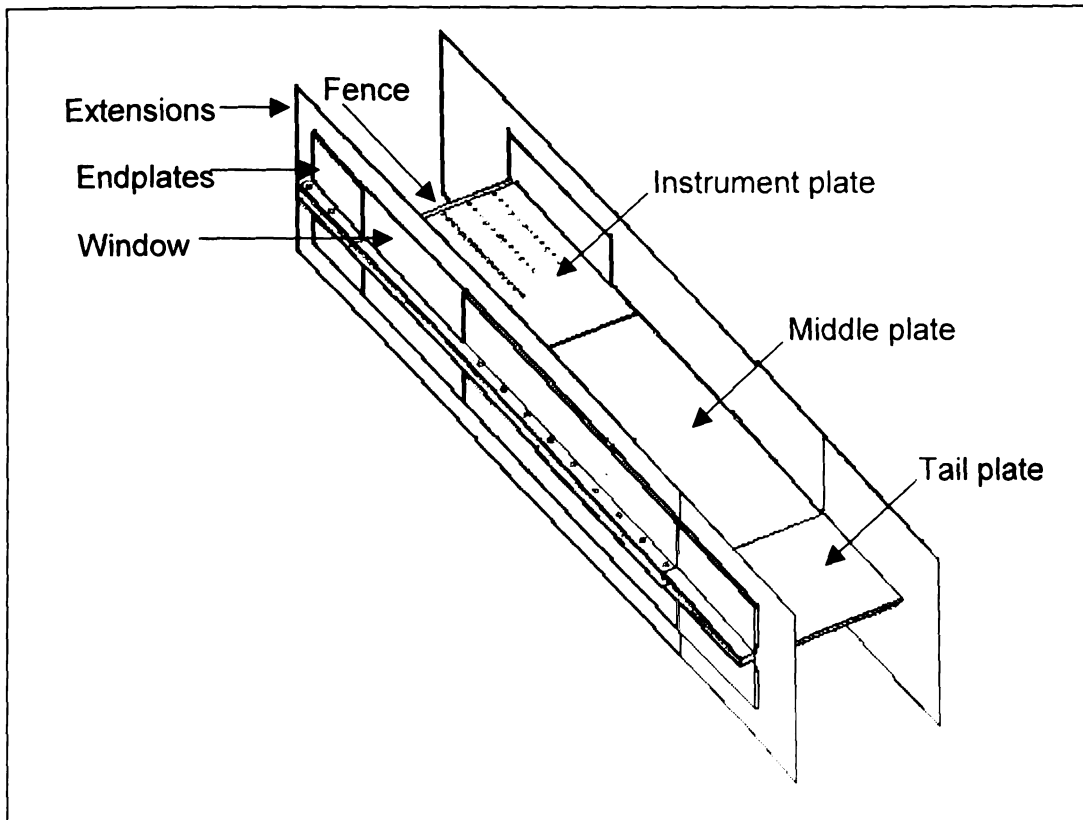


Figure 2.6 Schematic of actual model

Fence

The total fence height was approximately 35 mm, with a step height (h_f) of about 8 mm, which is the height of the fence above the splitter plate. In selecting the step height, it was necessary to consider the test section height of the wind tunnel and the reattachment length needed for the experiment. If the fence height was not sufficiently small in comparison to the test-section height, then the fence would create a significant flow blockage. Such a blockage would lead to substantial flow acceleration around the fence, thus affecting the mean location of the reattachment (x_r). Smits (1982) made a detailed documentation of the effect of the blockage ratio, defined as h_f/D_t where D_t is half of the test section

he

stu

pic

arg

use

par

as

fe

ns

m

es

22

height, on the reattachment length for a geometry similar to that used in this study. The pertinent graph from the study of Smits (1982) was digitized and re-plotted in Figure 2.7. As seen from the figure, a lower blockage ratio leads to a larger non-dimensional reattachment length. Thus, the graph in Figure 2.7 was useful in the design stage to estimate the reattachment point location for a particular selection of fence height.

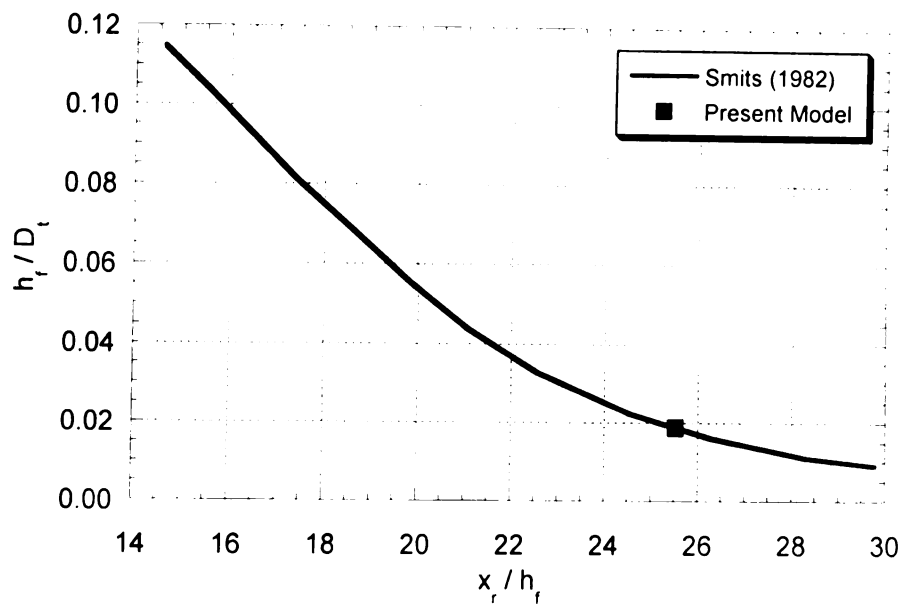


Figure 2.7 Dependence of reattachment distance on blockage ratio

On the other hand, it was desired to have an x_r location that was as large as possible to minimize the streamwise spatial gradients of the surface pressure field. This was important to attain the best possible spatial sampling of the instantaneous pressure field with a given microphone spacing. Twenty-eight (28) microphones, each with a diameter of 6 mm, were spaced 3.5 mm apart. This resulted in a total measurement distance along the centerline of approximately 262 mm, meaning the reattachment distance had to be shorter than that total

distance in order to capture the reattaching point of the flow. By knowing these parameters and by selecting a blockage ratio around 2%, the design, reattachment length was approximately 0.2m, which maximized the space allowed for spatial resolution and ensured that the reattachment point would be contained within the extent of the microphone array. The actual blockage ratio was calculated as a result of dividing half the test section height into the step height.

$$\text{Blockage Ratio} = \frac{h_f}{D_t} \times 100 = 1.94\% \quad (2)$$

where h_f is the step height and D_t is half the test section height. An overall blockage ratio as seen by the flow was determined by dividing the total fence height by the total test section height.

$$\text{Overall Blockage Ratio} = \frac{2H}{2D_t} \times 100 = 4.26\% \quad (3)$$

where $2H$ is the total fence height and $2D_t$ is the total, test-section height.

Three fence configurations were tested in order to determine the fence geometry for the study. Figure 2.8 shows the three different configurations. Geometry (a) is the classic configuration used in splitter plate/fence studies including Ruderich and Fernholz (1986) and Castro and Haque (1987). The fence in (b) is what was used in this study and fence (c) was tested for comparison purposes. Both fences (a) and (b) had the same step height.

the s

comp

exper

length

defin

where

meas

densi

the m

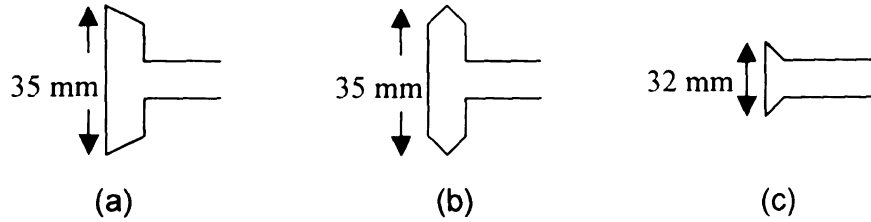


Figure 2.8 The three fence configurations tested

The fence geometries were tested by measuring the static pressure along the surface of the plate and determining the location of reattachment based on a comparison to the mean pressure data from Castro and Haque (1987). The experiment revealed the effect of the geometry of the fence on the reattachment length. The results are shown in Figure 2.9. The ordinate gives the C_p values, defined as

$$C_p = \frac{p_s - p_r}{\frac{1}{2}\rho U_\infty^2} \quad (4)$$

where p_s is the surface pressure along the model, p_r is the reference pressure measured with a static tap located at the exit of the contraction, ρ is the fluid density, and U_∞ is the free stream velocity. The abscissa gives the number of the microphones.

the m

that t

micro

fence

micro

flow

span

reata

camp

to o

beca

the m

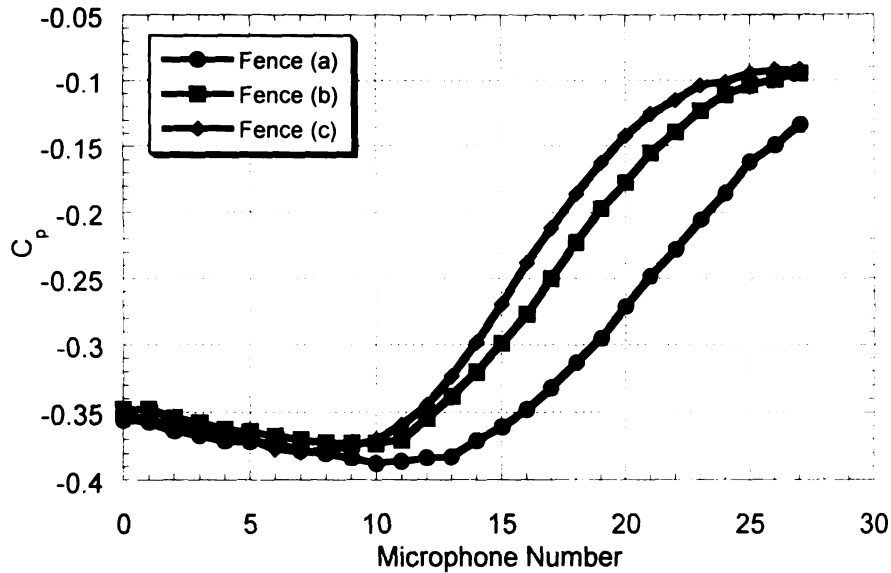


Figure 2.9 Static pressure distribution for all three tested fences – model was not aligned in the test section at this point

For fence (a), the mean pressure recovery occurs beyond the extent of the microphone distribution along the I-plate as shown in Figure 2.9, indicating that the mean reattachment point is near the end of or beyond the centerline microphones in the streamwise direction. The mean pressure distributions for fences (b) and (c) reveal mean pressure recovery within the spatial extent of the microphones along the centerline. Thus the mean reattachment length for the flow surrounding these two fences is shorter than the streamwise distance spanned by the measuring microphones. Between fences (b) and (c), the reattachment length on the splitter plate was longer when using fence (b) compared to fence (c) as evidenced by the point of pressure recovery for fence (b) occurring farther downstream than for fence (c) (Figure 2.9). Therefore, because of the relatively long reattachment length with respect to the extent of the microphones, fence (b) was determined to be the configuration for the study

as shown in Figure 2.10. The fence was about 6 mm thick and came to a point at the center forming an isosceles triangle.

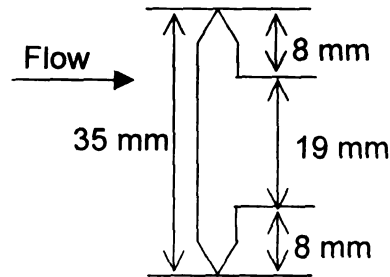


Figure 2.10 Fence configuration used in experiment

The difficulty with the fence configuration chosen is the possibility of early separation and reattachment at the front face of the fence before the main separation at the sharp edge of the fence. On the front face of the fence, the edge is beveled at 30° , which may cause a small separation of the flow before reaching the sharp point of the fence. This viable condition was not confirmed, as all measurements were taken downstream of the fence. Therefore, the effects on the flow are not known, but are presumed to be small due to overall scale of the flow field, for example, the fence height. More specifically, the scale and details of the thin separation boundary layer are not important compared to the size of the turbulent structures downstream of separation.

Once the step height was determined, the rest of the model's dimensions could be calculated based on the information presented by Castro and Haque (1987). The total splitter plate length was $160h_f$ or $73H$. Castro and Haque (1987) used a splitter plate length of $35H$. Smits (1982) confirmed the study done by Arie and Rouse (1956) stating that the splitter plate only needs to be

10:
pla
rea
oc
ch
(15
the
sp
bo
al
dis
the
int
at
ad
me
dis
Pa
m
13
the
the

10(2H) in length to be confident that the reattachment region will occur on the plate. The long length of the splitter plate used in this study not only ensured a reattachment point on the plate, but also aided in reducing the effects of downstream disturbances that could propagate upstream, i.e., acoustically, and change flow conditions in the measurement region. Farabee and Casarella (1986) observed, in their backward-facing step study, energized structures from the shear layer up to 72 step heights downstream of the step. In the case of the splitter-plate-with-fence configuration, energized structures from the top and bottom of a plate interact in the wake of the model. A lengthy splitter plate allows these vortical structures to diffuse and decay over a long downstream distance without a change in geometry, thus reducing the strength and allowing the break-up of the organized structures. Therefore, when the disturbances interact, the strength of the new disturbances formed due to the step-like feature at the end of the model (for more explanation see Section 2.1.2) is minimal. In addition, the point where the wake develops is so far downstream of the measurement region that the probability of the acoustics from the weak disturbances convecting upstream to the region of interest is small.

The splitter plate consisted of three sections: instrument plate, middle plate, and tail plate. Endplates were placed on the sides of the splitter plate to improve the two-dimensionality of the flow. According to Castro and Haque (1987), these endplates needed to be at least $10h_f$ upstream of the fence and the same above the splitter plate for the improvement. The endplates used in the present study measured $19h_f$ above the splitter plate and $30h_f$ upstream of

the fence. Each of these components will be addressed further in upcoming sections.

Instrument Plate

The instrument plate (also known as the I-plate) was about $52h_f$ long and was outfitted with 80 microphones and 80 static pressure taps. The configuration and the numbering of the microphones and the static pressure taps are shown in Figure 2.11. Dimensions for the microphone and static pressure tap layout are presented in Appendix A.

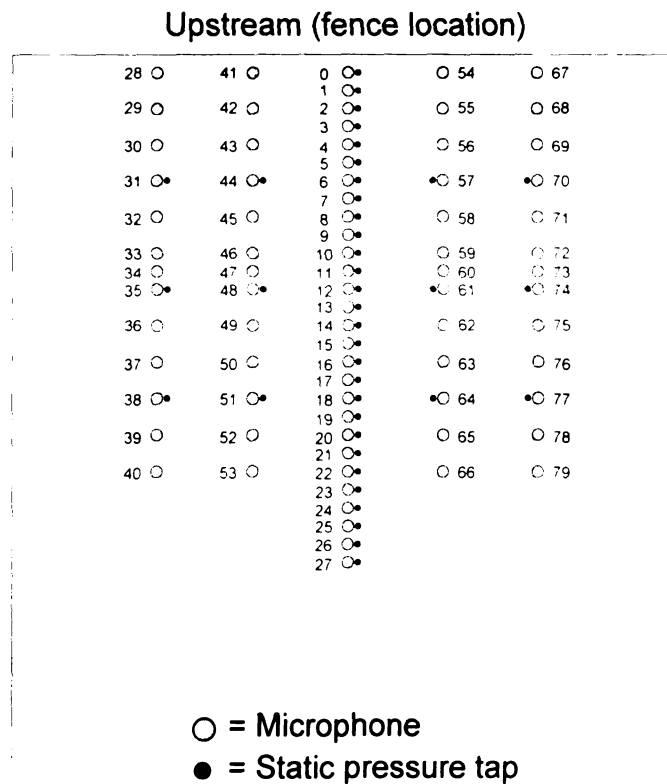


Figure 2.11 Instrument plate lay-out consisting of microphones and static pressure taps

00

the

min

ce

me

50

le

ce

dir

ten

pre

11

co

an

for

Ia

dis

70

35

The center row consisted of 28 microphones spaced 9.5 mm ($1.2h_f$ or $0.05x_r$) apart center to center in the streamwise direction, starting 4.8 mm from the fence. On either side of the centerline, there were 2 rows each containing 13 microphones. These 13 microphones were spaced 19 mm ($2.4h_f$ or $0.09x_r$) apart center to center, except for three microphones in each row that were spaced 9.5 mm apart center to center. The spanwise spacing between the five rows was 50.8 mm ($6.4h_f$ or $0.25x_r$).

The I-plate was also instrumented with 40 static pressure taps on the top I-plate and the bottom I-plate for a total of 80. The taps were aligned with the center of the microphones in the x direction but offset by 5.4 mm in the z direction. There were 28 taps next to 28 microphones on the centerline and the remaining 12 were spread out evenly among the four rows of 13. The static pressure tap locations mirrored each other on top and bottom.

Middle Plate

The middle plate (also called the M-plate) covered the skeleton on top and bottom. The middle plate measured approximately 0.61 m in length, or $76.8h_f$, and was used to cover the area where cabling for the microphones and tubing for the static pressure taps passed through.

Tail Plate

The tail plate (T-plate) was used to reduce possible downstream disturbances by gradually tapering the model thickness to a point. This would moderate the step-like feature at the end of the model that may create disturbances. These disturbances could propagate upstream, i.e., acoustically,

and change the flow conditions in the separating/reattaching zone of interest. The tail plate was 0.254 m long ($32h_f$); and it was designed to gradually slope on top and bottom, coming to point over the 0.254 m distance (Figure 2.12).

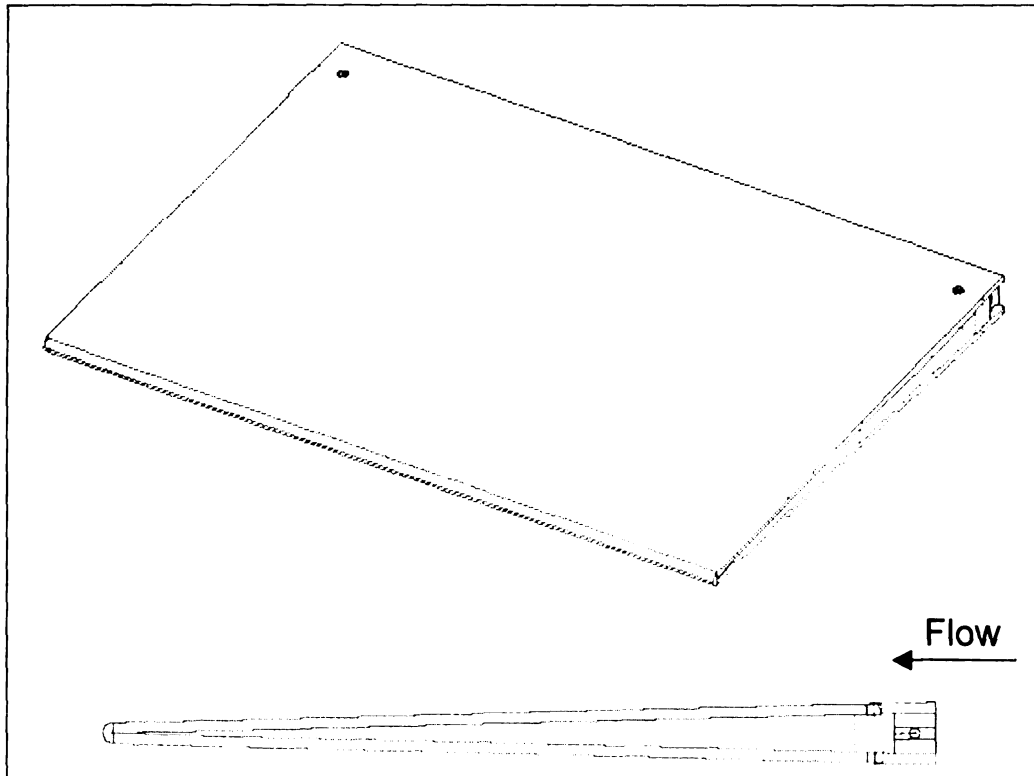


Figure 2.12 Tail plate used on the model: isometric view and side view

Endplates

Endplates were placed on either side of the model to shield the separated/reattaching flow region from the boundary layer on the sidewalls of the test section and to enhance the two-dimensionality of the flow. A new boundary layer, however, developed along these endplates. This new boundary layer grew

in

lay

sic

me

0.2

div

wh

the

Ha

the

asp

asp

Th

the

dim

in size with downstream distance but was substantially smaller than the original layer because of the shorter development length. Therefore, the effects of the sidewall boundary layers on the flow in the center of the model, the region of measurement, were minimized. The distance between the endplates was about 0.29 m, giving the model an aspect ratio of 36. The aspect ratio is calculated by dividing the width of the model by the step height.

$$\text{Aspect Ratio} = \frac{W}{h_f} = 36 \quad (5)$$

where W is the width between the endplates and h_f is the step height. The larger the aspect ratio, the better the two-dimensionality of the mean flow. Castro and Haque (1987) showed that the quality of flow two-dimensionality depended on the aspect ratio and whether or not endplates were used. In their study, the aspect ratio was 19 with endplates as shown in Figure 2.13. For this study, an aspect ratio of 36 was used along with endplates in the tunnel at NASA Langley. This aspect ratio is even larger than that of Castro and Haque (1987), and therefore it is expected that the flow here will have an even better 'two-dimensional' quality.

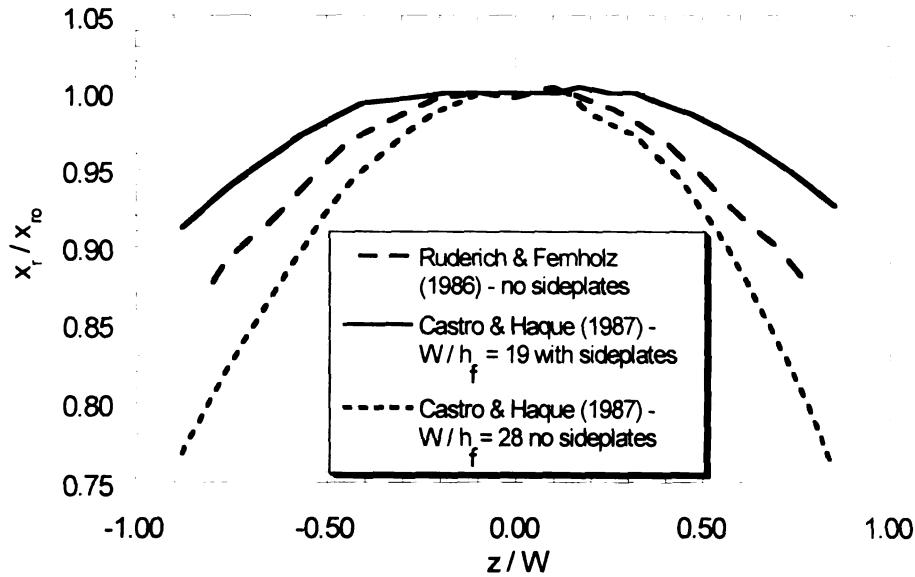


Figure 2.13 Spanwise reattachment lines reproduced from Castro and Haque (1987) – $x_{r0} = x_r$ along the centerline

The endplates were constructed out of 6 mm-thick aluminum angle stock and placed on the sides of the model. Glass windows replaced a 0.32 m stretch of the endplates to allow for camera access to the flow on top of the I-plate on either side of the model. These glass windows were placed on the topside only, and Plexiglas ones were used on the bottom side for possible access to the side opposite to that of measurements. Each of the windows extended from 6.35 mm upstream to 317.5 mm downstream of the fence.

Extensions were also added to the aluminum angle endplates to eliminate flow disturbances due to the 6.35 mm thickness of the endplates. As the flow approaches the thick endplates, it separates at the edges, thus creating another shear layer with vortical structures possibly similar to those seen in the main shear layer. These outside disturbances can affect the region of measurement by introducing vortical structures from the endplates that have nothing to do with

the main shear layer. Therefore, by placing 0.79 mm thick aluminum sheet extensions on the inside of the endplates, there is a minimal edge thickness where the flow may separate, creating a shear layer. Although the flow will still separate at these extension edges, the effects of separation are considerably reduced to the thickness of the extensions. The extensions extended $29h_f$ upstream and $130h_f$ downstream of the fence. These plates also extend $18h_f$ in the y direction above the splitter plate.

2.1.3 Instruments for Measurement

The measurement systems used to collect data included static pressure taps, microphones, and particle image velocimetry (PIV). The static pressure taps and microphones are described in this sub-section, whereas, the PIV is described in Appendix B. PIV images were acquired, but they were not processed and analyzed in this thesis.

Static Pressure System

Static pressure measurements were used to align the model in the tunnel, characterize the mean flow, and check for the two-dimensionality of the mean flow. To this end, static pressure taps were purchased from the Scanivalve Corporation (TUBN-063-.5). These were placed in eighty recessed holes on the top and bottom I-plates. The inner diameter of the taps was about 1 mm and the outer diameter was approximately 1.5 mm. The taps were connected individually using 0.254 m long Urethane tubes to a pneumatic connector (48D9M-1/2) of a scanivalve. Because the connector had only 48 ports, only 48 pressure taps were used in the static pressure measurements. Thus, the scanivalve enabled

stepping through the 48 static-pressure ports, linking each one individually to an output port. The scanivalve, designed and manufactured by Scanivalve Corporation (48D9-1/2 Scanner Oilless Design), has a 100 psi range and is driven by a rotary solenoid (48D9M-1/2). An encoder (DOETM-48) installed on the scanivalve generates binary numbers, corresponding to the scanivalve port connected to the output port. The encoder output was connected to an odd-even decoder (OED2/BINY), which converts the encoder binary information into a digital visual display. Moreover, a 12-bit parallel input module was used to capture the connected scanivalve port number to the data acquisition PC. This was used to check the operation of the scanivalve during data acquisition. The scanivalve was driven by the data acquisition PC through a homemade adaptor circuit shown in Figure 2.14.

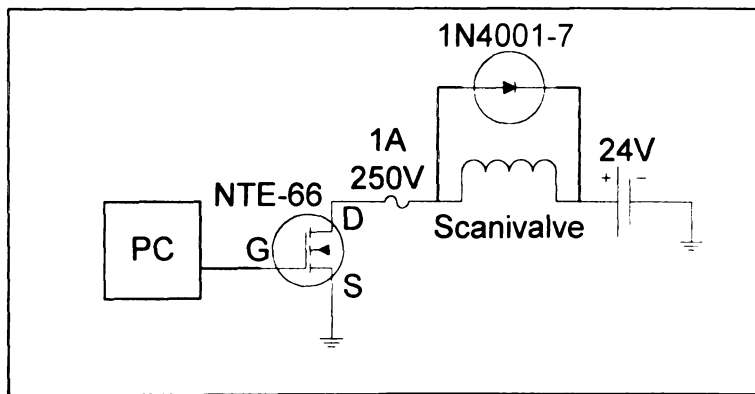


Figure 2.14 Circuit design used to control the scanivalve

The circuit contains a NTE-66 mosfet and is designed to step the scanivalve when the computer sends a 5V, 50-millisecond pulse. The mosfet consists of a gate, a source, and a drain. The gate is linked to the computer, the drain is connected to the scanivalve, which is coupled to a 24V power source,

an

th

vo

sc

re

m

fr

ra

We

ou

pr

pr

will

the

La

14

On

the

Fr

Hz

be

and the source is tied to the ground. When the computer sends the 5V pulse, the gate closes the connection between the source and drain, thus allowing a voltage drop across the scanivalve coil. This 24V voltage drop causes the solenoid motor to step. A resting period of at least three times the pulse width is required between steps in order to cool the solenoid. Therefore, a 150-millisecond delay was used between step pulses.

The output port of the scanivalve was connected to a pressure transducer from the Setra 239 series. The transducer measures differential pressure in the range 0-25.4 mm H₂O, outputting a corresponding 0-5V signal. The transducer was powered by a ± 12 V signal from a Hewlett Packard power supply. The output part of the scanivalve was connected to the negative pressure input of the pressure transducer. On the other side, the positive pressure port of the pressure transducer was connected to a reference pressure tap at the end of the wind tunnel contraction section. The data acquisition program used to acquire the static pressure readings was written by William Humphreys of NASA Langley.

Microphones

The microphones used in the experiment were Panasonic (WM-60A) Omnidirectional Back Electret Condenser Microphone Cartridges. Each microphone had a sensitivity of -44 ± 5 dB and a bandwidth of 20-20,000 Hz (Figure 2.15). The frequencies measured in the flow field ranged from below 20 Hz to approximately 1000Hz. Thus, the low-end of the measured frequency was below the frequency response range of the microphones. Because the

mic

ene

is e

the

sma

be s

thick

condu

ground

to driv

chips

Figure

60V at

microphone sensitivity below 20 Hz drops off, a reduction in the amount of energy recorded in the signal from the surface pressure fluctuations below 20 Hz is expected. This primarily affects the energy level for microphones closest to the fence, where low-frequency fluctuations are dominant. However, a very small effect, if any, is expected on the shape of the wall-pressure spectra (as will be seen in Section 3.5).

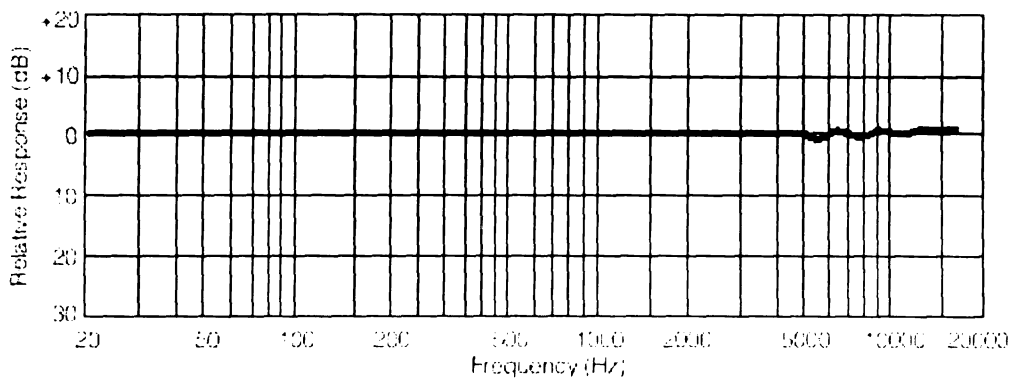


Figure 2.15 Typical WM-60A Frequency Response Curve –
Panasonic data sheet

The microphones were mounted flush with the surface in the 3.175 mm thick aluminum plate. The microphones were fixed to the plate using a conductive adhesive; therefore, the aluminum plate was utilized as the signal ground plane for all the microphones. An operational-amplifier board was used to drive the microphones. It contained 40 Motorola (MC33076) dual op-amp chips that had high output current, low power, low noise, and were bi-polar (Figures 2.16, 2.17, and 2.18). Two Trygon HR605B power supplies provided 0-60V at 5 amps to the microphone op-amp board.

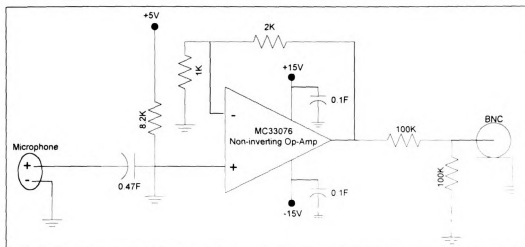


Figure 2.16 Schematic of the circuit used to drive the microphones and amplify the output signal

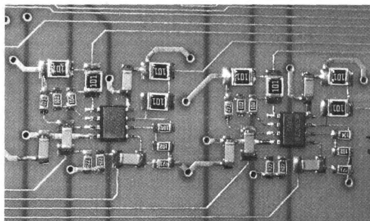


Figure 2.17 Actual circuit used to drive the microphones (two channels shown here)

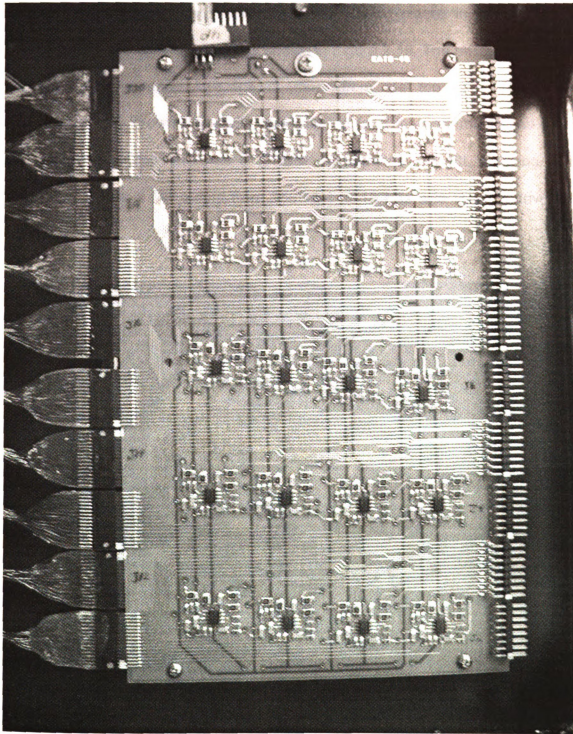


Figure 2.18 Op-amp board used to drive the microphones – two microphones per op-amp circuit. (Twenty shown here)

p

c

m

th

st

co

1

2

3

4

Each microphone was calibrated before being placed in the model. A photograph of the calibrator used is shown in Figure 2.19. The microphone to be calibrated was inserted into the chamber from the top and a reference microphone with known sensitivity was inserted from the bottom. In this case, the reference microphone was a $\frac{1}{4}$ " B&K microphone. A JBL, Lansing 075, speaker that has a flat output from 2500 Hz to 15 kHz was used to drive the calibrator.

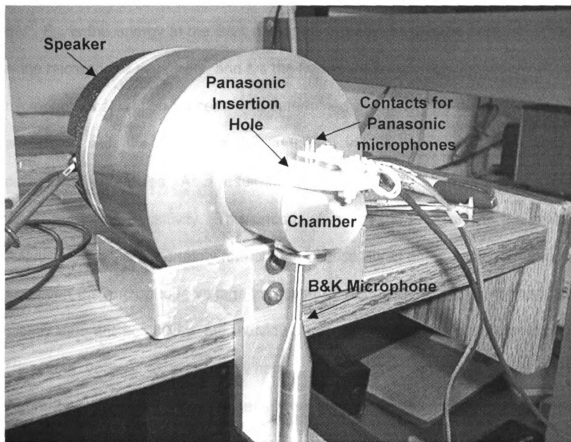


Figure 2.19 Microphone calibration unit

The two microphones received the same signal from the speaker at frequencies that varied from 1 kHz to 6 kHz, in increments of 1 kHz. The output

signals of the two microphones were recorded and compared in terms of amplitude and phase difference. The amplitude information was used to determine the sensitivity of the Panasonic microphone, while the phase data were used to verify any possible inter-microphone delay. More specifically, the sensitivity was calculated using the following equation.

$$k_m(f) = \sqrt{\frac{E_{vv}(f)}{E_{pp}(f)}} \text{ [mv/Pa]} \quad (6)$$

where E_{vv} is the energy in the Panasonic's microphone voltage spectral peak in mV^2 , E_{pp} is the energy in the B&K microphone pressure spectral peak in Pa^2 , k_m is the microphone sensitivity, and f is the frequency in Hz. The uncertainty of the microphone calibration process was determined by computing the 2*RMS value associated with the scatter in the sensitivity values obtained at six different calibration frequencies. As a result, the uncertainty was determined to be about 7% of the mean sensitivity. This uncertainty gives the error of one realization; that is, it gives the uncertainty for using the sensitivity at one particular frequency to convert the microphone voltage to pressure. Because each microphone has a slightly different sensitivity, the individual microphone sensitivities were used in converting voltage to pressure when conducting measurements in the flow. Figure 2.20 shows a probability density function for the microphone sensitivities. Using a bin width of 0.5 over the sensitivity range, about 90% of the sensitivity values fall in the range of 15 to 17.5 mV/Pa.

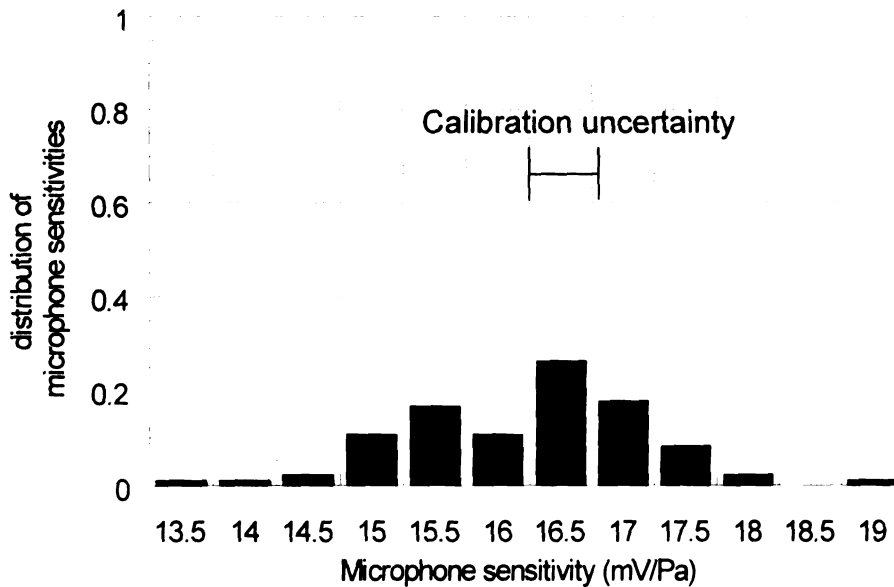


Figure 2.20 Distribution of microphone sensitivities

On the other hand, the phase results were used to check that the phase variation with frequency was linear to avoid signal distortion [e.g., Proakis and Manolakis 1988]. Additionally, since the slope of the phase response line gives the time delay between the actual and measured pressures, it was important to check that the variation in this slope from microphone to microphone was substantially less than any important convective time scale in the flow. Figure 2.21 shows the percent distribution of the microphone time delays in a histogram format. Approximately 94% of the distribution falls in the range of -1.3×10^{-5} to -1.0×10^{-5} , which results in a time delay between 10 to 13 μs . Comparing this time delay range to an estimate of the average convective time scale, 635 μs , in the flow determined by dividing the spacing between microphones (9.5 mm) into the free stream velocity (15 m/s), it is evident that the microphone time delay is

more than an order of magnitude (≈ 50 times) smaller than the convective time scale.

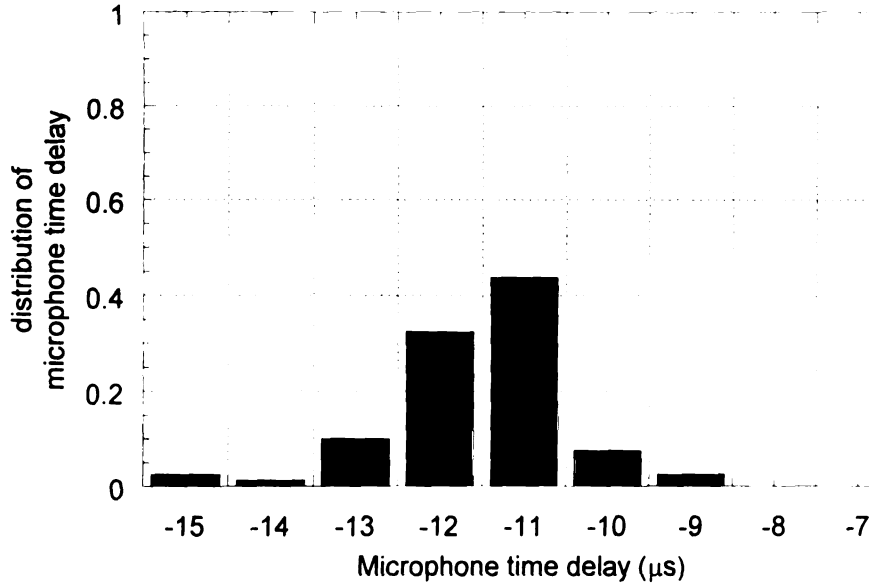


Figure 2.21 Distribution of microphone time delays

The microphones were connected to eight National Instruments A/D Boards (SCXI 1141), placed in a SCXI 1001 chassis. Each board had an input signal range of $\pm 5V$, eight differential analog-input channels, and a variable channel gain that was set to one for this experiment. The highest sampling rate the board is capable of is 1.25 MHz for one channel. For sixty-four channels, the minimum sampling rate is 19,531 Hz per channel. Because the channels were multiplexed, there is an average time delay between sampling each microphone, which results in a systematic error in the sampled data. However, this error is relatively small, $2.6 \mu s$, compared to the flow convective time scale, $635 \mu s$, over a distance equal to the microphone spacing. Each of the channels could also be connected to an ONO SOKKI FFT Analyzer (CF940) using a matrix switch in

0

w

E

C

w

P

d

P

n

Z

n

v

Z

C

t

A

s

order to spot-check the data during the experiment. Data from the microphones were collected using PC software written in Visual Basic by William Humphreys.

Particle Image Velocimetry

Particle image velocimetry was used to measure the flow field along the centerline in a plane perpendicular to the splitter plate. Although this technique was used extensively in the experiment, the results of these data will not be presented in this thesis. However, the experimental set-up and procedure is described in Appendix B. This was done in effort to document the entire test procedure from the experiment in one manuscript and have this information readily available for future reference.

2.2 Experimental Procedure

The procedure for the experiment required a number of steps for all three measuring techniques. Each step is outlined and described beneath in the various sub-sections for the different measuring systems.

2.2.1 Static Pressure System

For the static pressure measurements, preliminary tests had to be done to determine the acquisition time, to check the acquisition time delay, and to align the model within the test section.

Acquisition Time

Mean pressure in this study was determined by taking the average of the static pressure values recorded for a period of time. This meant that the time

series had to be long enough to ensure a stable average. To determine the time required to obtain a stable average of the mean pressure, a variety of time series lengths (Table 2.1) were acquired for one of the pressure ports (#10 in this case) and the stability of the average was checked.

Table 2.1 Time series lengths tested and C_p values

Time Series Length (seconds)	C_p Values
2	0.5273
5	0.5274
8	0.5366
10	0.5375
15	0.5339
20	0.5352

The stability was checked by plotting the C_p values for each time series listed in Table 2.1. As with any statistical information, confidence in the mean value is obtained by ensuring enough points are sampled to give a stable mean value. Figure 2.22 gives the C_p distribution as a function of time series length and shows an increase in the C_p value between time series 5 and 8 seconds. Beyond 8 seconds, the C_p values fluctuate slightly ($\approx 0.3\%$) around 0.536, but are relatively stable. Overall, the actual difference between the C_p values at all time series is very small around 2%, which means any time series could be used with confidence. However, 10 seconds was selected as a more than sufficient length of time for obtaining a stable average of the static pressure data. During the 10 seconds, the data were sampled at a rate of 100 Hz.

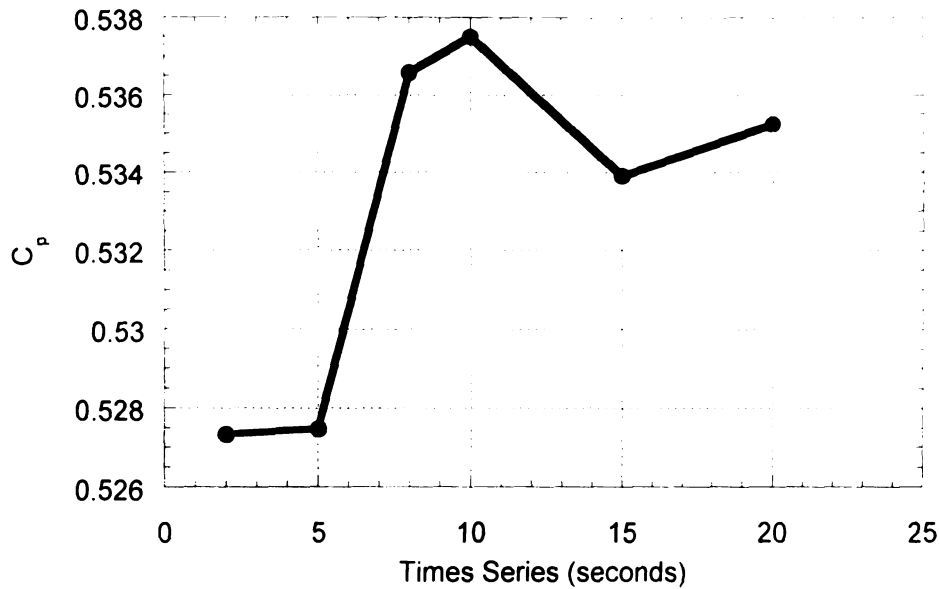


Figure 2.22 Mean pressure values at six different tested time series

Acquisition Time Delay

Due to the relatively long length of the tubing used to connect the static pressure taps to the scanivalve, the acquisition time delay had to be verified. More specifically, when the scanivalve steps from one port to the next, there is a time delay that is directly proportional to the tubing length before the pressure transducer senses the new pressure. This delay needed to be evaluated to guarantee that data acquisition started after waiting an appropriate time period for the new reading to stabilize. Because of the large pressure difference between the front and back of the I-plate, the acquisition delay test was done by switching from a back port to a front port while acquiring a 20-second time series. The acquired data showing the measured static pressure are plotted in Figure 2.23.

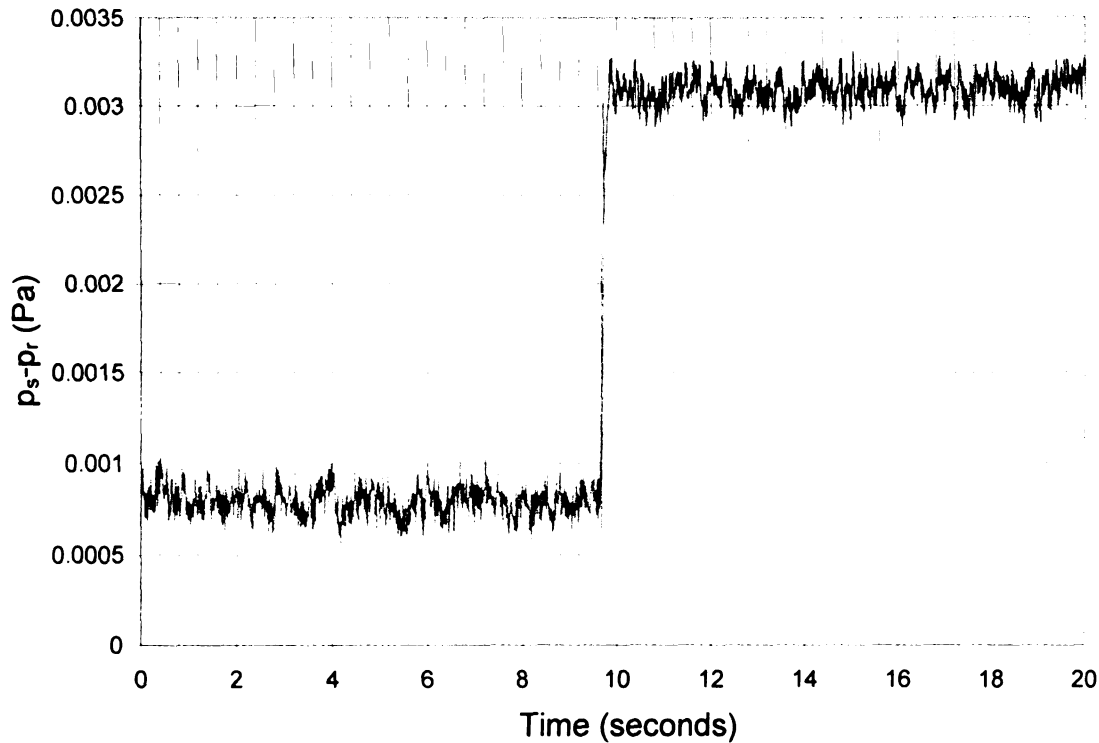


Figure 2.23 Typical step response of the tubing/pressure transducer system

The time delay was determined by estimating the time at which the port was switched and the time at which the transducer picked up the new pressure. The difference between the two times was considered the time delay. It was determined that this delay was very small, less than 0.15 s. Therefore, a one second time delay was used after each port step prior to acquiring data. This delay, which is clearly more than enough to eliminate the transient effect on the measurements, was the smallest allotted by the data acquisition program.

Alignment

The next experiment involved aligning the model in the tunnel using a two-part process. The first part was a two-port initial alignment based on comparing

the pressure at tap number 10 from the top of the model with the mirror image port on the bottom. Tap 10 was selected because in preliminary runs this was the location where the maximum pressure deviation from the reference occurred. The model was pivoted at the front by rotating the back end of the model through an angle of about 0.5° . By moving the back end, the angle of the model relative to the tunnel floor could be changed. Ideally, if the model was perfectly aligned and centered in the tunnel, such that the stagnation line on the fence coincides with the center of the model, the flow would be symmetric: top and bottom. To guarantee such symmetry, static pressure measurements were used to align the model.

In order to start aligning the model, it was placed at the bottom and top of the middle slot to determine the total pressure difference between the maximum positive and negative angle positions. The model was then pivoted to different angle positions starting with 0.15° relative to the tunnel floor, moving to 0.26° , and finally to 0.31° . At each position, the two designated ports were recorded. When the static pressure reading for each port was equal, then the model was considered aligned. At this point, an all-port final check was done to verify the alignment. Reasonable agreement of the pressure port readings along the centerline row on the top with the centerline pressure port readings on the bottom were used as an indication of the mean flow symmetry on the top and bottom of the model as seen in Figure 2.24. The abscissa gives the distance along the splitter plate with respect to the reattachment distance and the ordinate gives the C_p values.

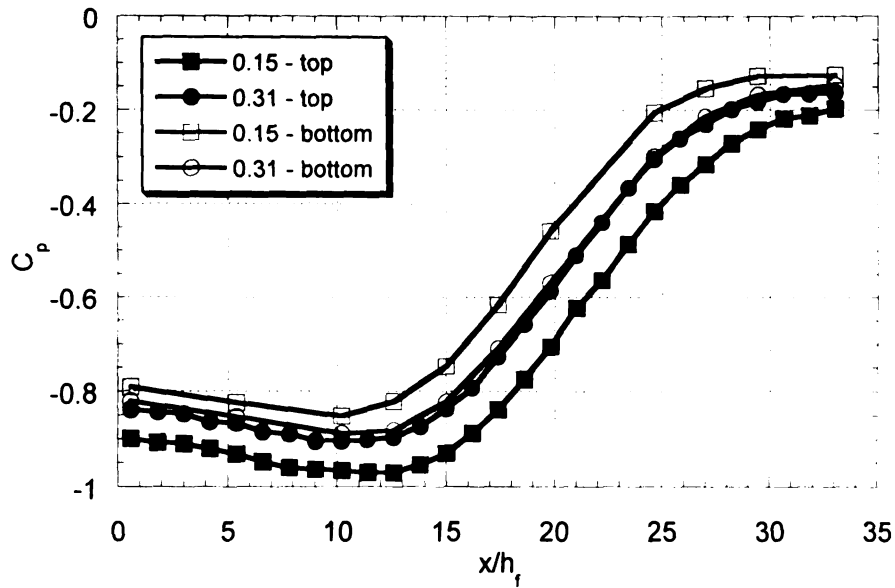


Figure 2.24 Vertical alignment of model in the tunnel in the streamwise direction

This method is different from the method used by Cherry *et al.* (1984) as well as Ruderich and Fernholz (1986). In the case of Cherry *et al.* (1984) the model was placed at zero incidence with respect to the free stream flow. A trailing flap at the back edge of the model was adjusted to remove any asymmetry top-to-bottom. This was confirmed by comparing C_p values on the top and bottom as seen in the present experiment. Ruderich and Fernholz (1986) also used flaps at the downstream end to adjust for symmetry around the model. An analysis of the vertical pressure distribution in front of the bluff plate at different spanwise locations and a check of oil surface streaking pictures verified the symmetry. Castro and Haque (1984) measured the reattachment length on the top and bottom as well as compared surface pressure measurements on the fence to confirm top-and-bottom symmetry.

Mean flow uniformity in the spanwise direction was also checked. This was accomplished by comparing measurements of the static pressure at different spanwise locations to those on the centerline. Moreover, top/bottom symmetry of the flow off-center was verified by contrasting off-center pressure measurements on the top and bottom. The results are shown in Figure 2.25 for data obtained at the $x/h_f = 15$ position. The figure displays values of C_p normalized by the C_p value at the centerline as a function of spanwise coordinates with respect to the model width. As seen, the measurements from the top and bottom agree closely. This suggests that good flow symmetry is obtained across the span of the model. Furthermore, the flatness (within 2%) of the spanwise distribution of the C_p indicates that a satisfactory region of nominally two-dimensional flow is obtained in the vicinity of the centerline.

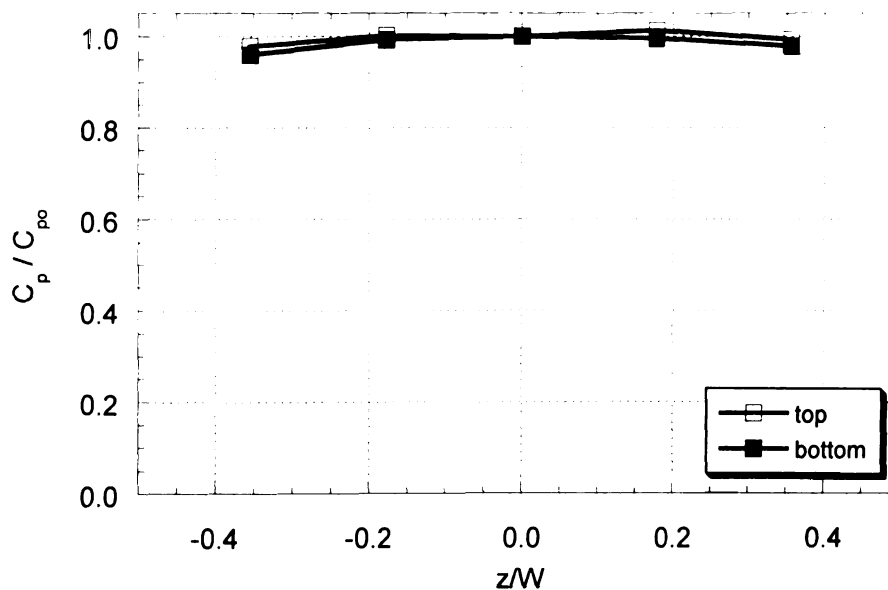


Figure 2.25 Check for two-dimensionality of the mean flow in the spanwise direction – $C_{p0} = C_p$ at x along the centerline

2.2.2 Microphones

The procedure for the microphone measurements was established after conducting a number of preliminary tests, and the following is a description of these tests.

Cross Talk Check

Because of the multi-channel nature of the microphone measurements, the microphones had to be checked for cross talk. Cross talk is defined as the 'leakage' of the signal from one microphone into the neighboring channel of another microphone by electric means (e.g., electromagnetic or capacitive coupling). In order to test for cross talk, a hand-held sound signal generator was used to generate a harmonic sound signal at 1000 Hz. The signal was fed to a single microphone using a short tygon tube. Data were acquired for all 64 channels, and the auto-spectrum of each channel was calculated and used to estimate the relative strength of the cross talk signal at the channels other than where the sound was applied. The acquisition rate per channel used was approximately 19 kHz, which was the fastest acquisition rate for the data acquisition hardware and thus represented the worst-case scenario as far as cross talk effects are concerned. The results showed that the maximum amount of cross talk observed was about 30 dB lower than the input signal (1 kHz). That is, if channel one receives a 1 kHz sound signal and the spectrum obtained at this channel was normalized so that the spectral peak at 1 kHz is 0 dB, then the other 63 channels would read no higher than -30 dB at 1 kHz. During actual data acquisition, the sampling rate was only 6 kHz and 12 kHz, which is lower

than the 19 kHz used in the cross-talk test. Therefore, it was expected that the actual cross talk would even be several decibels lower than -30dB and would not interfere with the desired measurements.

Data Acquisition Parameters

The data acquisition parameters used to record the microphone data were determined based on known information about the flow and from the necessary data collection parameters for the PIV images. It was anticipated that the flow frequencies of interest would not exceed 2500 Hz. Power spectra, sampled at 12,000 Hz and similar to the one seen in Figure 2.26, were checked to determine if flow frequencies exceeded 2500 Hz. The spectrum analyzed was close to reattachment, where the energy in the flow is highest. The semi-log format for plotting the spectrum in Figure 2.26 gives the RMS pressure fluctuations as the total area under the curve. As seen, this area vanishes for frequencies higher than 1000 Hz, confirming the belief that the fluctuations associated with flow structures of interest are contained below 2500 Hz. Therefore, the cut-off frequency of the anti-aliasing filters employed was set to 2500 Hz. The corresponding sampling frequency was at 6000 Hz, giving a Nyquist frequency of 3000 Hz. These were the parameters used when collecting surface pressure array and PIV measurements. However, for the investigation described in the thesis, the anti-aliasing filters were set at 5000 Hz and the sampling frequency was 12,000 Hz, resulting in a Nyquist frequency of 6000 Hz.

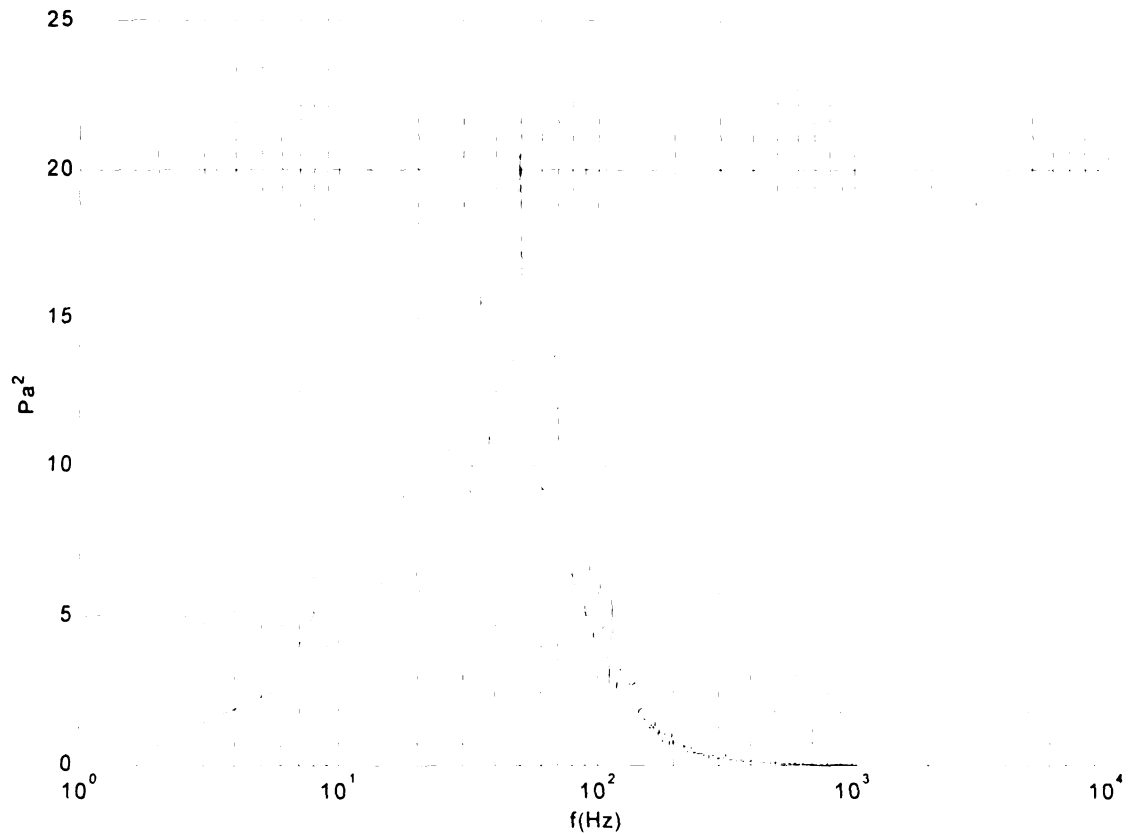


Figure 2.26 Power Spectrum sampled at 12,000 Hz for the microphone closest to reattachment

The appropriate acquisition duration was also tested at a 6000 Hz sampling rate to ensure the stability of the surface pressure RMS. This is similar to the test done for the mean pressure data. The test was done at 15 m/s and four different time series lengths as shown in Table 2.2.

C

n

v

a

S

S

W

S

IC

to

to

a

Se

Table 2.2 Acquisition time values used to test convergence of C_p

Flow Speed (m/s)	Sampling Frequency (samples/second)	Acquisition Time (seconds)
15	6000	5
15	6000	10
15	6000	15
15	6000	20
15	6000	25

Figure 2.27 show the RMS pressure fluctuation distribution as a function of time series length in seconds. This distribution was used to determine the minimal time series length needed to produce a stable RMS value of the time-varying pressures. As can be seen in Figure 2.27, the RMS values do not reach a stable value, yet variation is small on the order of around 1%. Furthermore, it should be noted here that one PIV image was to be acquired per second for 20 seconds. Because the microphone signals recorded were to be synchronized with the PIV images, the microphone time series needed to be at least 20 seconds. As a result, it was necessary to acquire the microphone signal for longer than 20 seconds to ensure that enough microphone data were available for each PIV image. Therefore, microphone signals were acquired at 6000 Hz for 25 seconds when simultaneously acquiring PIV images. However, for the analysis in this thesis, microphone data were acquired at 12,000 Hz for 15 seconds.

N

cc

di

re

m

th

m

fig

co

mi

las

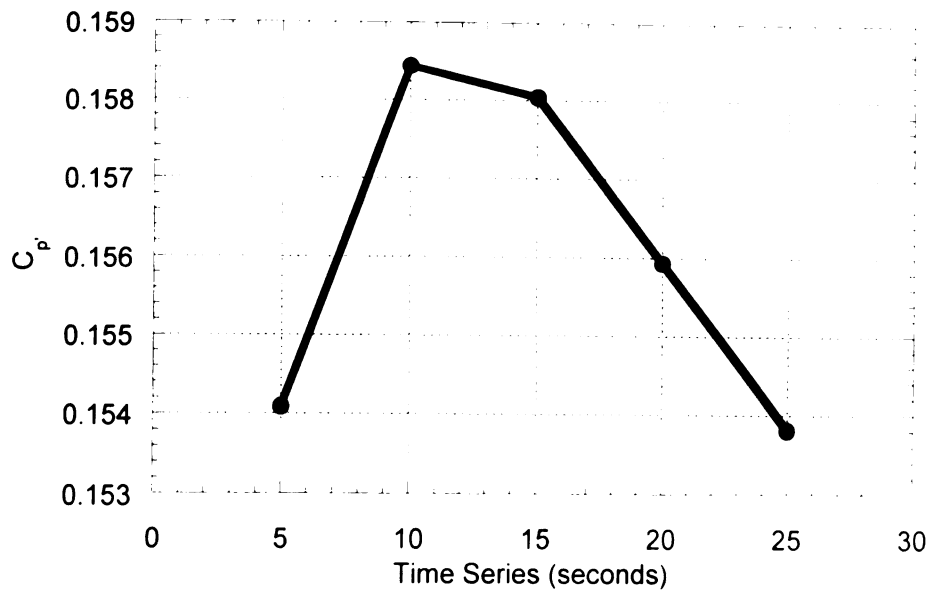


Figure 2.27 RMS pressure fluctuations – 5 different time series

Noise Cancellation Microphones

Because the microphone measurements are also susceptible to contamination by noise produced by the wind tunnel fan and disturbances due to diffuser unsteadiness, special provisions were implemented to remove and/or reduce such noise. In particular, three 'noise-cancellation' microphones were mounted in the wall extension between one side of the test section and one of the endplates, as seen in Figure 2.28. The figure provides a plan view of the model in the vicinity of the separation/reattachment zone. As depicted in the figure, the microphones were located at three different streamwise positions, corresponding approximately to that of the beginning, middle, and end microphones in the center row. The three microphones were connected to the last three channels in the data acquisition system.

se

m

Inv

dis

de

Si

ien

pro

m

no

the

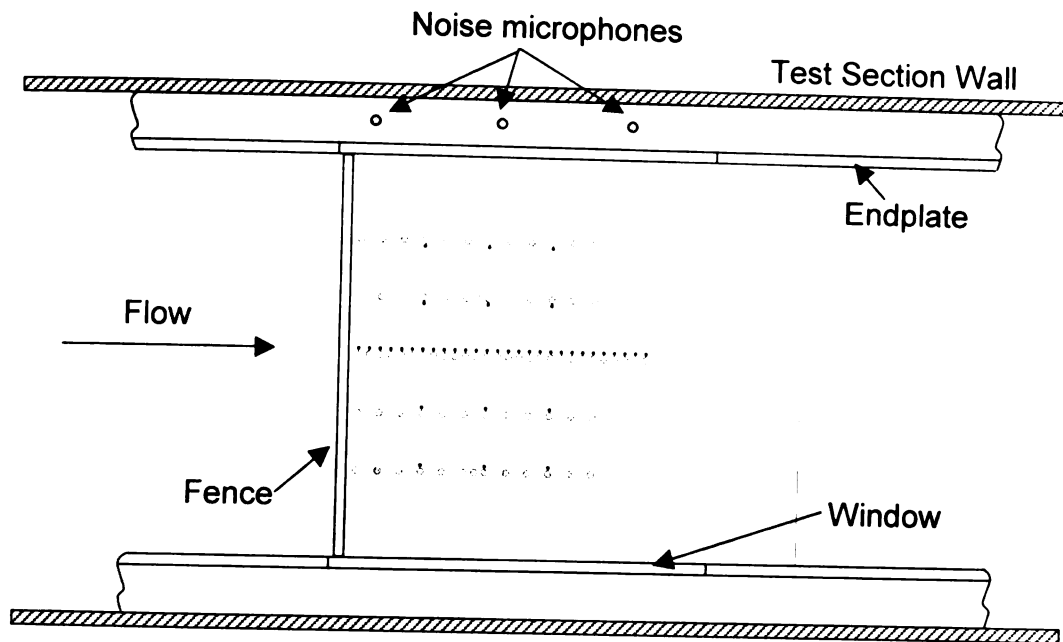


Figure 2.28 Schematic showing position of noise cancellation microphones

Since the noise cancellation microphones are shielded from the separated/reattaching flow region by the endplates and extensions, they do not measure the pressure fluctuations caused by flow structures in that region. Instead, they measure the noise from the fan, diffuser unsteadiness disturbances, along with the pressure fluctuations from the boundary layer developing on the extension plate in which the microphones are embedded. Since the dominant noise sources in the wind tunnel seem to be long-wave length and two dimensional in nature [e.g., Willmarth and Yang 1970], it should produce the same unsteady pressure field at the noise and measurement microphones. This correlated component of the measured signal between the noise and measurement microphones can then be estimated and removed from the measurements using an optimal filtering technique. Details of this technique

are described in Naguib *et al.* (1996), who applied it successfully to remove wind tunnel noise from surface pressure measurements beneath a turbulent boundary layer.

In this study, the noise removal was implemented using the noise-cancellation microphones located at the most downstream position. This was done since the results seemed to be insensitive to the downstream location of the noise-cancellation microphone. It should be mentioned here that the first 5–8 microphones were the most prone to noise effects, since the RMS pressure fluctuations provided by the flow are lowest close to the fence. Farther downstream, the flow-produced pressure fluctuations overwhelm that produced by the noise. Figures 2.29 and 2.30 demonstrate the measured power spectrum and auto-correlation at microphone #0 (closest to the fence) before and after noise cancellation. The harmonic peaks associated with tunnel noise are indicated by arrows and the corresponding frequency is given. As can be seen from the power spectrum and the auto-correlation, the wind tunnel noise in the signal was removed.

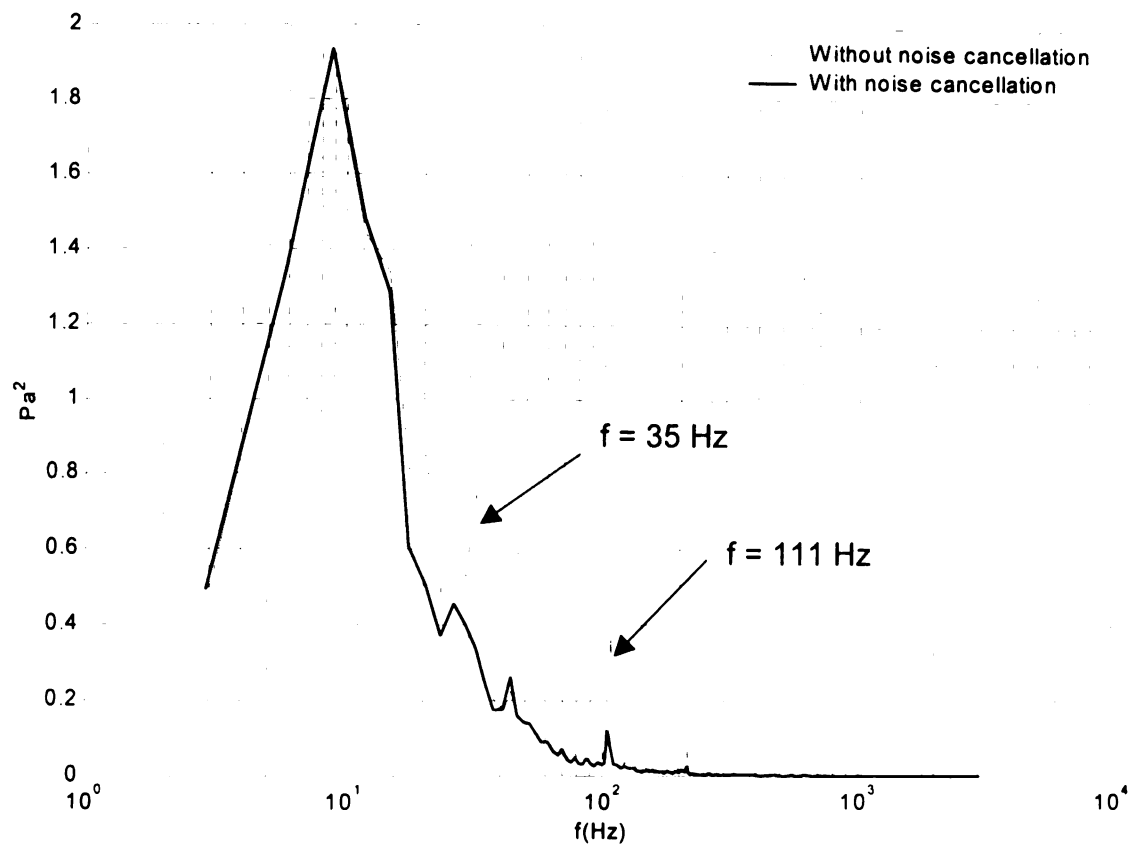
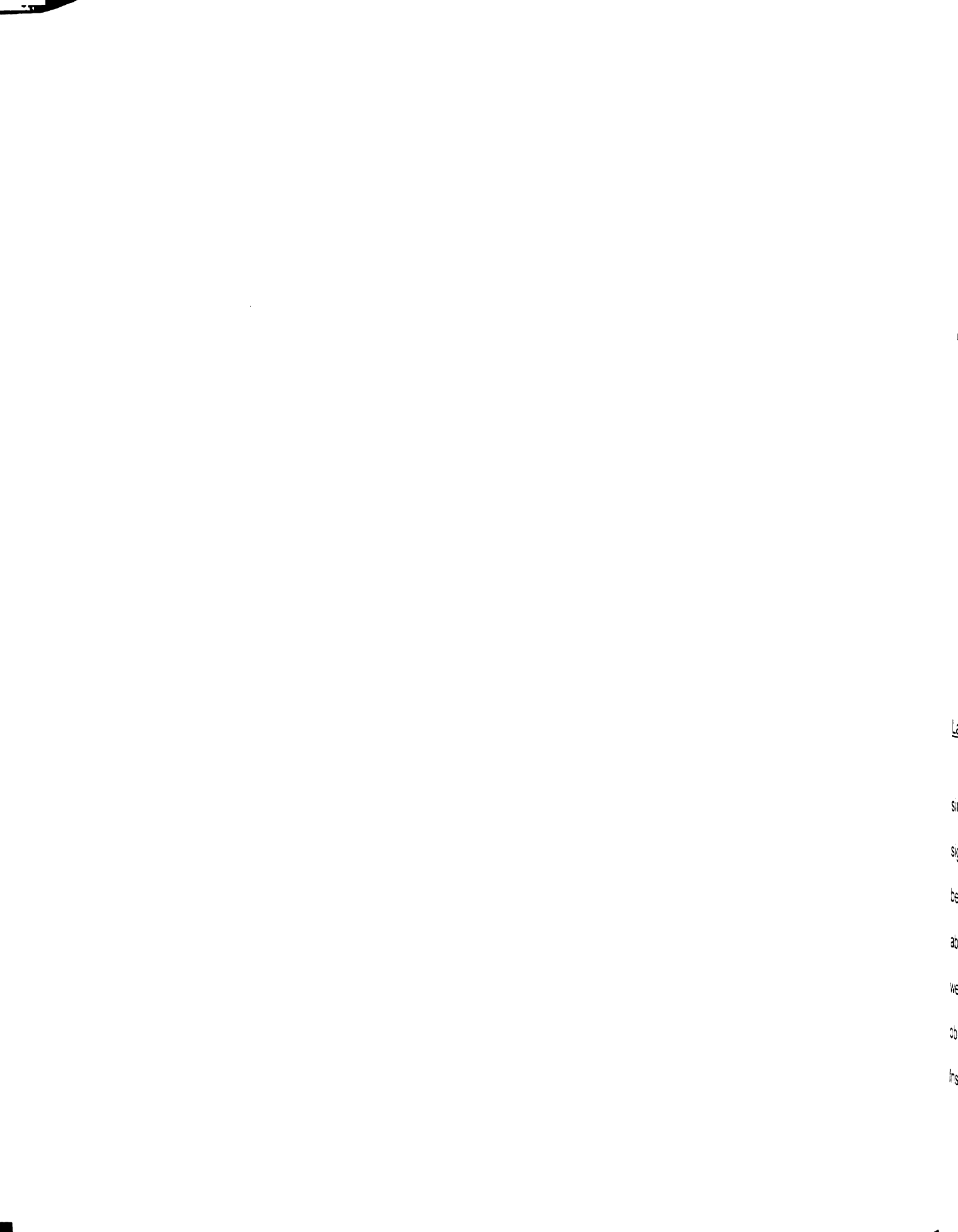


Figure 2.29 Power spectra for microphone #0 with and without noise cancellation



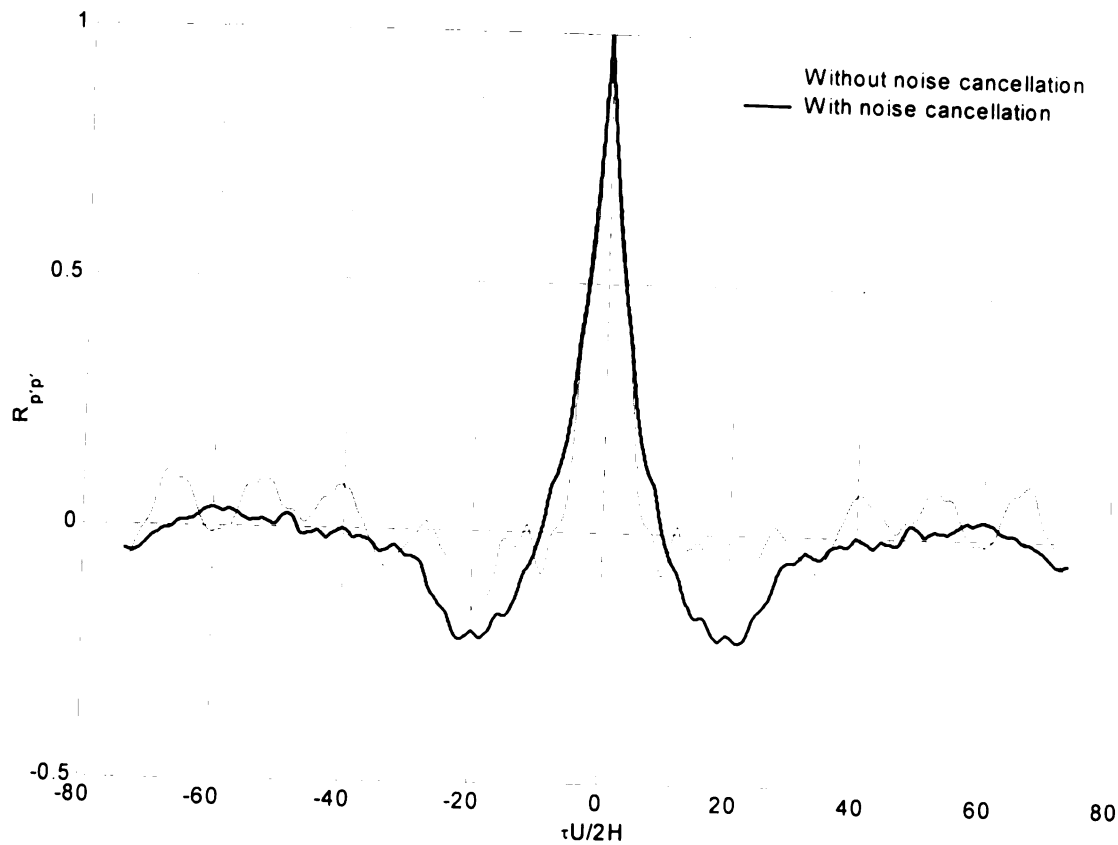
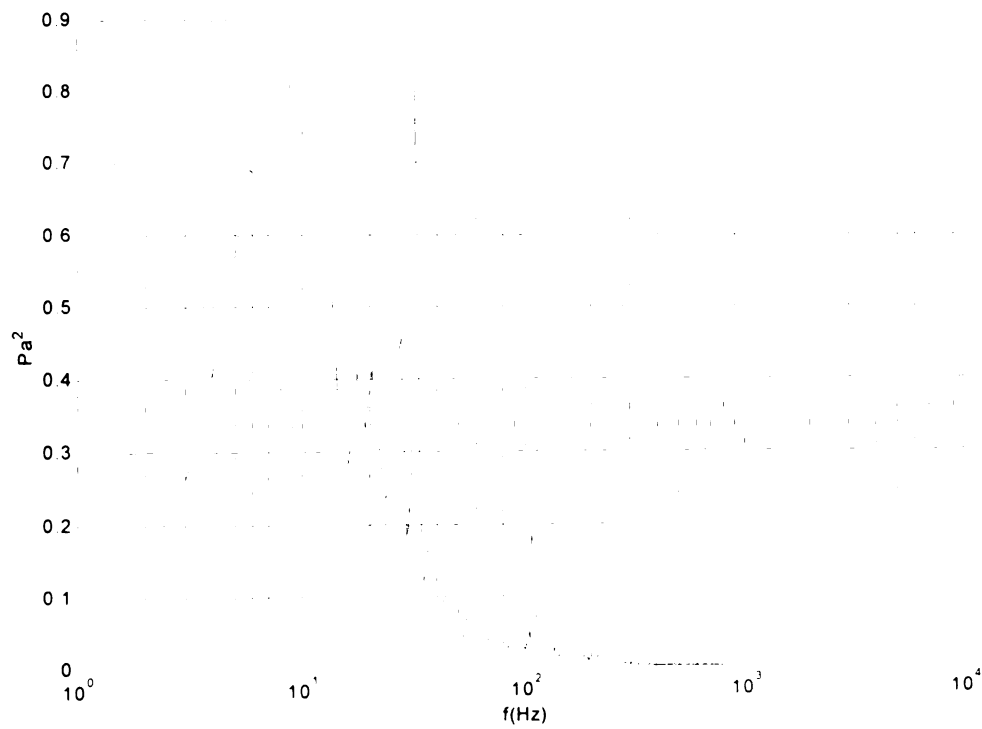


Figure 2.30 Auto-correlation for microphone #0 without and with noise cancellation

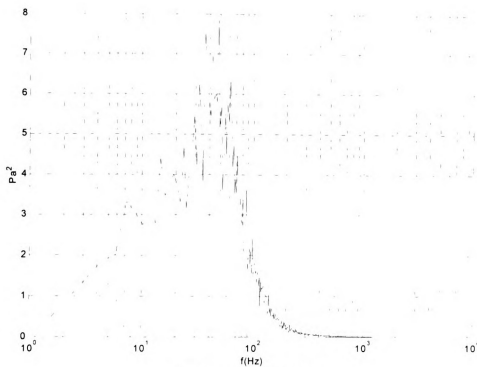
Laser Noise

Because microphone and PIV measurements were conducted simultaneously, it was important to check that the laser did not induce a noise signal in the microphone at the laser repetition frequency. Such a signal could be produced by electromagnetic coupling since the laser sheet was immediately above the centerline microphones or by the audible sound heard when the lasers were pulsed. Figure 2.31a, b, and c show the surface-pressure power spectrum obtained without noise cancellation at microphones 2, 14, and 26 respectively. Inspection of Figure 2.31a, b, and c clearly shows that the measured surface-

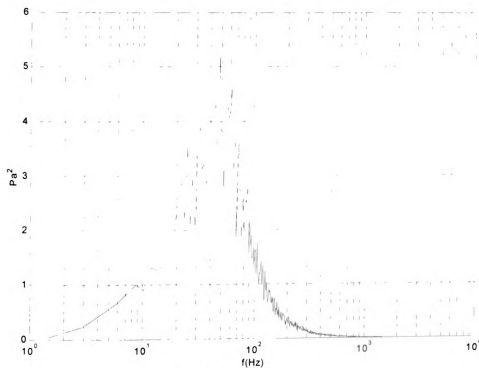
pressure auto-spectra contain no peaks at the laser frequency (10 Hz) or its harmonics. Therefore, no special filtering needed to be done for the laser noise.



(a) Microphone #2



(b) Microphone #14



(c) Microphone #26

Figure 2.31 Surface-pressure power spectra at microphones #2, 14, and 26

Airfoil

As discussed in Appendix B, the region of the PIV measurements was illuminated with the laser sheet using a 45° mirror that was embedded in an airfoil and mounted downstream of the model. The airfoil shape minimized disturbances produced by the mirror support. However, the mirror itself did not conform perfectly to the airfoil profile. Therefore, it was desired to check if any disturbances produced by the protruding portion of the mirror of the airfoil support affected the surface pressure measurements. Additionally, the mean pressure distribution was checked to verify that there was no effect on the mean flow as well. To this end, the microphone as well as the static pressure tap data were checked before and after the airfoil was placed in the tunnel. Figure 2.32 shows the static pressure data for the two conditions. There was a slight increase in the static pressure along the surface when the airfoil was placed in the tunnel, but the symmetry top and bottom remained the same. However, there was no change in the characteristics of the flow. Reattachment remained at practically the same position for both conditions.

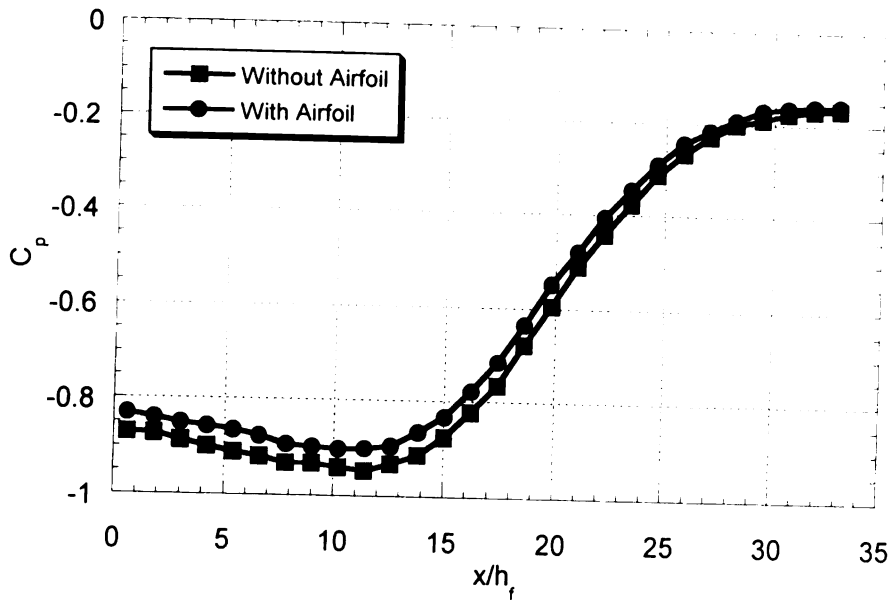
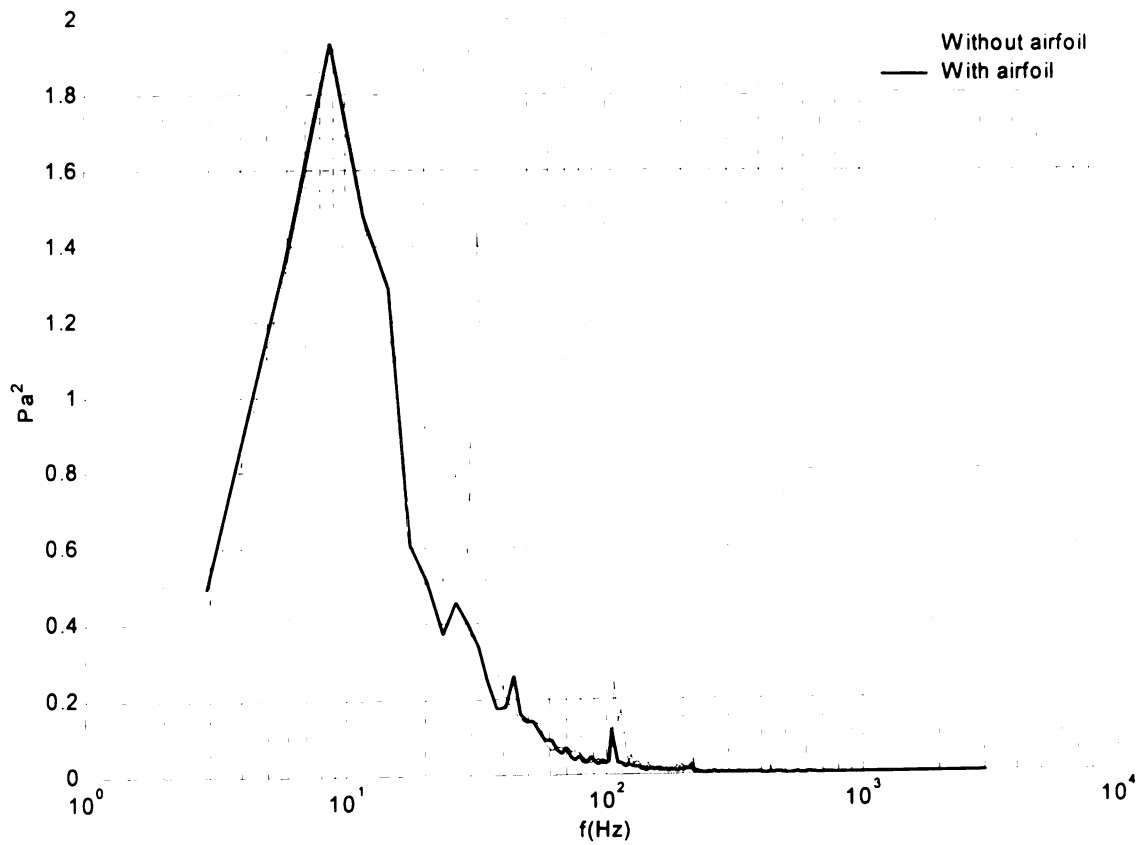


Figure 2.32 Static pressure data with and without airfoil in tunnel

Surface-pressure spectra data were compared with and without the airfoil in the tunnel for the microphone closest to the fence and the microphone nearest to reattachment on the centerline, Figures 2.33a and 2.33b respectively. As seen from Figure 2.33a, the broadband component of the surface-pressure spectrum remains unchanged. Interestingly, however, the harmonic peaks associated with the tunnel noise seem to be attenuated significantly by the presence of the airfoil. This is believed to be caused by alteration to the sound field of the fan noise produced by placing the airfoil inside the tunnel. Possible mechanisms causing such alteration include but are not limited to sound reflections of the foil and the insertion of the airfoil in the noise path. Farther downstream, (Figure 2.33b) the spectra seem to agree well with and without the airfoil, except for differences caused by the data scatter in the vicinity of the spectral peak. Such scatter can be reduced by increasing the number of records

used in calculating the spectrum at the expense of the number of points per record. However, this would reduce the resolution of the spectrum, obscuring some of the harmonic peaks in the spectrum.



(a) Microphone #0 – closest to the fence

B:

to

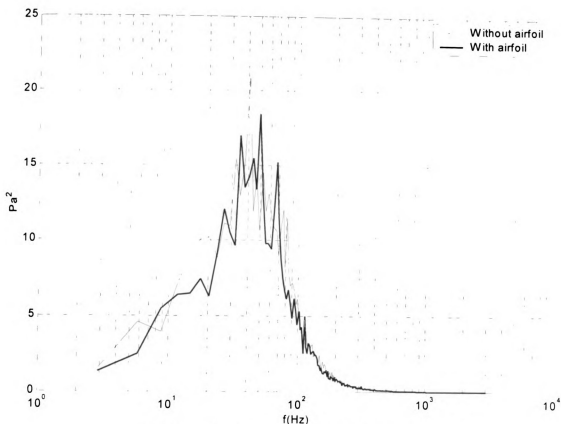
ter

su

me

ex

ex



(b) Microphone nearest to reattachment

Figure 2.33 Auto spectra of microphone data with and without airfoil

Base Microphone Run

Base microphone measurements were collected without the PIV system to benchmark the surface pressure characteristics without the PIV seed. This test was done at two different speeds: 15 and 20 m/s. Hence, it was possible subsequently to verify if the PIV seed caused alteration to the surface pressure measurements or if it affected the microphone response. Generally, however, extensive testing of the effect of the PIV seed was conducted prior to the experiment (See Appendix C).

2

R

W

S

—

L

—

—

—

—

—

—

—

We

the

of

se

to

2.2.3 Data Collected

The following is the test matrix used for the experiment (Table 2.3).

Reynolds number (Re) is defined as

$$Re = \frac{U_{\infty} h_f}{\nu} \quad (7)$$

where U_{∞} is the free stream velocity, ν is the kinematic viscosity, and h_f is the step height as previously described.

Table 2.3 Test matrix used for the experiment

Date	Data	Reynolds #	# of runs	Microphones		PIV	
				Acquisition Frequency (Hz)	Total # samples	# of pictures per camera	Camera Position
7/28/00	Microphones only	7885	1	12000	180000		
7/28/00	Microphones only	10513	1	12000	180000		
8/3/00	Microphones and PIV	7885	51	6000	150000	1020	downstream
8/4/00	Microphones and PIV	7885	49	6000	150000	980	downstream
8/9/00	Microphones and PIV	7885	100	6000	150000	2000	upstream
8/10/00	Microphones and PIV	7885	100	6000	150000	2000	downstream

In terms of the static pressure taps, ten second scans of the various ports were recorded. The ports scanned included the centerline 28 on the top of the model and centerline ports 0, 2, 4, 8, 10, 12, 14, 16, 20, 22, 24, 27 on the bottom of the model. In terms of the microphones, the length of the time series was 25 seconds as previously discussed. Tables 2.4 and 2.5 show the microphone matrix used in the tests.

is

Se

m

Qu

H2

pu

AC

an

Table 2.4 Microphone matrix for microphone only tests – C = ADC channel and M = microphone number

C	M	C	M	C	M	C	M	C	M	C	M	C	M	C	M
0	0	8	8	16	16	24	24	32	32	40	40	48	67	56	75
1	1	9	9	17	17	25	25	33	33	41	50	49	68	57	76
2	2	10	10	18	18	26	26	34	34	42	51	50	69	58	77
3	3	11	11	19	19	27	27	35	35	43	52	51	70	59	78
4	4	12	12	20	20	28	28	36	36	44	53	52	71	60	79
5	5	13	13	21	21	29	29	37	37	45	64	53	72	61	56
6	6	14	14	22	22	30	30	38	38	46	65	54	73	62	58
7	7	15	15	23	23	31	31	39	39	47	66	55	74	63	60

Table 2.5 Microphone matrix for microphone and PIV tests – C = ADC channel, M = microphone number, and T = Trigger

C	M	C	M	C	M	C	M	C	M	C	M	C	M	C	M
0	0	8	8	16	16	24	24	32	32	40	40	48	68	56	76
1	1	9	9	17	17	25	25	33	33	41	51	49	69	57	77
2	2	10	10	18	18	26	26	34	34	42	52	50	70	58	78
3	3	11	11	19	19	27	27	35	35	43	53	51	71	59	79
4	4	12	12	20	20	28	28	36	36	44	64	52	72	60	56
5	5	13	13	21	21	29	29	37	37	45	65	53	73	61	58
6	6	14	14	22	22	30	30	38	38	46	66	54	74	62	60
7	7	15	15	23	23	31	31	39	39	47	67	55	75	63	T

The matrix in Table 2.4 was used in the microphone only tests, thus, this is the configuration used for collecting the data analyzed in this thesis, which was sampled at 12,000 Hz. In Table 2.5, this set-up was utilized for the PIV and microphone tests. For PIV, one picture was taken a second for 20 seconds per run. There were a total of 100 runs at these following conditions: 15 m/s, 2500 Hz cutoff frequency, 6000 samples/sec for 25 seconds, and 40-microsecond pulse separation. The pulse train sent to the camera was recorded on the last ADC channel (T = Trigger) in the time series data so that the microphone data and the PIV data could be synchronized.

3 RESULTS AND DISCUSSION

In the following sections, an analysis of the data collected from the surface pressure measurements is presented. Time-mean and RMS pressure statistics characterize the mean flow field around the model and the fluctuation energy in the surface pressure signature, respectively. Auto-correlations and power spectra outline the time scales of the vortical structures influencing the wall-pressure fluctuations. Finally, cross-correlation and phase analyzes are used to explore the convective character of the flow structures.

3.1 Reattachment Length

The reattachment length is an important parameter for the present flow geometry and, as shown by Ruderich and Fernholz (1986), is the appropriate length scale for this flow field. Therefore, before analyzing the data it was necessary to estimate the reattachment length for the purpose of normalizing the data. This was done utilizing the pressure coefficient (C_p^*) used by Ruderich and Fernholz (1986) in their presentation of C_p results. The form of C_p^* was first proposed by Roshko and Lau (1965). As Ruderich and Fernholz explain, the mean pressure distribution from different long-separation-bubble studies correlates well by using a C_p^* , which is defined as follows

$$C_p^* = \frac{C_p - C_{p,min}}{1 - C_{p,min}} \quad (8)$$

where $C_{p,min}$ is the minimum C_p in the mean pressure distribution. Figure 3.1 shows the C_p^* distribution for six different studies as a function of the distance

a

s

c

th

th

l

n

s

A

t

and

len

bot

along the splitter plate normalized by the reattachment length. All six of the studies, except the Cherry *et al.* (1984) study, used a splitter-plate-with-fence configuration. Cherry *et al.* (1984) investigated a blunt-face splitter plate, with thickness of the plate defined as D . The legend displays details about each of the studies for which data are shown in the Figure 3.1.

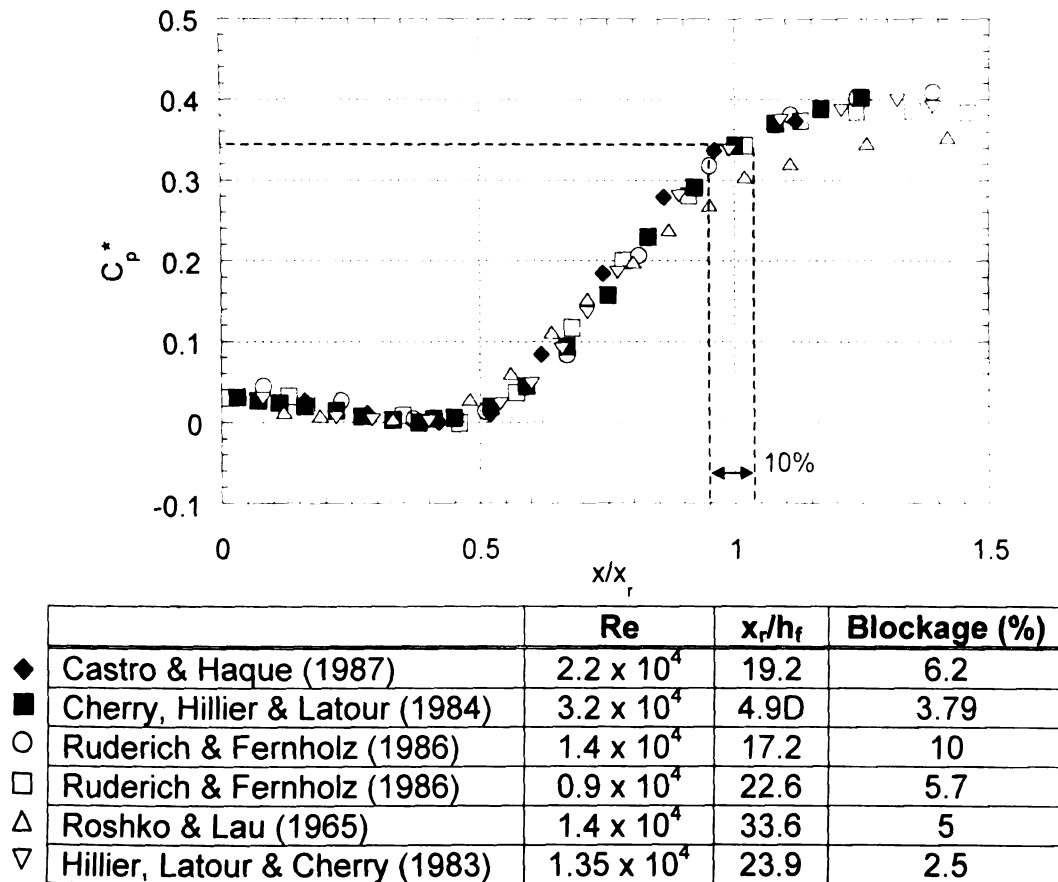


Figure 3.1 The pressure coefficient distribution for six different studies

Although these studies were conducted at different Reynolds numbers and had various blockage ratios, resulting in a difference in the reattachment lengths, the pressure distribution for each experiment correlates well when plotted using the C_p^* coefficient, even in the case of the blunt-face-splitter-plate

g

m

T

C

w

d

p

n

3.2

var

045

225

geometry. Thus, a universal pressure coefficient (C_p^*) value may be found at the mean reattachment location ($x/x_r = 1$), within the band of data scatter ($\pm 5\%$). This value was determined to be approximately $C_p^* = 0.345$. By applying this C_p^* value to the present data, the reattachment length could be determined within $\pm 5\%$ uncertainty as shown in Figure 3.2. Therefore, the reattachment distance was determined to be roughly 205 mm. Static pressure tap #21 is the port located closest to this reattachment value and thus was used in the normalization of the present data throughout the study.

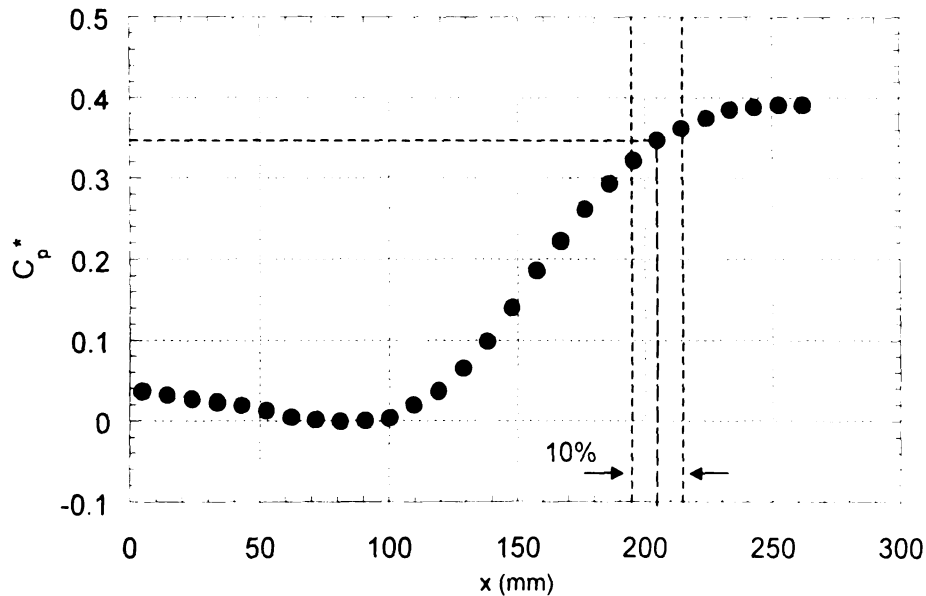


Figure 3.2 Mean pressure distribution of present data

3.2 Mean Pressure Distribution

Mean, or static, pressure distribution denotes the time-average spatial variation of the fluid pressure exerted on a surface as a result of a flow moving over that surface. Such a distribution can be measured using static pressure taps embedded in the surface and connected to a pressure transducer. Mean

p

n

s

F

a

tv

p

p

C

ms

mo

pressure measurements are used to characterize the mean flow surrounding a model. Examples of these measurements are found in most papers including splitter plate studies conducted by Castro and Haque (1987), Ruderich and Fernholz (1986), and Cherry *et al.* (1984). The mean pressure distribution can also be used to align a test model in the center of a test facility and to check the two dimensionality of the mean flow as discussed in Section 2.2.1. The mean pressure coefficient was defined in Section 2.1.2. Figure 3.3 shows the mean pressure distribution for the present model compared to the model utilized by Castro and Haque (1987) and Cherry *et al.* (1984).

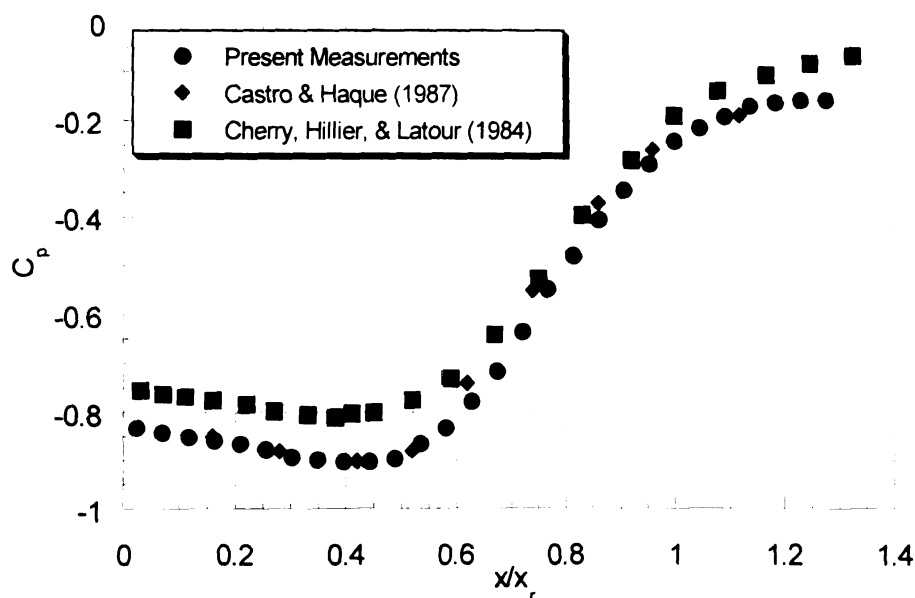


Figure 3.3 Mean streamwise pressure distributions for the current study compared to Castro and Haque (1987) and Cherry *et al.* (1984)

The C_p values are graphed as a function of the distance along the instrument plate normalized by the reattachment distance (x/x_r). As the flow moves downstream, there is a steady decline in the surface pressure until

a

st

p

p

p

re

se

th

m

Th

th

m

ov

se

str

wt

pie

Th

giv

va

Th

fac

approximately $0.5x_r$. Around $0.5x_r$ in Figure 3.3, the surface pressure values start to increase dramatically, with reattachment occurring in a region of small pressure difference.

The lowest point in the graph (around $0.5x_r$) represents the minimum pressure value along the surface of the splitter plate within the reattachment region and could coincide with the location of the highest point of the average separation bubble. Assuming the separation streamlines on top and bottom of the splitter plate to represent a wall, then the model takes on a geometry that may be approximated by a Rankine oval as proposed by Arie and Rouse (1956). The pressure distribution along the separation streamline is thus determined by the potential flow around the oval with the maximum velocity and hence minimum pressure (by Bernoulli equation) occurring at the top and bottom of the oval. To deduce the pressure distribution on the splitter plate from that along the separation streamline, consideration must be given to the re-circulating streamlines. However, pressure measurements at various vertical positions within the separation bubble, done by Arie and Rouse (1956) using a series of piezometer orifices, revealed that the mean pressure is invariant with height. Therefore, it appears that in fact the C_p distribution measured on the splitter plate gives good representation of the distribution along the separation streamline.

Theoretically, as the flow settles downstream of reattachment, the C_p value should go to zero, or rather approximately zero due to pressure losses. This was discussed by Farabee and Casarella (1986), who studied a backward-facing step geometry and stated that the pressure distribution after reattachment

s
w
in
co

C
be
va
of
us
(1)
wit
se
ie
co
sp
fac
sur
the
and
us
step
char

should return to the same as seen before the step. However in this study, data were neither collected before the fence nor farther downstream of reattachment in order to confirm this point, as these two regions were not the area of concentration.

Figure 3.3 shows fair agreement between the current results and the Castro and Haque (1987) data, which indicates the consistency of the mean-flow behavior around the constructed model with earlier studies. There is a slight variance between the present data and that from Cherry *et al.* (1984). This offset could be due to the difference in model geometry. Cherry *et al.* (1984) used a thick splitter plate without a fence. The comparison to Cherry *et al.* (1984), however, was important because it was the only detailed study found with more than one-point unsteady surface pressure measurements in a separating/reattaching flow geometry similar in nature to the present experiment (i.e., one with a very thin boundary layer at separation). Cherry *et al.* (1984) conducted two-point microphone measurements at different spacings on a splitter plate. Kiya and Sasaki (1983) also studied the flow state over a blunt-face splitter plate using extensive single- and two-point measurements of surface-pressure and velocity measurements. However, they displayed most of their data in velocity and velocity-pressure correlation plots. More recently, Lee and Sung (2001) also conducted unsteady surface pressure measurements using a 32-microphone array. However, their geometry was a backward-facing step, which as already explained in Section 1.2 has somewhat different flow characteristics from the splitter plate/fence configuration.

3.3 Root-Mean-Squared Pressure Fluctuations

The microphone array measures the spatial distribution of pressure fluctuations produced by the passage of various flow structures over the model. These fluctuations represent the deviation from the mean pressure value measured by the static pressure taps. The root-mean-squared (RMS) of the pressure fluctuations determines a measure of the 'average pressure deviation' from the mean pressure value (disregarding the sign of such a deviation). This average can be obtained for each microphone along the splitter plate. Additionally, the square of the RMS pressure fluctuations represents the energy of the unsteady pressure time series for a given microphone, thus the larger the RMS, the stronger the pressure fluctuation.

The current RMS measurements (plotted as $C_p = p'_{rms} / \frac{1}{2} \rho U_\infty^2$) are shown using circles in Figure 3.4, along with a trend line fit (solid line) and results from Cherry *et al.* (1984). The present data exhibit some scatter around the trend line, which is believed to be associated with the uncertainty of the microphone calibration procedure, which was found to be approximately 7%, as described in Section 2.1.3. The results shown in Figure 3.4 were obtained using the individual sensitivities of the microphones, determined from this calibration procedure. Comparison to the data from Cherry *et al.* (1984) in Figure 3.4 shows good qualitative agreement with the present data, although there is an offset as seen in the static pressure measurements. The offset is largest in the vicinity of the peak in the C_p values. As mentioned earlier, the difference between the two

plots could be due to the variation in the model geometries selected for each study.

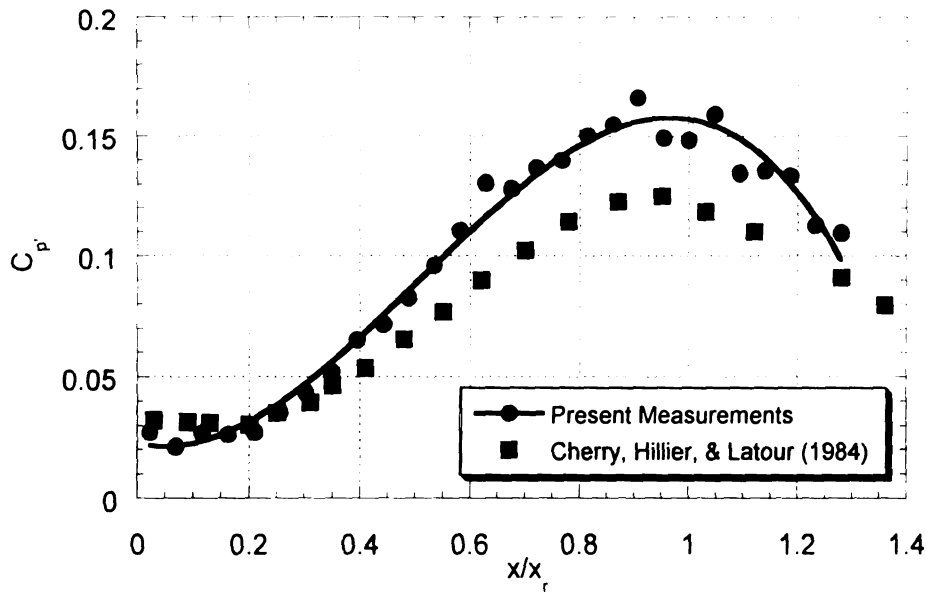


Figure 3.4 Streamwise distribution of the coefficient of RMS pressure fluctuations

At the point of separation, the shear layer is laminar and relatively far away from the splitter plate wall-pressure sensors. At this location, the microphones detect low RMS pressure fluctuations directly behind the fence. It is unknown what causes these pressure fluctuations, but it has been theorized in the literature that the unsteadiness, or 'flapping', of the shear layer may in fact produce some of the wall-pressure activity seen in this region. The region referred to is the distance from the fence up to about a quarter of the reattachment distance ($1/4x_r$), where the RMS values are relatively flat for both data sets shown in the graph. This area is significant and will be referred to in the upcoming sections.

t

f

t

c

T

in

(

th

H

m

re

er

do

sh

the

by

se

Pr

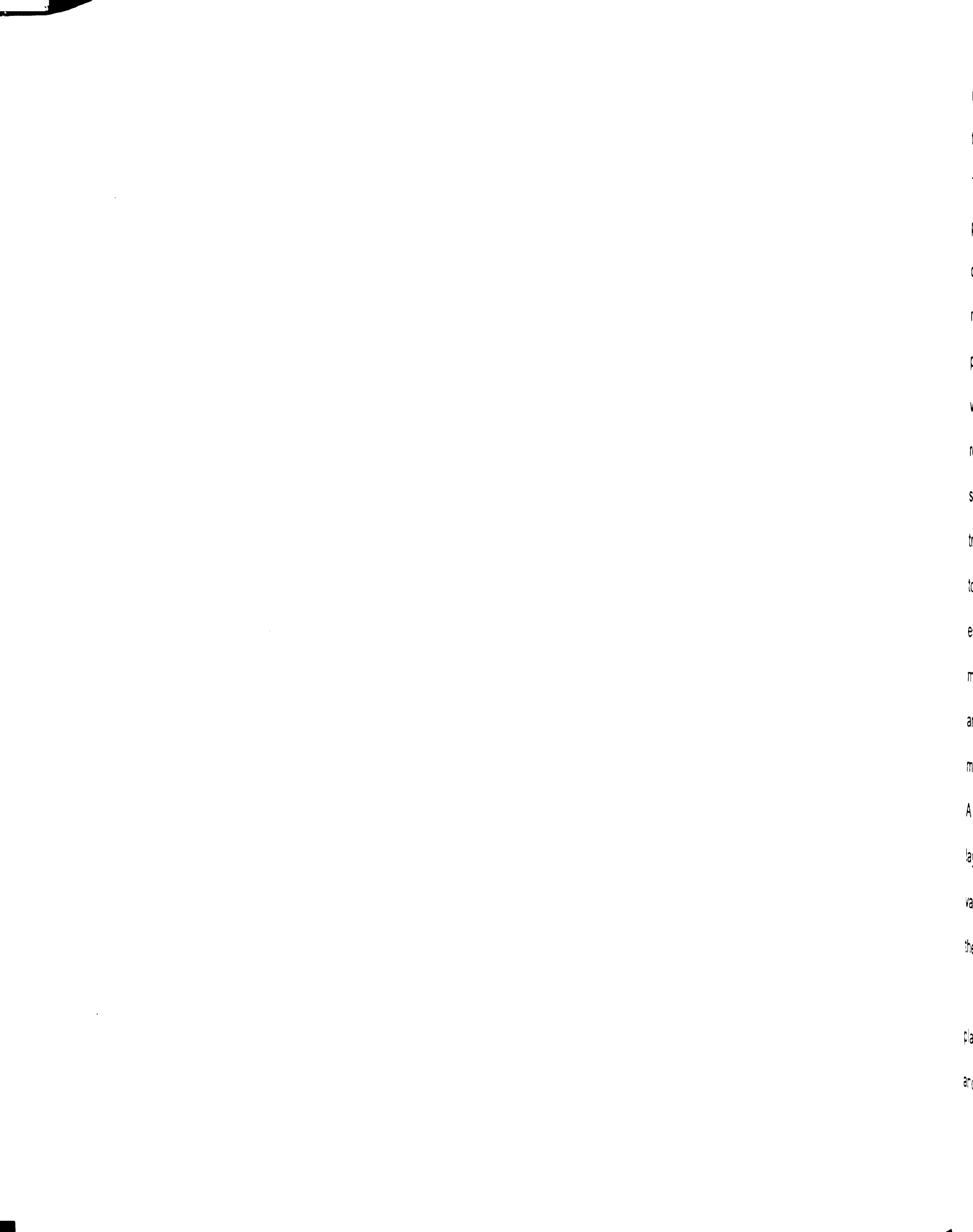
ca

On

Beyond $\frac{1}{4}x_r$, there is a rise in the RMS pressure fluctuations, as seen in both graphs in Figure 3.4. It is believed that in this region the surface pressure fluctuations are predominately associated with shear-layer vortical structures. As these structures convect downstream, growing in size and strength and moving closer to the wall, they produce an increasingly strong wall-pressure signature. This signature reaches a maximum level in the vicinity of where the flow impinges, or reattaches, on the plate as described by Farabee and Casarella (1986).

It is well documented that the peak RMS value occurs slightly upstream of the reattachment point in both splitter plate and backward-facing step studies. Heenan and Morrison (1998), in their backward-facing step study, found the maximum RMS value to occur approximately one-step height upstream of reattachment. Beyond reattachment, the RMS values decrease slowly as the energized turbulent structures from the shear layer decay and diffuse downstream. The flow then takes on boundary layer characteristics once the shear layer reattaches. Farabee and Casarella (1986) reported that, based on their backward-facing step study, high-frequency structures decay first followed by the low-frequency structures. Evidence of organized flow structures can be seen over 72-step heights downstream of the backward-facing step.

As the flow progresses downstream past the $\frac{1}{4}x_r$ region, the rise in the RMS value indicates the growing strength of the shear-layer vortical structures caused by the transition of the shear layer from a laminar to turbulent state. Cherry *et al.* (1984) also found this to be true in their surface pressure



measurements. Although using smoke visualization techniques, they observed that the beginning of the formation of shear layer vortices, which they called 'transition', was complete by $0.3D$ (D was the thickness of their blunt-faced plate), with the first visible signs of the shear-layer instability occurring at half that distance. This is in contrast to the $\frac{1}{4}x_r$ ($3H$) deduced from the beginning of the rise in the C_p results in Figure 2.3 for both the current and Cherry *et al.* data. A possible reason for this discrepancy between surface measurements and flow visualization is that the shear layer vortical motion is too far away in the $\frac{1}{4}x_r$ region to be resolved accurately through surface pressure measurements. More specifically, because the initial shear-layer structures at the beginning of transition are weak and located farther away from the wall, they may generate too weak a wall-pressure footprint to be detected by the surface sensors, especially in comparison to the strength of the low-frequency fluctuations measured within the region. Only when the energy of these structures has amplified through the shear-layer instability to a strong enough level will the microphones be able to record their associated turbulent pressure fluctuations. A more precise method of checking and/or identifying the starting point of shear-layer transition would be through the calculation of the RMS unsteady velocity values in the shear-layer from the PIV data, which will not be done in time for this thesis. However, that data will be presented in future papers.

Another interesting point concerning the differences between the splitter plate and backward-facing step studies was seen in the RMS data. In the Lee and Sung's (2001) backward-facing step, the C_p values started to rise rapidly



around $0.5x_r$. Heenan and Morrison (1998) saw the same in their backward-facing step. However, with the present splitter plate and fence configuration, the C_p value increases dramatically around $0.25x_r$. This suggests that the shear-layer transition starts earlier in the splitter plate/fence configuration than in the backward-facing step, assuming the boundary layer is laminar at separation.

A possible reason for this difference could be due to the thickness of the shear layer at separation. In the case of the splitter plate with fence, a thin, laminar, shear layer is formed at separation compared to the relatively thick separating boundary layer in the backward-facing step due to the boundary layer development on the top side of the step. A thin shear layer is subject to steeper velocity gradients and higher shear stresses than a thicker shear layer. Therefore, a thin shear layer is highly unstable and may transition earlier than a thick shear layer as it may be more susceptible to disturbances. It should be noted here that if the separating boundary layer is turbulent, in the backward-facing step case, the start of the shear layer transition refers to the beginning of the process leading to the roll-up of the shear layer and subsequent formation and development of vortical structures. This of course also takes place when the separating boundary layer is laminar; but in this case, it also causes transition from a laminar to turbulent state in addition, as mentioned earlier.

The source of the pressure fluctuations is another important point of discussion. Fricke (1971), using a theoretical approach, stated that the source of the surface pressure fluctuations appear to come from the shear layer above the re-circulation region. Cherry *et al.* (1984) support the idea that the main source

of the pressure fluctuations is associated with the downstream convection of the turbulent structures in the shear layer. These structures are smaller in scale than the reattachment length. This study supports the latter idea expressed by Cherry *et al.* (1984).

Figure 3.5 gives the RMS pressure fluctuations plotted as a function of the spanwise distance normalized by the width of the model between the endplates. The model centerline corresponds to $z/W = 0$ in this graph. The RMS pressure coefficients (C_p) at different spanwise locations were divided by the centerline value (C_{p0}) at the same streamwise location, for each of the four streamwise locations (represented using different symbols in Figure 3.5).

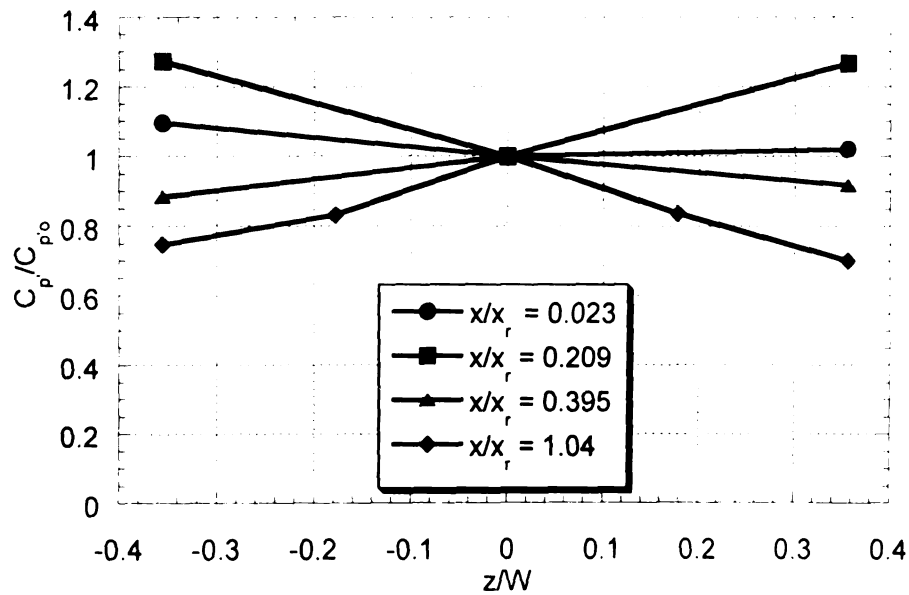


Figure 3.5 Surface-pressure RMS distribution in the spanwise direction

The graph in Figure 3.5 is used to check the two dimensionality of the fluctuating wall pressure field. These results are analogous to those obtained

earlier for the spanwise static pressure taps in Figure 2.25, except they relate to the unsteady rather than the steady component of the wall pressure. For a perfectly two-dimensional flow, the values seen in Figure 3.5 for all four microphones at a given streamwise direction should be 1. This is not depicted in Figure 3.5, except perhaps for the results closest to the fence (closed circles). The RMS pressure fluctuations measured at $0.35W$ away from the centerline seem to deviate anywhere between 10-30% from the centerline values. These deviations are substantially larger than those obtained in the C_p data (Figure 2.25), which exhibit very little deviation from two-dimensional behavior. Thus, the spanwise distribution of the RMS results suggests a flow field that is inherently more three dimensional than implied in the mean pressure data.

Ruderich and Fernholz (1986) studied the three-dimensional effects within a splitter plate/fence configuration. They found three-dimensional, secondary flow patterns within the circulating region as well as near reattachment. As discussed earlier, it is believed that the flow within the re-circulation zone does not alter the static pressure distribution measured at the wall from that observed along the separation streamline (stream surface). This is possibly why the three-dimensional, secondary motion within the reattachment zone does not cause a substantial deviation in the spanwise distribution of C_p from the two-dimensional behavior. On the other hand, the inherent time-unsteadiness of the separating/reattaching flow may cause jittering of the three-dimensional secondary-flow features leading to a more pronounced effect on the RMS pressure. The test model, however, was carefully designed and mounted so the

flow is symmetric about the centerline, resulting in a zero pressure or velocity change in the z (spanwise) direction at the centerline. This symmetry is evident in the data seen in Figure 3.5 (within the measurement uncertainty $\approx 7\%$). Thus, the flow can be described as a function of two spatial coordinates with the $\partial/\partial z$ derivative equal to zero for both pressure and velocity in the vicinity of the centerline. The same conclusion was made by Hancock (1999) who conducted surface shear and velocity measurements in a splitter-plate-with-fence configuration.

In Figure 3.5, results at $x/x_r = 0.209$ and 1.04 show the largest deviation from two-dimensionality as the distance from the center increases on either side. The deviation at $x/x_r = 0.209$ indicates a rise in the pressure fluctuations at the edges of the splitter plate compared to the centerline, whereas, farther downstream the pressure fluctuations are lower than that of the centerline. In the latter case, it has been reported by Cherry *et al.* (1984), through the cross-correlation of fluctuating pressures, that downstream close to reattachment, the flow appears to slowly become more three-dimensional. This can possibly cause the decrease in RMS values closer to the model edges at $x/x_r = 1.04$. At $x/x_r = 0.209$, however, the increase in pressure fluctuations could be caused by the corner vortices found in the study of Ruderich and Fernholz (1986). They showed, through a “mean footprint” using oil-flow pictures, a re-separation region occurring around $2.3h_f$ and the corner vortices within this region. The re-separation was associated with a secondary re-circulating bubble located upstream of the main re-circulating flow. The corner vortices seen in this region

were small with small rotation, directing the flow downstream. It seems possible that these corner vortices fluctuate with time, creating pressure fluctuations different from those seen at the centerline. These additional pressure fluctuations could cause the increase seen in the RMS values at $x/x_r = 0.209$ nearest to the endplates. Further experimentation is needed to verify this point.

3.4 Auto-correlation Analysis

The discrete-time auto-correlation is defined as

$$r_{p'p'}(n) = \frac{1}{N} \sum_{k_t=0}^{N-1} p'(k_t)p'(k_t - n) \quad (9)$$

where k_t represents the time index, n represents a time shift, or delay, and N is the total number of points measured in a time record, $p'(n)$. The correlation function from equation (9) provides an integral measure of the time scales of the signal $p'(n)$. This type of correlation can help identify regions dominated by short or long timescales.

To avoid the prohibitively long processing time associated with implementing equation (9) in the time domain, the correlation was computed using the Fast Fourier Transform (FFT). This method of calculation produces a circular correlation function because of the periodicity of the FFT. The circular correlation results nevertheless do agree with the results of equation (9) provided that the time delay (n) is small compared to the number of points in the time record (N). For the present data, the largest n value (n_{max}) of interest was approximately 1000. This value exceeded that required to capture the range of non-zero correlation values for the microphones with widest correlation extent

(those closest to the fence, as will be seen shortly). The corresponding record length was $N = 4096$. Hence, the ratio of n_{\max}/N was approximately 0.25, or 25%, which was sufficiently small to enable use of the circular correlation for calculating $r_{p'p'}$. This may be verified from Figure 3.6, which provides the auto-correlation results obtained for microphone #0 using the time and frequency domain methods. As seen, a very good agreement between the time- and frequency-results is obtained. The ordinate represents the normalized auto-correlation calculated using the following equation

$$R_{p'p'} = \frac{r_{p'p'}}{p'_{rms}^2} \quad (10)$$

where $r_{p'p'}$ is the individual auto-correlation function for each signal and p'_{rms} is the RMS value for that particular signal as calculated in Section 3.3. The abscissa represents the time shift ($\tau = n/f_s$, where f_s is the sampling frequency) normalized by the free stream velocity and the total fence height.

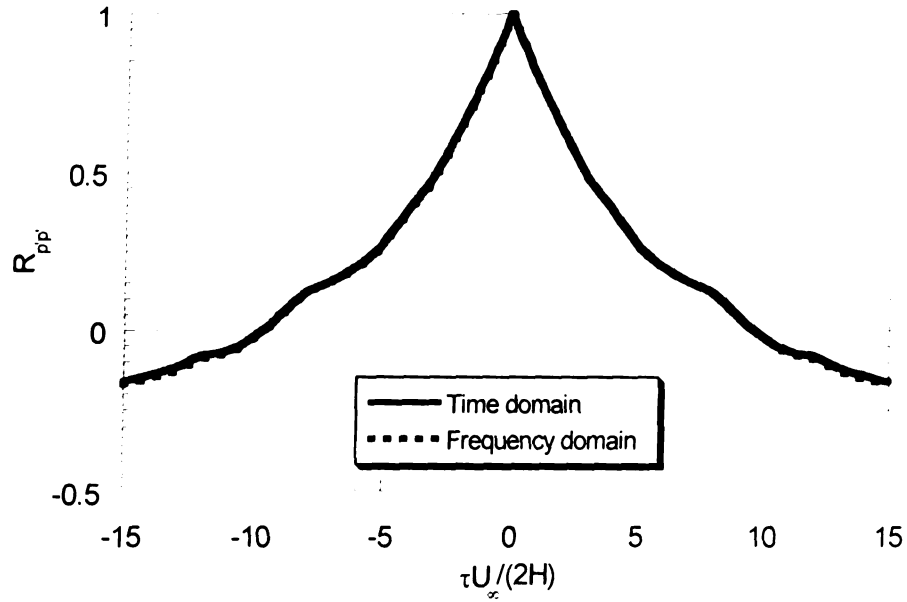


Figure 3.6 Comparison of the auto-correlation function computed in the time and frequency domain

Figure 3.7 shows the normalized auto-correlation for five different microphones, numbering 0, 4, 7, 21, and 27. Microphone #0 is located directly behind the fence. Microphones 4 and 7 are in a 'transition region', which will be explained in more detail shortly. Microphone #21 is the microphone nearest to reattachment and microphone #27 is the last microphone on the centerline. The corresponding streamwise locations of these microphones are $x/x_r = 0.02, 0.21, 0.35, 1.00, 1.28$ respectively. These specific microphones were chosen to highlight the change in the character of the auto-correlation function in the downstream direction. The vertical axis represents the normalized auto-correlation coefficient and the horizontal axis shows the dimensionless time shift.

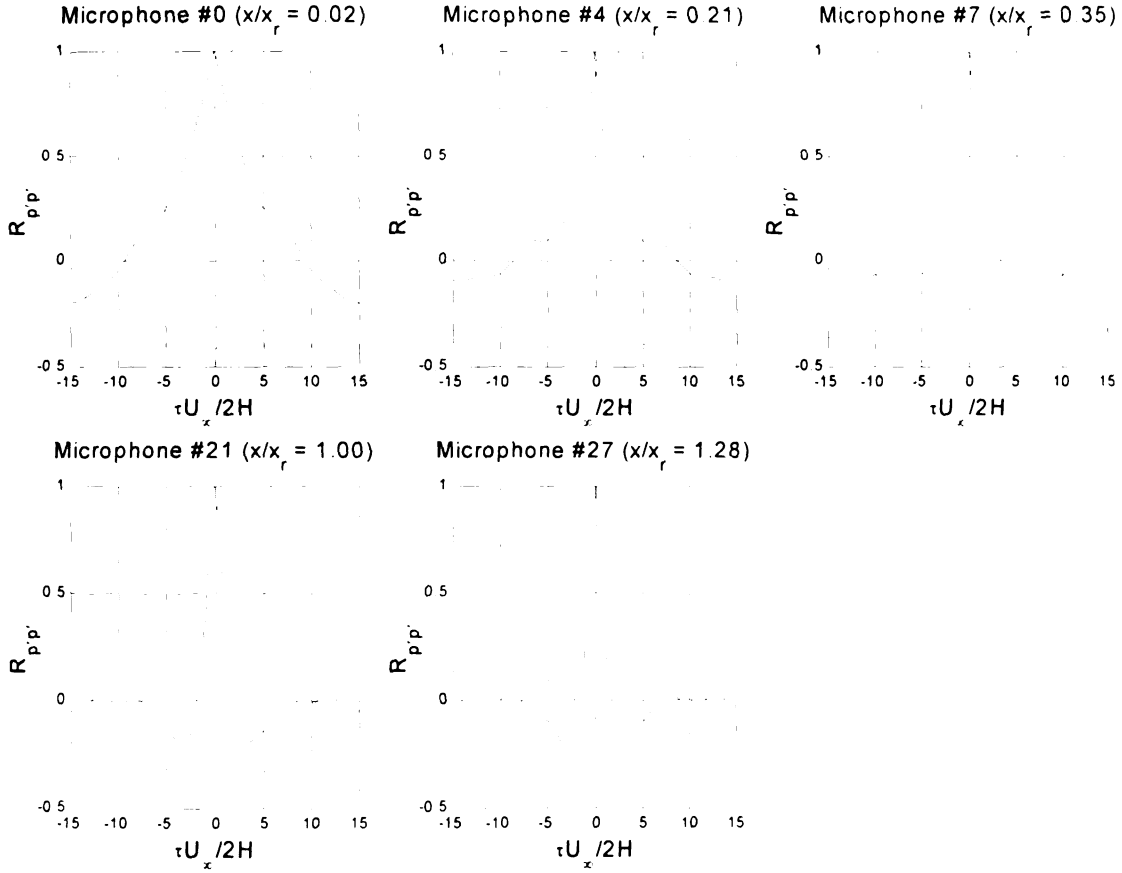


Figure 3.7 Auto-correlation function for microphones # 0, 4, 7, 21, and 27

For microphone #0 results, the area under the peak is wide. This area narrows farther downstream, as seen in the following four graphs. A wider $R_{p'p'}$ indicates dominance of longer timescales, or low frequencies, at that particular microphone. Hence, Figure 3.7 demonstrates a transition from a surface pressure signature that is dominated by large timescales to one that is dominated by shorter time scales with increasing streamwise coordinate. A more complete view of the dependence of the auto-correlation function on the streamwise distance is given by the gray-scale contour map in Figure 3.8 for all 28 centerline microphones.

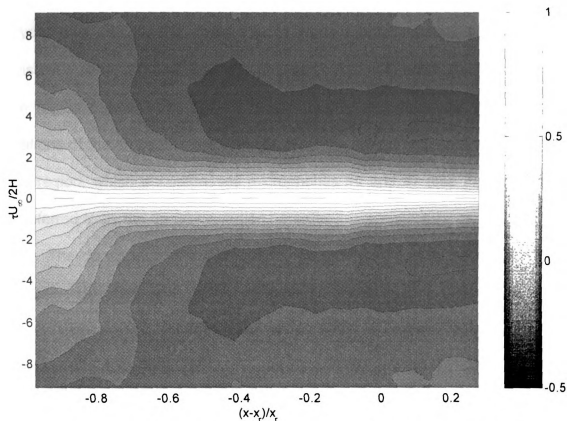


Figure 3.8 Contour map of the auto-correlation function for all 28 microphones along the centerline of the model

In the contour map, the abscissa shows the distance along the splitter plate with respect to the reattachment point, the ordinate shows the time shift normalized by the free stream velocity and the total fence height; and the color bar indicates the values of R_{pp} . The map makes it easier to see the transition in the auto-correlation width with downstream distance. In the region immediately behind the fence, the auto-correlation function extent is wide and changes very little up to a distance of about $0.2 - 0.25x_r$ ($x-x_r/x_r = -0.80$ to -0.75) behind the fence. Farther downstream, this width narrows significantly over a relatively short distance (roughly from $0.25x_r$ to $0.7x_r$; $x-x_r/x_r = -0.75$ to -0.30) as

demonstrated by the focusing of the $R_{p'p'}$ contours towards $\tau U_\infty/2H = 0$ line. Beyond this region, the contour lines remain approximately parallel to the constant τ lines showing very little change in $R_{p'p'}$ with additional increase in x . The region between $x/x_r = 0.25$ to 0.7 roughly delineates the start and end locations of the change in the time scales of the flow structures dominating $R_{p'p'}$. This region, which encompasses microphones #4 and #7 (see Figure 3.5), will be referred to as the transition region hereafter.

The dominance of low-frequency disturbances directly behind the fence has been identified in a number of studies. These include Castro and Haque (1987), Cherry *et al.* (1984), Driver *et al.* (1987), Eaton and Johnston (1981), Farabee and Casarella (1986), and Lee and Sung (2001). Some of these studies have attributed these disturbances to the flapping of the shear layer as discussed by Cherry *et al.* (1984). Farther downstream, the organized shear layer structures grow in strength and move closer to the wall. These more energized structures impose a shorter timescale, than that encountered close to the fence, on the auto-correlation function. Thus, the increasing influence of these structures on the wall pressure appears to be responsible for the observed change in $R_{p'p'}$ within the transition region. Past this region, in the vicinity of the reattachment location and farther downstream, the energy of the shear layer organized structures appears to saturate (e.g., as manifested in the RMS plot in Figure 3.4) then decrease slowly. This is possibly why no substantial change in $R_{p'p'}$ is detected past the transition zone.

To establish the change of the auto-correlation width on a more quantitative basis, a measure of the R_{pp} extent is computed for all 28 microphones. The results for this 'integral time scale' seen in Figure 3.9 were derived from the auto-correlation function. In particular, τ^* was determined by finding the time at which the negative peak in the auto-correlation occurred with respect to the ordinate and multiplying that time value by two. Because of the even symmetry of the auto-correlation, τ^* gives the time delay between the two negative peaks in the auto-correlation function. The resulting value was normalized and plotted along the ordinate as a function of the distance along the splitter plate with respect to the reattachment point in Figure 3.9. The displayed error bars represent the uncertainty in locating the peak, which stems from the fact that a narrow peak can be located more precisely than a broad peak in the presence of data scatter inherent to experimental data. Details of the error estimation are provided in Appendix D.

(19

me

sm

and

the

area

func

for

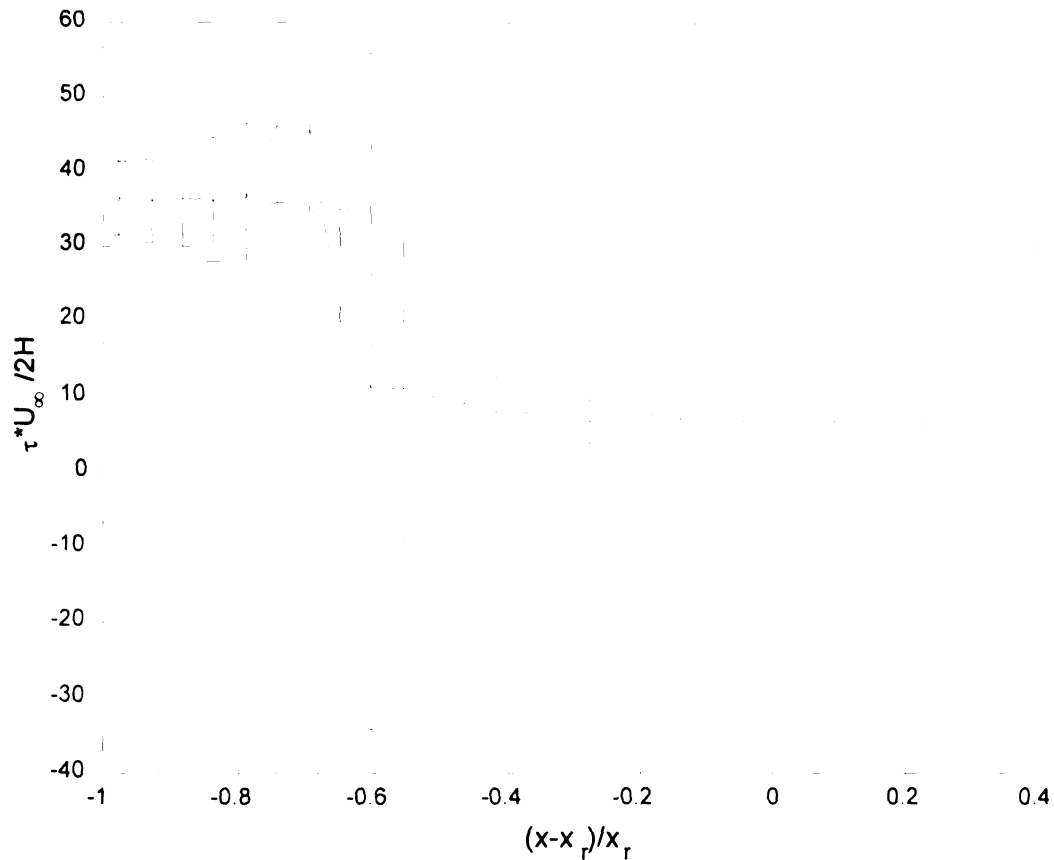


Figure 3.9 Streamwise variation of the integral time scale

Figure 3.9 is similar in nature to that produced by Castro and Haque (1987) using velocity measurements in the shear layer region. The measurements at the first five microphones show long time scales with relatively small error bars. This is the region closest to separation where other authors and this study have observed predominately low-frequency motions. Data from the next five microphones, associated with large error bars, are in the transition area. The error is expected to be high here because the auto-correlation functions in this region have a relatively flat negative peak along with data scatter (for example see $R_{p'p'}$ for microphone #7 in Figure 3.7). The remaining

m

o

m

th

tr

wl

be

sh

de

on

two

one

Re

met

reat

than

scale

could

microphones have shorter time scales with small error bars. This reaffirms the observations from the auto-correlation contour plot. That is, the signals from the microphones closest to separation are dominated by large time scales, whereas, the signals from the microphones farther downstream are dominated by smaller time scales. In between, there is a transition region starting roughly around $\frac{1}{4}x_r$, which is the same region seen in the RMS statistics. This region is believed to be associated with the amplification and streamwise development of the vortical shear layer structures.

The integral time scales can be calculated using another method that is defined based on finding where the function first crosses the abscissa ($R_{p,p'} = 0$) on either side of the ordinate axis and determining the time delay between these two points. Thus, the time delay was determined by interpolating τ at $R_{p,p'} = 0$ on one side of the abscissa axis and multiplying this τ by two due to the symmetry of $R_{p,p'}$. Figure 3.10 gives the normalized time scale (τ^*) plot calculated using the method described as a function of streamwise distance with respect to the reattachment length. Although the time scale values in Figure 3.10 are smaller than those found in Figure 3.9, the uncertainty in the calculation of the time scales for the transition region is reduced. This is because the axis crossing could be determined significantly more precisely than the negative peak location.

3.

ab

fre

ch

no

de

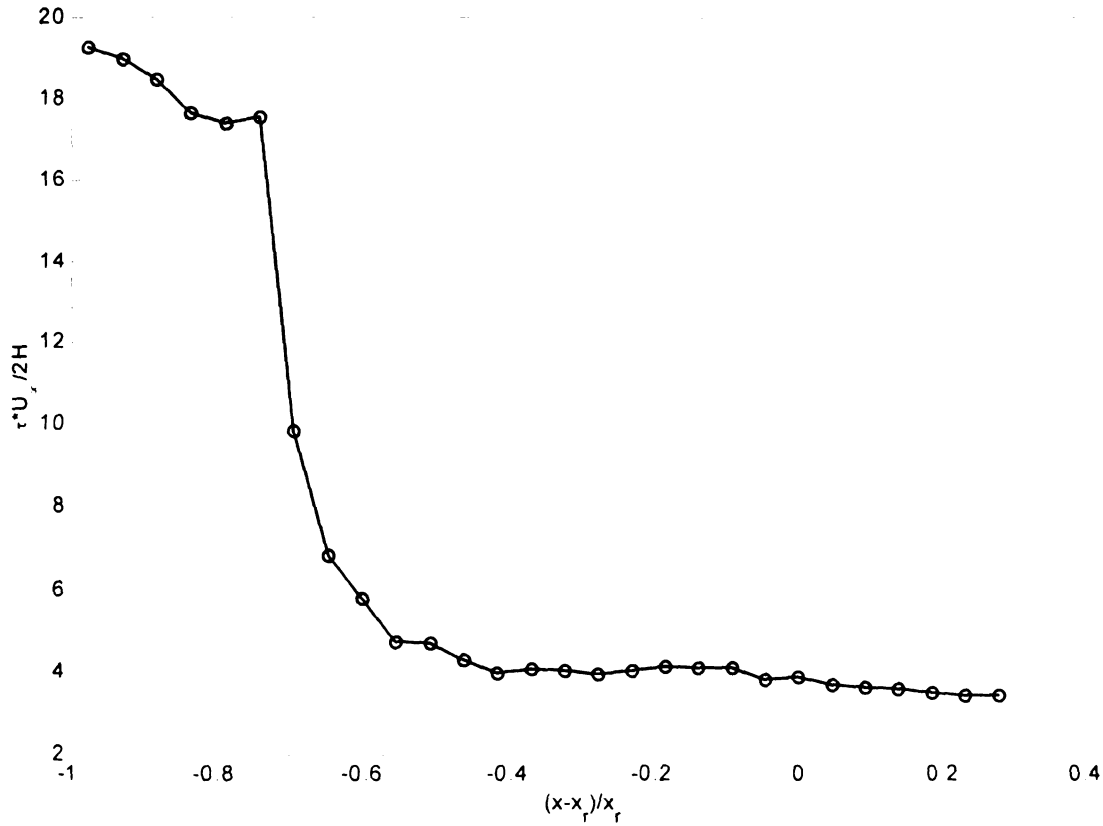


Figure 3.10 Streamwise variation of the integral time scale

3.5 Power Density Spectra

The power spectrum density function contains frequency information about a time signal. For example, the power spectrum can show which frequencies in the signal have the highest energy content. This can be useful in characterizing the frequency content of the pressure and velocity signatures of flow structures. The power density spectrum gives the average power in a periodic signal as a function of frequency and is calculated from

$$\phi_{p'p'}(k) = \left[\frac{1}{N_j} \left(\sum_{j=1}^{N_j} P'_j(k) (P'_j(k))^* \right) \right] \frac{a}{N^2}; k = 0, 1, \dots, \frac{N}{2} \quad (11)$$

where $P'(k)$ is the FFT of the signal, $p'(n)$, $(P'(k))^*$ is the complex conjugate of $P(k)$, k is the frequency index ($k = (f/f_s)N$, where f is the frequency associated with k and f_s is the sampling frequency), j is the record index, N_j is the total number of records, N is the total number of points in each record, and $a = 1$ for $k = 0$ and $N/2$ (DC and Nyquist frequencies) and $a = 2$ otherwise to form the one-sided spectrum. Each record contained 4096 points and the number of records totaled 40, resulting in a random error uncertainty of 15%. If desired, the uncertainty can be reduced by reducing the number of points per record and increasing the number of records.

The power spectra for microphones # 0, 4, 7, 21, and 27 in linear-logarithmic form are shown in Figure 3.11. The ordinate is linear and represents the power spectrum multiplied by the frequency, and normalized by $\frac{1}{2}\rho U_\infty^2$, the fence height, and the free stream velocity ($\gamma = [4\phi_p f(2H)]/[\rho^2 U_\infty^5]$). The abscissa shows the frequency normalized by the total fence height and the free stream velocity plotted on a logarithmic scale.

the
for
str
Th
in
ear
hav
mos
arou

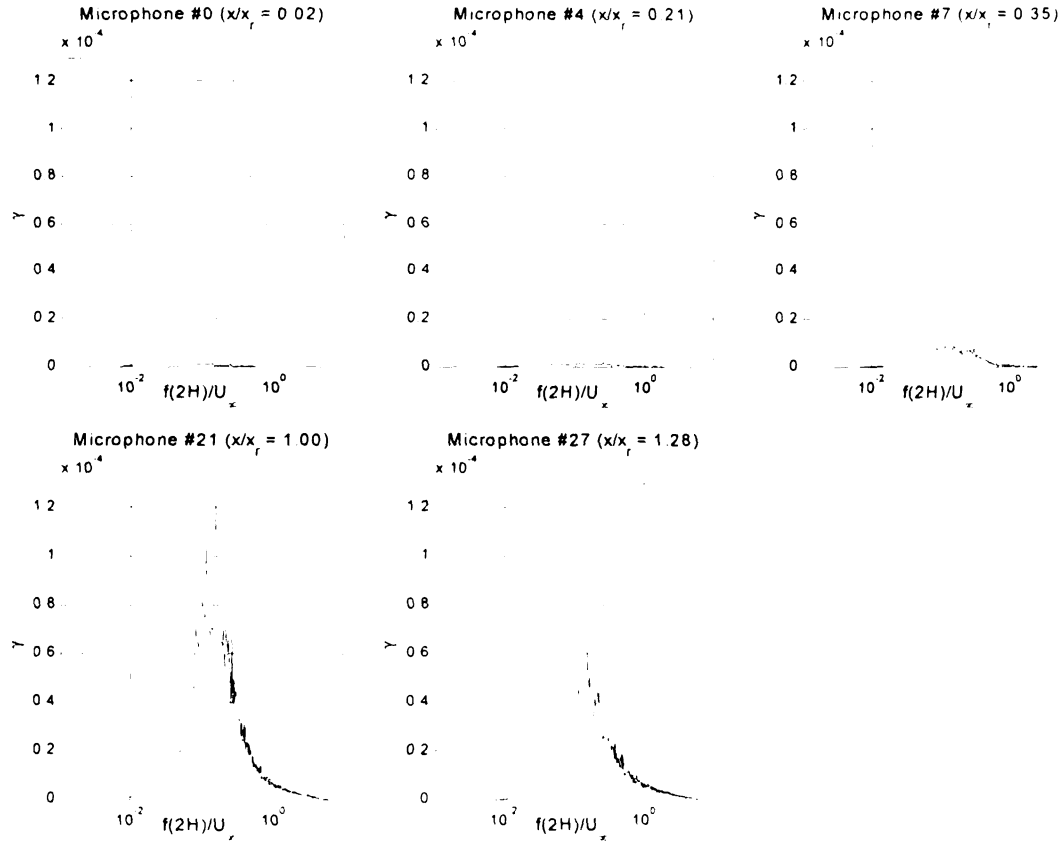


Figure 3.11 Power Spectra for microphones # 0, 4, 7, 21, and 27

The advantage of plotting the spectra in the format given in Figure 3.11 is that the geometrical area under a given curve represents the energy in the signal for that particular microphone, which is also representative of the strength of the structure within the flow region affecting the measured pressure fluctuations. The results show an increase in energy up to reattachment and then a decrease in energy beyond reattachment. This is identical to the RMS results presented earlier in section 3.3. Previous authors have described the power spectra as having overall low-energy content levels close to the point of separation that is mostly concentrated at low frequencies. At these low frequencies, roughly around $f2H/U_\infty = 0.02-0.03$ in the present study (See spectrum for microphone

#

b

v

v

th

M

M

th

th

st

(1

wa

of

the

be

str

mo

fre

the

the

total

pow

#0) and in Cherry *et al.* (1984), there is a broad peak. In the case of the backward-facing step, Lee and Sung (2001) also found a similar peak frequency value close to separation at $fH/U_\infty = 0.015$ (H = the height of the step), which when scaled by x_r instead gives a value of $fx_r/U_\infty = 0.11$. This is comparable to the values given by Spazzini *et al.* (2001) at $fx_r/U_\infty = 0.08$ and Heenan and Morrison (1998) at $fx_r/U_\infty = 0.1$. Cherry *et al.* (1984) along with Heenan and Morrison (1998), Driver *et al.* (1987), and Lee and Sung (2001), have associated this low-frequency peak with the flapping of the shear layer. Flapping refers to the unsteadiness of the reattachment point location, which results in the shortening and lengthening of the separation bubble. Farabee and Casarella (1986) suggested that the energy distribution in the spectra indicates that the wall pressure fluctuations close to separation were caused by the unsteadiness of the low-speed re-circulating flow, rather than the highly turbulent structures in the shear layer. This is consistent with the fact that these structures are only beginning to develop in this region and are most likely weak compared to the strength of the low frequency disturbance produced by the shear layer movement.

Farther downstream, the energy in the spectrum is located at higher frequencies as seen in the spectra for microphones #7, 21, and 27. In particular, the peak in the spectrum occurs around $f2H/U_\infty = 0.1$, which is in agreement with the findings of Cherry *et al.* (1984), where their frequency is normalized by the total width of the splitter plate in their case. Lee and Sung (2001) stated that the power spectrum reaches a maximum at $fH/U_\infty = 0.068$, or $fx_r/U_\infty = 0.5$. Spazzini

e

N

re

th

tr

p

pl

sp

fre

an

sp

sh

sh

me

an

not

con

ln

mo

be

Fur

con

et al. (2001) found their maximum at $fx_r/U_\infty = 1.0$ along with Heenan and Morrison (1998). Driver *et al.* (1987) recorded a peak value close to reattachment of $fx_r/U_\infty = 0.6$. This higher frequency peak has been attributed to the highly turbulent structures within the shear layer, as discussed previously.

The following two figures (3.12 and 3.13) show the detailed evolution of the wall-pressure spectra with downstream distance. These figures contain the power spectrum plots on a logarithmic scale for both axes. The ordinate is plotted relative to an arbitrary reference value and represents the power spectrum normalized by the square of $\frac{1}{2}\rho U_\infty^2$ and the abscissa represents the frequency normalized by the fence height and free stream velocity. The use of an arbitrary reference value for the ordinate provided a means by which many spectrum plots can be shown on the same graph without clutter. Figure 3.12 shows the spectra for the first 27 microphones along the centerline. Figure 3.13 shows only every third microphone along the centerline. The latter figure magnifies the spectra plots in order to get a closer look at the spectrum details and the shift in the peak frequency in the downstream direction. It should be noted here that the observations made from the power spectrum analysis are consistent with those discussed earlier in regard to the auto-correlation function. In particular, the transition in the time scale of the wall-pressure generating motion from large to small with streamwise distance behind the fence appears to be associated with transition from a low to a high frequency motion. Furthermore, it is interesting to compare the τ^* values obtained from the auto-correlation to the spectral peak frequencies. This comparison is possible

because of the inverse relationship between time and frequency ($f = 1/t$). For large time scales, the τ^* value close to the fence was determined to be $\tau^*U_\infty/(2H) = 36.7$; thus the frequency is $f(2H)/U_\infty = 0.027$, which is similar to the low-frequency peak found in the power spectra ($f(2H)/U_\infty = 0.02-0.03$). The case is the same for the smaller time scales farther downstream where the τ^* value is $\tau^*U_\infty/(2H) = 6.8$, resulting in a frequency of $f(2H)/U_\infty = 0.147$ compared to the $f(2H)/U_\infty = 0.1$ high-frequency peak from the power spectra. Castro and Haque (1987) obtained velocity auto-correlation measurements at various positions in the shear layer using a pulsed-wire anemometer. From their results, they determined the time scale near separation to be 8 when normalized with the reattachment distance. This value compares well with the $\tau^*U_\infty/(x_r) = 6.8$ value calculated in the present study, which was determined from surface-pressure auto-correlation measurements. The discrepancy could be due to the difference in the measuring techniques and/or the location where the data were recorded.

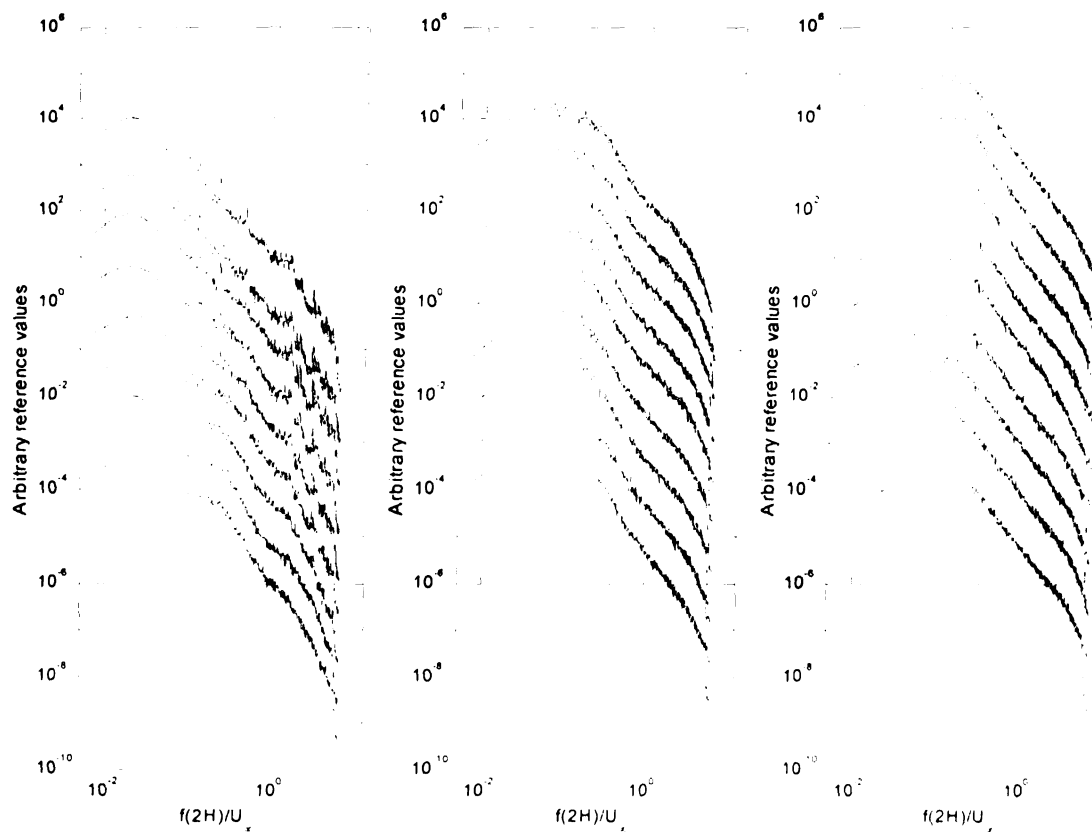


Figure 3.12 Power Spectra in logarithmic form for the first 27 microphones along the centerline of the model – streamwise direction is from top to bottom

3
re

by

Wt

a

US

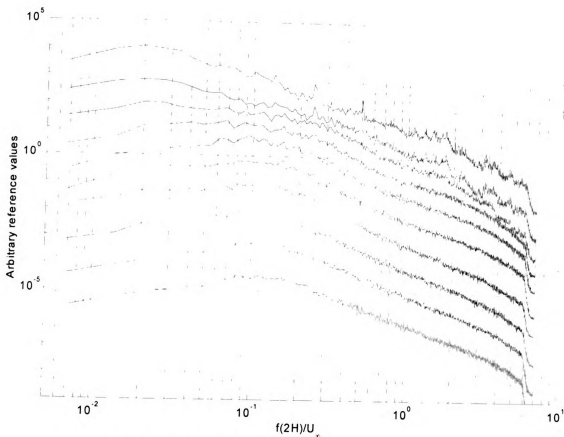


Figure 3.13 Power Spectra for selected microphones covering the measurement range - streamwise direction is from top to bottom

3.6 Cross-Correlation with respect to measurements at reattachment

The discrete-time cross-correlation function between two signals is given by the following equation:

$$r_{p'_1 p'_2}(n) = \frac{1}{N} \sum_{k_t=0}^{N-1} p'_1(k_t) p'_2(k_t - n) \quad (12)$$

where p'_1 and p'_2 are two different discrete-time signals, k_t is the time index, n is a time shift, and N is the number of points sampled. The cross-correlation is used to determine the similarity between two different signals. If the two signals

are identical (i.e. $p'_1(n) = p'_2(n)$), equation (12) yields the auto-correlation function, calculated earlier using equation (9). The cross-correlation was normalized, similar to the auto-correlation, using the RMS value of p'_1 and p'_2 .

$$R_{p'_1 p'_2} = \frac{r_{p'_1 p'_2}}{(p'_{1,rms})(p'_{2,rms})} \quad (13)$$

where $r_{p'_1 p'_2}$ is the cross-correlation and $p'_{1,rms}$ and $p'_{2,rms}$ are the RMS pressure fluctuations for the two different discrete-time signals.

Prior to presenting results for all 28 microphones, it is necessary to examine the consistency of the current measurements with data from the literature. To this end, the cross-correlation function obtained from five different microphones correlated with the microphone closest to reattachment was calculated and compared to similar results from Cherry *et al.* (1984). The locations of these microphones are given in Table 3.1. Note that the results obtained for the microphone at $x/x_r = 1$ represents the auto-correlation function (since the reference microphone in the cross-correlation is located at x_r). Figure 3.14 shows the cross-correlation results for the five microphones compared with the data from Cherry *et al.* (1984). The abscissa gives the time shift normalized by the free stream velocity and the total fence height; whereas, the ordinate represents the cross-correlation coefficient.

Table 3.1 Microphone positions used in cross-correlation analyses

	Present Study – x/x_r	Cherry <i>et al.</i> – x/x_r
1	0.54	0.55
2	0.65	0.70
3	0.95	0.95
4	1.0	1.0
5	1.3	1.4

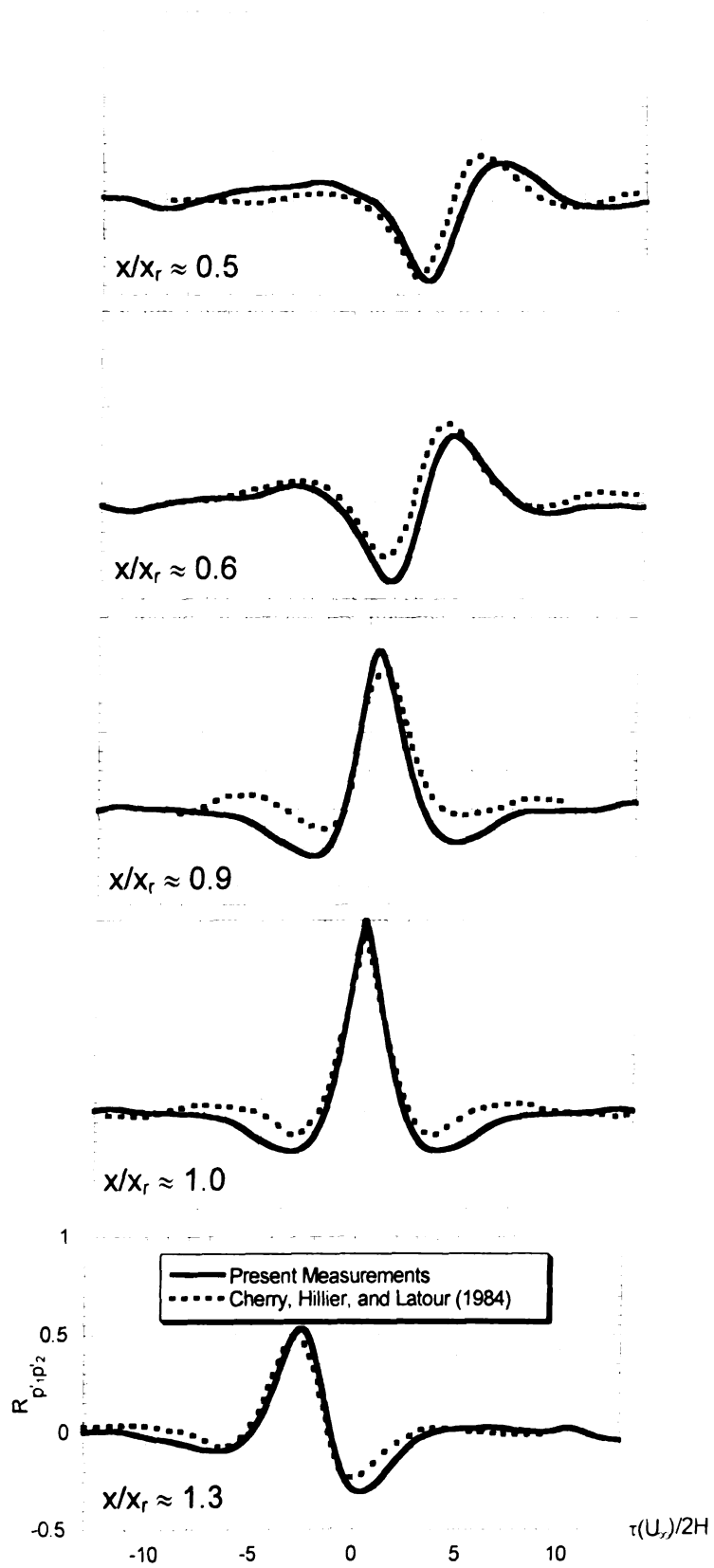


Figure 3.14 Cross-correlation results at five different locations compared to data from Cherry *et al.* (1984)

The data in Figure 3.14 compare well with the data from Cherry *et al.* (1984), who characterize the data as a manifestation of “clear convective motion in the mainstream direction.” The convective motion is implied from the shift in the location of the correlation peak for microphones located at different x positions. For example, the positive correlation peak is seen to shift towards lower time delays with increasing streamwise coordinate of the microphone. The advantage of this study compared to Cherry *et al.* (1984) is the use of the microphone array, allowing the cross-correlation of the signals from all 28 microphones with that from the microphone closest to reattachment to be presented. This paints a more detailed picture of the spatial structure of the cross-correlation. Figure 3.15 shows a gray-scale contour map (similar to that used to present the auto-correlation data earlier in Figure 3.8) of the cross-correlation for all 28 microphones. The abscissa is the distance along the splitter plate with respect to the reattachment location and the ordinate is the time shift normalized by the free stream velocity and the total fence height. The color bar indicates the magnitude of the cross-correlation function.

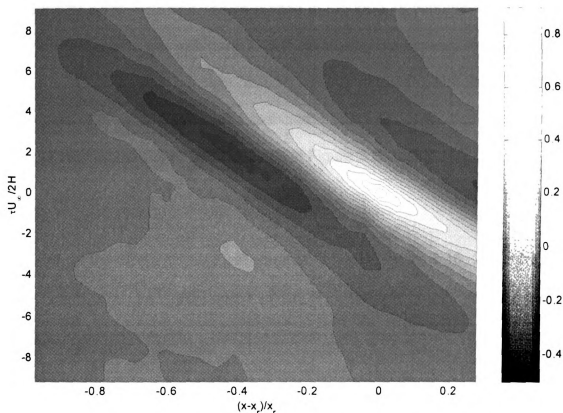


Figure 3.15 Cross-correlation color contour map for all 28 centerline microphones (reference microphone closest to reattachment)

In the cross-correlation contour map, there is a main, positive peak inclined at an angle and two negative lobes on either side of the main lobe. At each x location, the main peak is centered around time shift values corresponding to the largest positive correlation between the wall pressure signal at this x location and that at reattachment. The negative peaks give the time delay to the highest negative correlation. By finding the slope of the main (or negative) peak, an average downstream convective velocity can be calculated for the flow structure dominating the generation of surface pressure fluctuations. In order to find the slope, the coordinates of the positive-lobe peaks in the

contour plot were extracted and re-plotted in Figure 3.16 with the same axes as used in the contour plot in Figure 3.15. Calculating the convective velocity from Figure 3.16 gives the average velocity of the dominant turbulent structures regardless of their time scales (frequencies). This velocity is calculated from the slope of the least-squares line fit, shown in Figure 3.16, using

$$\frac{1}{U_c} = \frac{m_s(2H)}{U_\infty x_r} [(m/s)^{-1}] \quad (14)$$

where m_s is the slope of the least-squares fit line in Figure 3.16, $2H$ is the total fence height, x_r is the reattachment length, U_∞ is the free stream velocity, and U_c is the convection velocity. Using equation (14), the convective velocity was determined to be 57% of the free stream velocity. Heenan and Morrison (1998) reported, using two flush-mounted pressure transducers in their backward-facing step configuration, convective velocities ranging between $0.5U_\infty$ and $0.6U_\infty$ depending on the position along the model. Lee and Sung (2001) stated that convective velocities at high frequencies converged to a value of $0.6U_\infty$ in their backward-facing step study, using a 32-microphone array. Hwang *et al.* (2000) estimated the average convective velocity in their blunt-faced flat plate to be approximately $0.5U_\infty$ based on flow visualizations using a high-speed camera with high framing rates. Cherry *et al.* (1984) determined the convective velocity to be $0.5U_\infty$ from pressure-pressure cross-correlations. Their pressure data were recorded using two microphones at different spacings. Generally, the convective values were cited to range from 0.5 to 0.6 of the free stream velocity in the literature, depending on model geometry, location of measurement, and

3.

av

arc

fre

fre

by

sig

measuring technique. However, consideration of the results cited above suggests that the convective nature of the dominant structures in the splitter plate/fence flow is more similar to the backward-facing step, than to the blunt-facing plate.

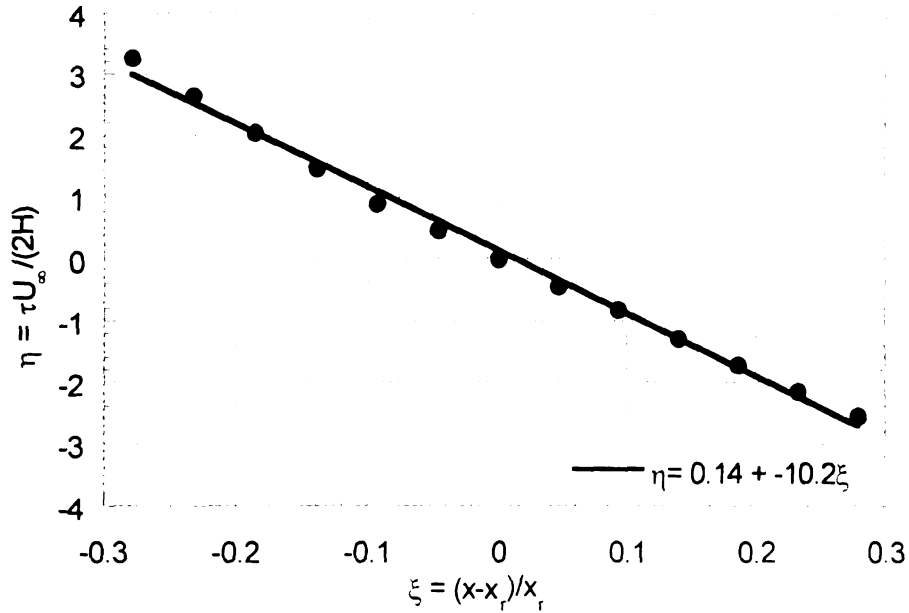


Figure 3.16 Convection velocity plot for the cross-correlation contour plot from Figure 3.15

3.7 Phase, Coherence, and more on Convection Speeds

As previously mentioned, the cross-correlation is used to estimate an average of the convective velocities associated with various time scales. In order to determine the convective velocities at individual time scales (frequencies), a phase plot can be used. The phase angle (θ) at a given frequency is computed from the cross-spectrum ($\phi_{p'1p'2}$) of two signals measured by two microphones. More specifically, the one-sided cross-spectrum of two signals, p'_1 and p'_2 , is calculated from

V

C

t

f

d

W

O

Te

m

C

fr

de

Si

be

Wh

an

$$\phi_{p'_1 p'_2}(k) = \left[\frac{1}{N_j} \left(\sum_{j=1}^{N_j} P'_{1,j}(k) (P'_{2,j}(k))^* \right) \right] \frac{a}{N^2}; k = 0, 1, \dots, \frac{N}{2} \quad (15)$$

where P'_1 is the FFT of $p'_1(n)$, P'_2 is the FFT of $p'_2(n)$, superscript $*$ indicates complex conjugate and the summation denotes record averaging. Moreover, k is the frequency index, with the corresponding frequency given by $(k/N)f_s$, and $a = 1$ for $k=0$ and $N/2$ (DC and Nyquist frequencies) and $a = 2$ otherwise. The angle of $\phi_{xy}(k)$ as a function of frequency is then computed from

$$\theta(k) = \tan^{-1} \frac{\text{Im}(\phi_{p'_1 p'_2}(k))}{\text{Re}(\phi_{p'_1 p'_2}(k))}; k = 0, 1, \dots, \frac{N}{2} \quad (16)$$

where Im and Re denote the imaginary and real components, respectively, of $\phi_{p'_1 p'_2}$. When θ is calculated for all microphones, with respect to a particular reference microphone, the resulting variation in θ at a given frequency with microphone location (streamwise distance) provides information concerning the convection velocity at that frequency (this will be shown later).

However, before presenting the results for the phase plot, the range of frequencies for which reliable phase information can be calculated must be determined. This is accomplished by computing the coherence between the two signals for which the phase plot is to be obtained. The one-sided coherence between two signals is defined as follows:

$$\Gamma_{p'_1 p'_2}(k) = \frac{\phi_{p'_1 p'_2}(k)}{\sqrt{\phi_{p'_1 p'_1}(k) \phi_{p'_2 p'_2}(k)}}; k = 0, 1, \dots, \frac{N}{2} \quad (17)$$

where $\phi_{p'_1 p'_2}$ is the one-sided cross-spectrum between the two signals and $\phi_{p'_1 p'_1}$ and $\phi_{p'_2 p'_2}$ are the corresponding one-sided power spectra. The coherence gives

v
a
v
f
f
a

s
p
co

an
cl
dr
co
an
mi
mi
Fig
thu
par

a measure of the 'phase locking' between two signals at a particular frequency. If the signals are perfectly correlated across all frequencies, then the coherence value will be 1 over the entire range. The highest value in a coherence plot is 1 and any value below 1 can be viewed as a percentage. In general, a coherence value larger than 50% at a certain frequency is indicative of the existence of a fairly well defined phase between the two signals at that frequency. Thus, for frequencies where $\Gamma_{p_1 p_2} < 0.5$, the calculated phase values may not be reliable and will generally be randomly scattered.

Traditionally, coherence is calculated between one microphone and a series of microphones farther downstream. Figure 3.17 presents the coherence plot at four different microphones along the centerline: 1, 8, 17, and 27. The coherence was determined between these four microphones and microphone #0. As seen in the Figure 3.17, there is high coherence between microphone #0 and microphone #1, which is expected because the two microphones are in close proximity with respect to one another. Farther downstream, the coherence drops off quickly as seen in the remaining three plots. Therefore, one cannot be confident in the validity of the phase angles calculated between microphone #0 and microphones farther downstream. Nonetheless, because an array of microphones was used to collect data, the phase angle between neighboring microphones can be determined with high confidence. This is demonstrated in Figure 3.18, which shows the coherence for neighboring microphones (numbering 0 and 1, 7 and 8, 16 and 17, and 26 and 27) to be high over a particular frequency range.

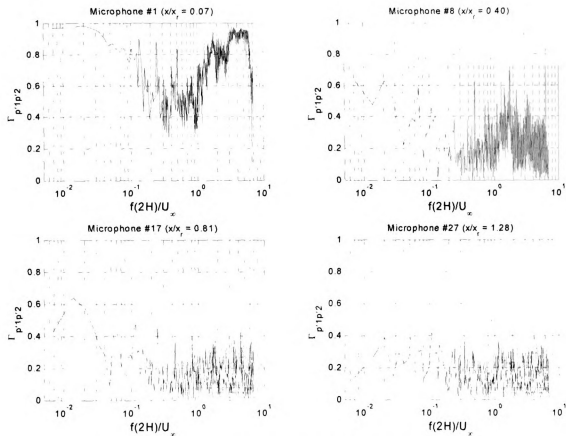


Figure 3.17 Coherence plot for four different microphones referenced to microphone #0

ad

fre

0.1

0.4

a g

ne

Wi

ran

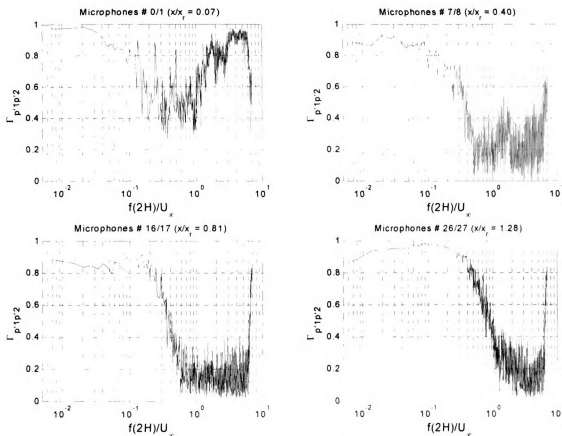


Figure 3.18 Coherence plot for four neighboring pairs of microphones

The coherence plots in Figure 3.18 reveal that the signals measured by adjacent pairs of microphones are not coherent (phase-locked) across all frequencies. In fact, there is a sharp drop off in the coherence around $f2H/U_\infty = 0.15$, immediately behind the fence. This value increases with x up to $f2H/U_\infty = 0.4$ at $x/x_r = 1.28$. This drop-off is seen in all four coherence plots, which provide a good representation of the high-coherence frequency range found for any two neighboring microphones along the centerline. Therefore, the phase analysis will be conducted using neighboring microphones and will be constrained to the range up to $f2H/U_\infty = 0.3$ (this falls roughly in the middle of the range $f2H/U_\infty =$

0.15-0.4). It should be noted here that this frequency range contains the low- and high-frequency peaks identified earlier in the power spectrum behind the fence and farther downstream, respectively. Thus, all the flow structures of interest to the surface-pressure generation process are contained within the frequency range where high coherence is seen for two neighboring microphones.

Because of the use of pairs of neighboring microphones in calculating θ , there was no phase angle change greater than π between two signals at any frequency. This was confirmed by estimating the representative wavelength ($\lambda = U_o/f$) of the flow structures dominating the surface pressure measurements to be about $25h_f$, using the high-frequency peak $f(2H)/U_\infty = 0.1$ and the average convection velocity, $0.57U_\infty$. Since the space between neighboring microphones is approximately $1h_f$, the phase angle difference between the two microphones would be, in the representative wavelength case, roughly $2/25\pi$. Hence, there was no need to unwrap the angles, which means to add multiples of $\pm 2\pi$ to the calculated phase angle. Large microphone separation causes the calculated phase angle between the two distant signals to fall outside the fundamental interval $[-\pi, \pi]$. This interval is set by the phase angle algorithm that utilizes a four-quadrant inverse tangent function. The function calculates the inverse tangent of complex signals, using the signs of the imaginary and real part of the signal to determine the appropriate quadrant. Thus, the calculated phase angle can be ambiguous within multiples of 2π . This is often the case when determining the phase angle difference between a microphone upstream (microphone #0) and consecutive microphones downstream of #0 because the

phase shift increases with increasing microphone separation distance. In the case of neighboring microphone pairs, the phase angle between these two signals is always small within the closed interval $[-\pi \pi]$ due to the close proximity of the microphones relative to the convective motion scale (wavelength). Nonetheless, by adding these phase angles between neighboring microphone pairs together moving in the downstream direction, the phase angle shift relative to microphone #0 can still be determined. Therefore, both methods can be used to determine the phase shift between, for example, microphone #0 and all microphones farther downstream, but the neighboring pair method requires no unwrapping and has a higher level of confidence according to the coherence plot shown in Figure 3.18.

Figure 3.19 displays a plot of the phase angle obtained using neighboring pairs of microphones as a function of the distance along the splitter plate for five different frequencies. The phase angles in the plot are calculated in reference to microphone zero for five different frequencies spanning the high-coherence frequency range. The distance along the splitter plate is referenced to the reattachment location.

a

di

de

co

ve

m

dir

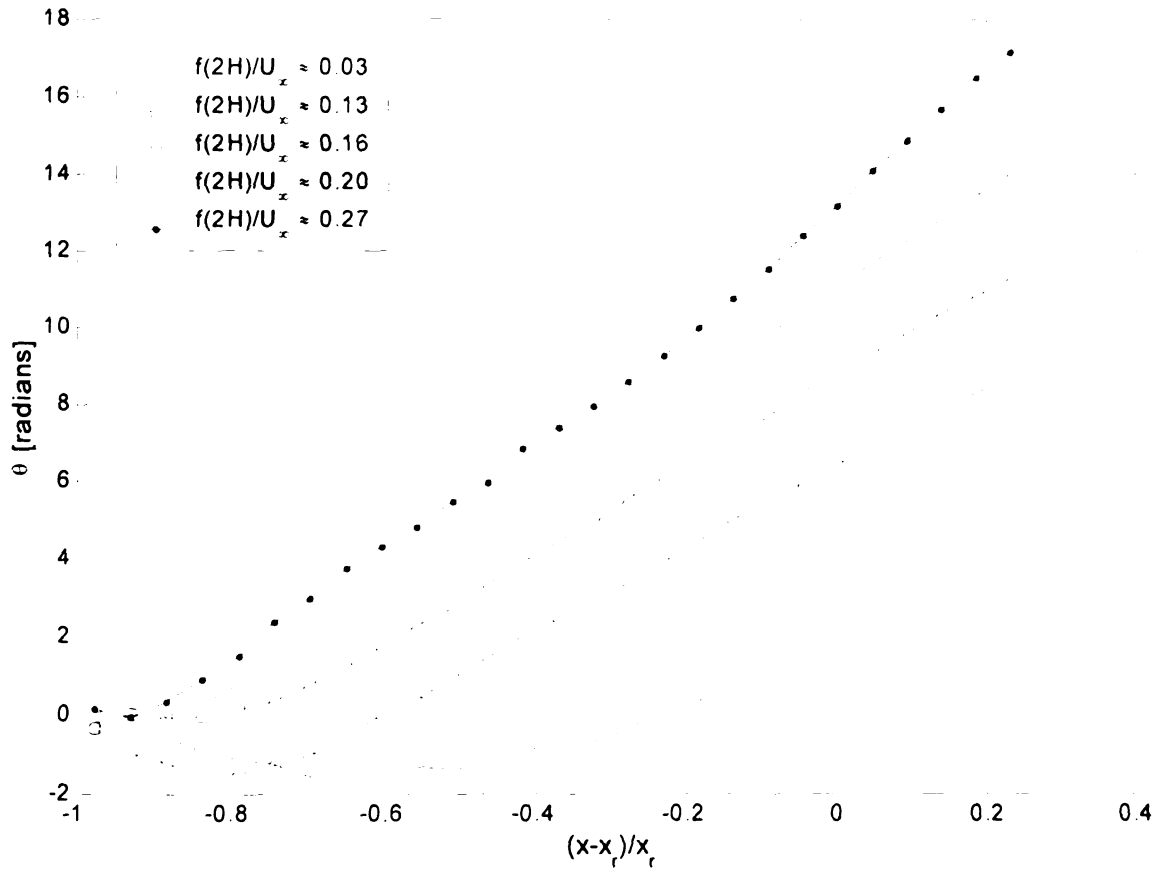


Figure 3.19 Streamwise development of the phase angle for five different frequencies (reference microphone at $x/x_r = 0.023$)

Except for the small region $x/x_r < 0.8$ in Figure 3.19, the phase plot reveals a steady, linear-like positive increase of the phase angle in the downstream direction for the four largest frequencies. The slopes of these lines differ, depending on the frequency. This indicates that there is a difference in the convective velocities corresponding to different frequencies. The convective velocity can be calculated by determining the slope as demonstrated below. The mathematical model of an ideal one-dimensional traveling wave in the positive x direction is as follows:

$$w(x, t) = A \cos(\omega t - bx) = A \cos(\omega t - \theta) \quad (18)$$

v

f

n

n

b

c

H

S

T

x₂

2-

th

Fi

reg

ab

be

by

con

where $\omega=2\pi f$ (f being the wave frequency in Hz) represents the wave angular frequency in radians/seconds, t and x represent time and space coordinates, respectively, θ represents a phase angle, $b=2\pi/\lambda$ (λ being the wavelength) represents the wave number, and A is the wave amplitude. The relationship between frequency and wavelength is given by $\lambda=c/f$, where c is the wave, or convection, speed. Therefore, the traveling wave equation can be rewritten as

$$w(x,t) = \cos\left(2\pi ft - 2\pi f \frac{x}{c}\right) \quad (19)$$

Hence, the difference in the wave phase angle between any two points that are spaced a distance x apart is given by the following equation.

$$\theta = 2\pi f \frac{x}{c} \quad [21] \quad (20)$$

Thus, by plotting the phase of a wave with respect to a reference point (say at x_0), as a function of x , the phase variation will be linear with a slope given by $2\pi f/c$. One may then determine the convection velocity (c) from knowledge of the wave frequency and the slope of the line. In this same manner, the plot in Figure 3.19 was used to determine c for different frequencies. A couple of points regarding this calculation should be noted here: (1) the line fit was restricted to about $(x-x_r)/x_r \geq -0.6$ where the phase characteristics behaved linearly, and (2) because the horizontal axis is normalized by x_r , the calculated slope was divided by x_r to convert to physical units. The following equation is used to calculate the convective velocity from the phase plot.

$$c = \frac{2\pi f x_r}{\Delta\theta / \Delta x} \quad (21)$$

where $\Delta\theta/\Delta x$ is the slope deduced from the phase plot using a least-square line fit. The convective velocities for the different frequencies are given in Table 3.2. Averaging the five convective velocities gives $0.47U_\infty$, which differs from the convective velocity $0.57U_\infty$, determined from the cross-correlation. This difference could be due to the fact that the velocities used in the average are not weighted by the relative dominance (energy) of the associated pressure fluctuations.

Table 3.2 Convective velocities for various frequencies

$f(2H)/U_\infty$	U_c/U_∞
0.03	0.21
0.13	0.45
0.16	0.50
0.20	0.55
0.27	0.64

The use of the pairs of neighboring microphones to calculate the phase raises the possibility of having phase accumulation error; however, this is only a concern if the error is systematic. If the error is random, then it is expected that the error will cancel during the addition process due to the different positive and negative signs associated with the random error. Three possible sources of error have been identified: different microphone phase characteristics, calibration error, and data acquisition sampling time delay. The first two sources cause random error and therefore, may be neglected. The last possible source results in a systematic error that needs to be checked by computing a change in phase angle given by $\Delta\theta = 2\pi f\tau$ at a particular frequency. The time delay (τ) is based

on the total sampling rate of the acquisition board during the experiment, which was 384000 Hz for all 64 channels. Therefore, for a normalized frequency of $f(2H)/U_\infty = 0.20$, the phase change is 0.0014 radians. Figure 3.20 shows a phase angle plot for the normalized frequency $f(2H)/U_\infty = 0.20$ with the $\Delta\theta$ subtracted out of the angle before the addition process. This plot illustrates the effect of the error, which is very small, on the phase angle distribution due to multiplexing the data acquisition system for the microphones. The convection velocity can be recalculated for the new “error-free” phase angle plot, it was determined to be 55.2% of free stream velocity compared to 55.1% of U_∞ computed from the phase plot without accounting for the acquisition time delay. The difference is 0.1% of U_∞ , which is considerably small and therefore, the systematic error due to microphone sampling was neglected in the phase angle analysis.

in

th

ba

co

Th

me

the

ups

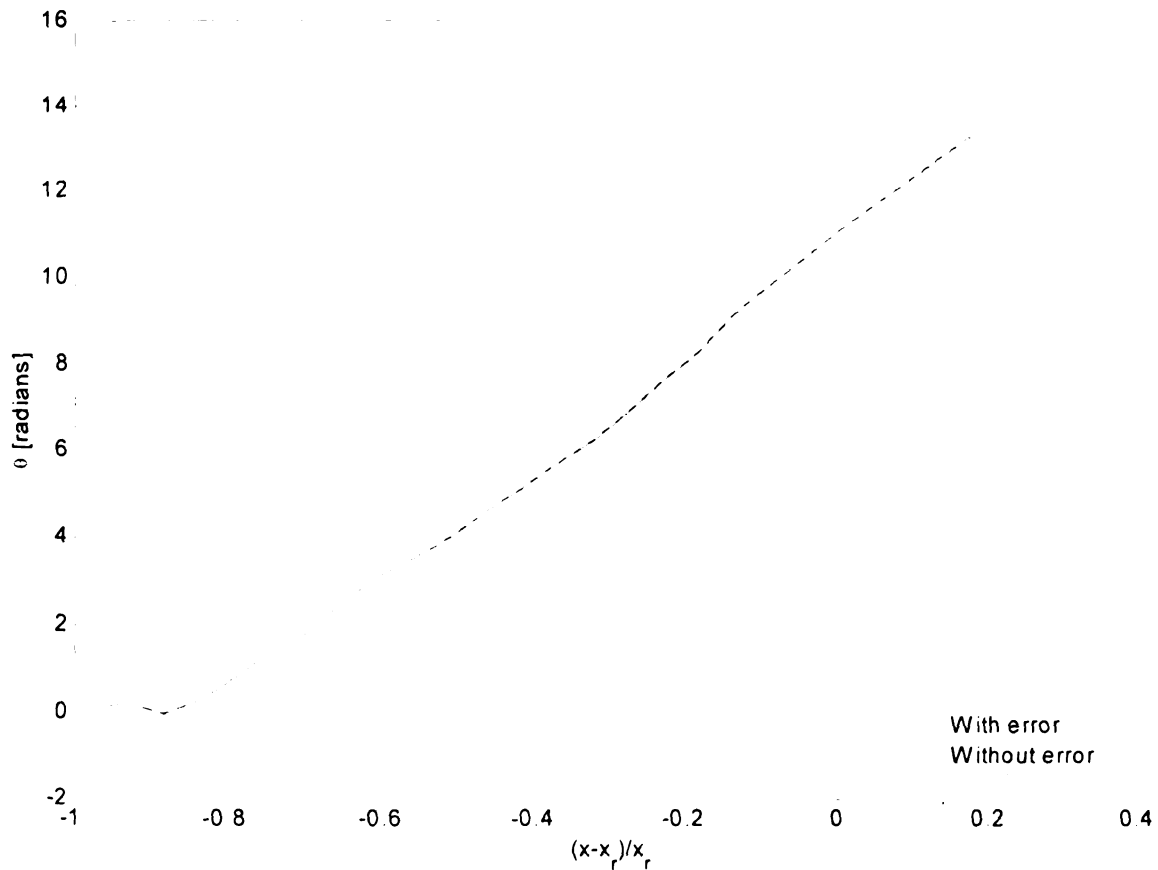


Figure 3.20 Phase angle plot at $f(2H)/U_\infty = 0.2$ with and without phase angle change due to systematic error

At $f(2H)/U_\infty = 0.13$ in Figure 3.19, the phase drops below zero. This is indicative of an upstream convecting velocity. Heenan and Morrison (1998) is the only other investigation reporting negative phase angles, in their study of a backward-facing step. Lee and Sung (2001) mention the idea of an upstream convecting velocity but found no evidence of this phenomenon in their study. The largest negative phase angle at $f(2H)/U_\infty = 0.13$ is found roughly around microphone #5, which is a $\frac{1}{4}$ of the way to reattachment. Interestingly, this is in the region identified earlier in both the RMS and the auto-correlation results, upstream of the transition region.

In the case of $f(2H)/U_\infty = 0.03$, which corresponds to the low-frequency peak identified in the power spectra, the phase angle drops below zero but has a maximum negative peak farther downstream of microphone #5. The peak is located near microphone #7. This indicates that the upstream convection velocity seen in the region spanning from the fence to microphone #5 at frequency $f(2H)/U_\infty = 0.13$ extends farther downstream to microphone #7 at frequency $f(2H)/U_\infty = 0.03$. Therefore, flow structures at very low frequencies can be seen, as evidenced by the phase plot, convecting upstream starting from a distance $x/x_r = 0.35$ downstream of separation. It is not clear if this could be associated with the flapping of the shear layer, which has been hypothesized to correspond to the low-frequency peak in the spectrum by various authors including Castro and Haque (1987).

To explore the convective characteristics of the surface pressure around $x/x_r = 1/4$ further, the cross-correlation function for all 28 microphones relative to microphone #5 was calculated and plotted in Figure 3.21. The abscissa is the distance along the splitter plate with respect to the reattachment point. The ordinate is the time shift normalized by the free stream velocity and the total fence height, and the color bar represents the cross-correlation magnitude.

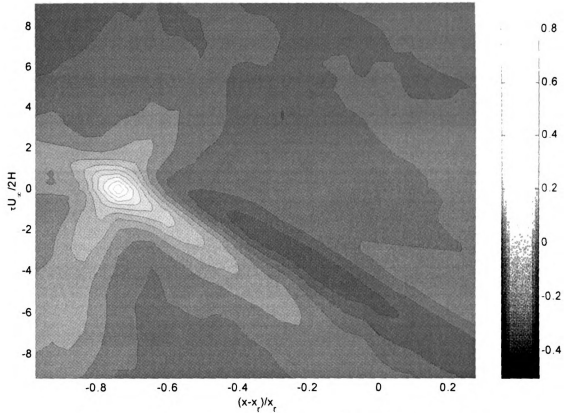


Figure 3.21 Cross-correlation color contour plot for all 28 (reference microphone at $x/x_r = 0.26$)

From the contour plot, an inclined positive peak is found on either side of the high correlation coefficient peak at microphone #5. These two peaks have opposite signed slopes with respect to each other. This is evidence that there are two convecting velocities: one upstream and one downstream as also deduced by Heenan and Morrison (1998) from the phase measurements. The present study is the first to depict the upstream convection from the space-time correlation function. Figure 3.22 shows the same results as in 3.21, but after low-pass filtering the pressure signals up to $f(2H)/U_\infty = 0.15$ in order to concentrate on the lower frequencies only. This was done to see if the

registration of the upstream convection velocity in the cross-correlation map would be enhanced (since the negative phase angle is only seen for the lowest frequencies in Figure 3.19). The axes in Figure 3.22 are the same as in Figure 3.21.

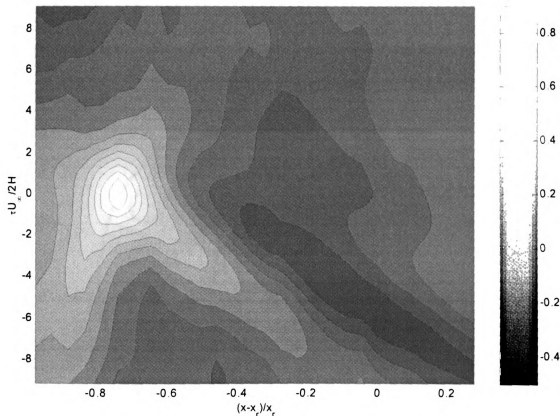


Figure 3.22 Cross-correlation color contour plot for all 28 (reference microphone at $x/x_r = 0.26$) – filtered data

The contour plot in Figure 3.22 also shows the positive inclined lobe associated with the upstream convecting velocity of frequencies up to $f2H/U_\infty = 0.15$. It also illustrates that these lower frequencies still contain downstream convecting motions. This gives evidence that the flow structures that are more dominant farther downstream from microphone #5 (those corresponding to the



power spectrum peak at $f(2H)/U_\infty = 0.1$) are detectable as early as microphone #5. To check for the earliest manifestation of the downstream convecting motion, the cross-correlation map is obtained for all 28 microphones relative to microphones#0. These data, shown in Figure 3.23, are unfiltered; and the axes are the same as in the previous two figures.

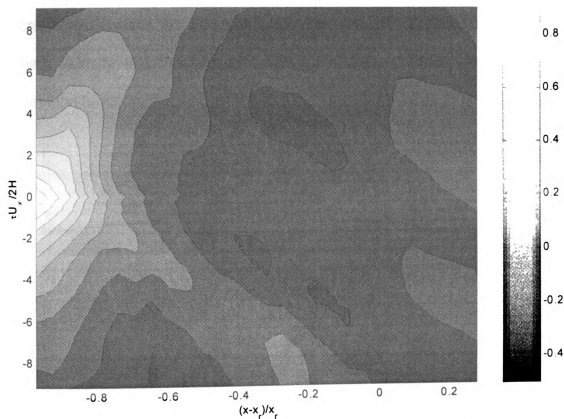


Figure 3.23 Cross-correlation color contour plot for all 28 (reference microphone at $x/x_r = 0.023$)

The cross-correlation results in Figure 3.23 reveal that the downstream convecting velocity begins roughly around the $1/4x_r$ distance, as evidenced by the negative-inclined peak that starts at this position. Upstream of $1/4x_r$, there is no negative-inclined lobes indicating a downstream convecting velocity. Therefore,

it is reasoned that the flow structures seen to dominate the measurements downstream are first noticeable in the surface pressure measurements around the $\frac{1}{4}x_r$ distance.

Cutting the cross-correlation contour plot from Figure 3.22 in the vertical direction yields the individual cross-correlation plots for each microphone relative to microphone #5. These plots are shown in Figure 3.24 for the first twelve microphones, where the abscissa gives the time shift normalized by the free stream velocity and the total fence height and the ordinate gives the cross-correlation function.

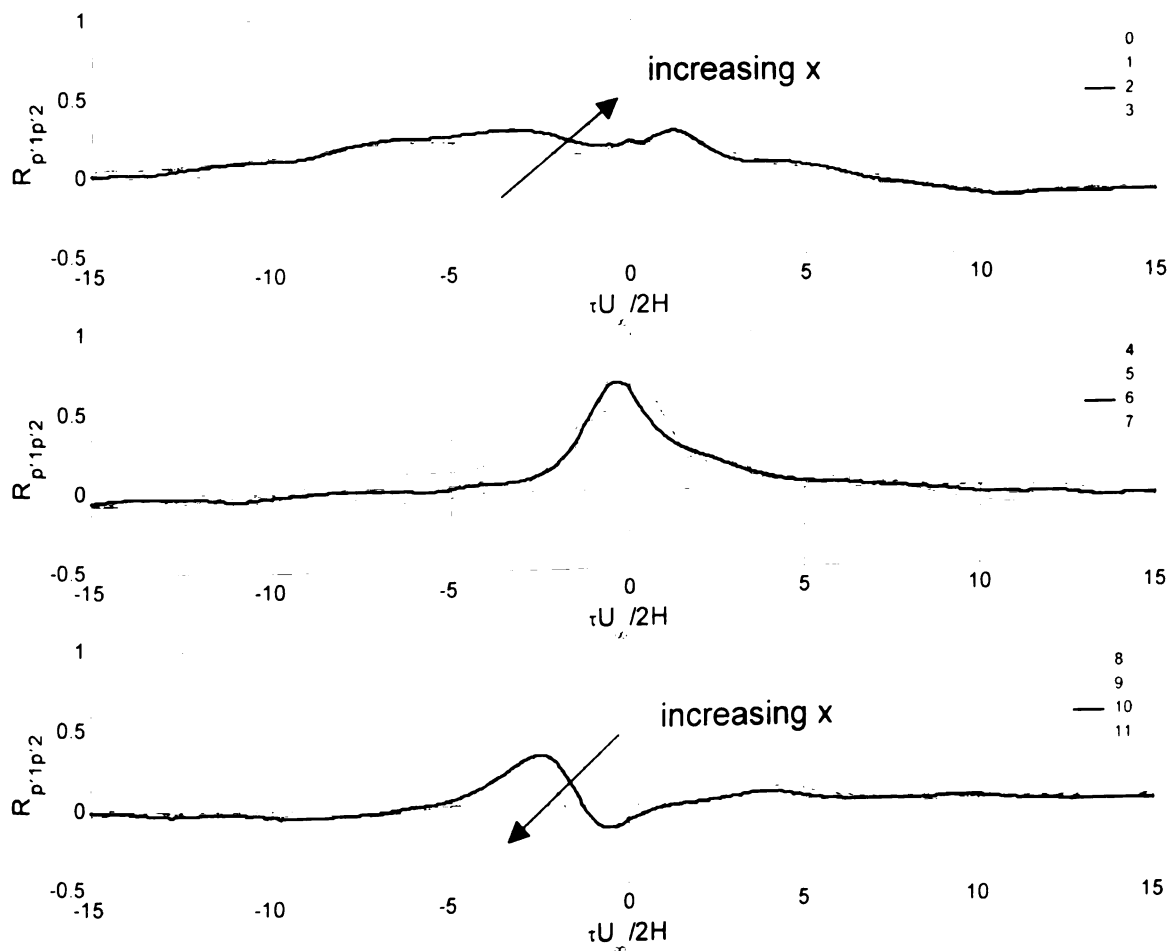


Figure 3.24 Individual cross-correlation plots for the first 12 microphones (reference microphone $x/x_r = 0.26$) – filtered

In Figure 3.24, the top plot shows the graphs for the microphones upstream of microphone #5, while the bottom plot shows the cross-correlation of the microphones downstream of the reference microphone #5. The middle plot contains results for microphones that are located both downstream and upstream in the vicinity of microphone #5. The plots show the split in the convecting nature of the flow structures on either side of microphone #5. Up to microphone #5, the flow structures are traveling at an upstream convecting velocity and beyond microphone #5, the flow structures are convecting at a downstream velocity. This is manifested in the plots by the shift in the correlation peak (marked by arrows in the figure) towards zero time delay with increasing (decreasing) x position upstream (downstream) of microphone #5. The upstream convecting velocity was calculated in the same fashion as done earlier for the downstream convection velocity using a linear fit to the data shown in Figure 3.25.

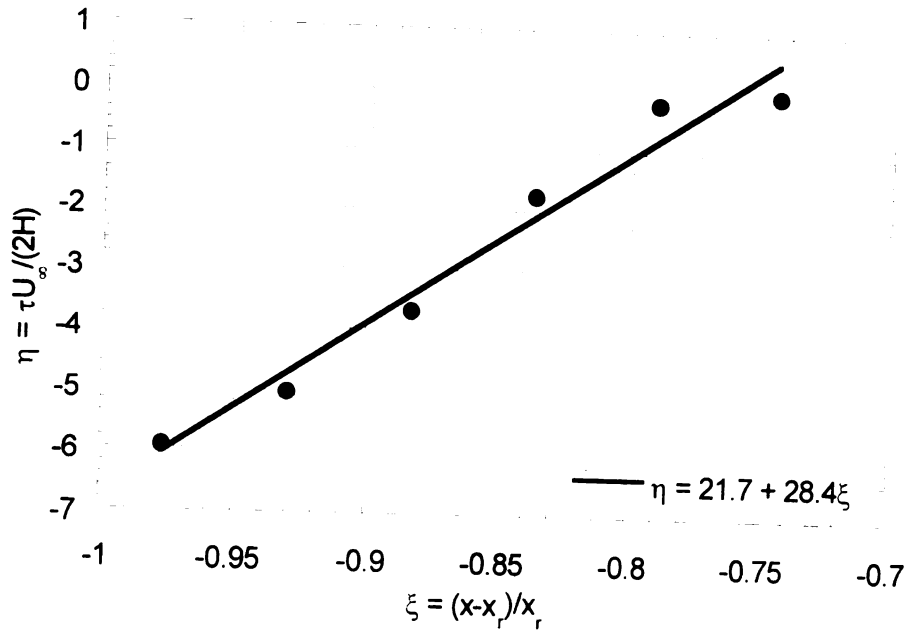


Figure 3.25 Plot of positive-inclined-lobe peak locations from contour map in Figure 3.22

The upstream convecting velocity was determined to be 21% of the free stream velocity. This is similar to the value determined by Heenan and Morrison (1998). Their value was about 20% of the free stream velocity. The downstream convecting velocity was calculated to be 41% of U_∞ for the filtered data and 47% of U_∞ in the unfiltered data. An interesting point is that it seems as though the average convection velocity is not strongly dependent on frequency near microphone #5, as evidenced by the two cross-correlation plots and the calculated convecting velocities. Whether using only low frequencies or using all frequencies to determine the average downstream convecting velocity, the difference between the two speeds is relatively small, leaving only a 6% of U_∞ discrepancy.

The region up to $\frac{1}{4}x_r$ contains the re-separation region as described in Ruderich and Fernholz (1986). They observed this using oil-flow patterns on the splitter plate, revealing a spanwise streamline around $2.3h_f$ downstream of the fence. Spazzini *et al.* (2001) determined the re-separation region to be in the range of $0.2-0.4x_r$ downstream of separation using two methods (forward flow probability and skin friction measurements) at four different Reynolds numbers. Their results also showed that the re-separation point is Reynolds number dependent. Therefore, beneath the shear layer there are two opposing re-circulating flows: the main re-circulating region and a secondary re-circulating bubble just behind the fence. Because the two are in close proximity to one another, they may interact creating a secondary internal shear layer because of their different circulation. Disturbances created from the instability of such an internal shear layer would convect in the local flow direction between the main re-circulating flow and the smaller secondary re-circulating bubble. This offers a plausible explanation for the upstream convecting velocity seen within the $\frac{1}{4}x_r$ region. Heenan and Morrison (1998) attributed the upstream convecting velocity to the main re-circulating flow. They did not, however, elaborate on how the re-circulating bubble would produce a surface pressure signature reminiscent of that of a traveling disturbance. Also, they do not discuss why this signature would be detected upstream but not immediately beneath the main re-circulating flow.

One final point worth mentioning is the dependence of the convection velocity on x as evidenced by the increasing of the convection velocity in the

downstream direction. Close behind the fence, the downstream convection speed was determined to be 47% of the free stream velocity; whereas, near reattachment it was calculated to be 57% of U_∞ . Heenan and Morrison also noticed this trend in their impermeable backward-facing step. Upstream near the fence, they observed a $0.5U_\infty$ convecting velocity that increased to $0.6U_\infty$ close to reattachment and continued to rise farther downstream.

3.8 Inviscid Analysis on Vortical Structures in the Shear Layer

As seen from earlier discussions, the vortical structures within the shear layer convect downstream at a particular propagation speed, which increases with downstream distance. It is also known that the shear layer bends towards the wall and reattaches at some point downstream of separation. Therefore, these vortical structures within the shear layer move closer to the wall as they approach reattachment. Applying a potential flow analysis, it may be theorized that the vortices in the shear layer aid in the reattachment process. This analysis, however, does not explain the increase in convection speed observed with downstream direction, which may be the result of another unknown phenomenon.

In the case of potential flow associated with a rotating cylinder near a wall with no free stream velocity, the cylinder pushes fluid between itself and its image cylinder, causing the cylinder to accelerate towards the wall. Analogous to this phenomenon, as the flow vortex and the image vortex move closer to each other, the velocity of the flow between the two vortices increases, creating a low-pressure region between the vortex and the wall. Thus, above the vortex, there is a higher-pressure region. The pressure difference over the vortex causes the vortex within the shear layer to accelerate towards the wall as in the rotating cylinder case. Therefore, vortices in a shear layer would result in a shorter reattachment length compared to the reattachment length of a shear layer, theoretically speaking, with no vortical structures. This is not to say that

this inviscid mechanism is the only reason the shear layer moves towards the wall, but it may contribute to its reattachment.

Support for this idea may be reasoned from experimentation with forced flows. Kiya *et al.* (1999) found that exciting the flow, or rather adding energy to the turbulent structures in the shear layer, using a woofer embedded in a blunt-faced splitter plate near separation, decreased the reattachment distance. This could be explained as the added energy increased the energy of the turbulent structures, causing the vortex above the wall and its image vortex to spin faster. The increased acceleration of the flow between the two vortices would create an even lower pressure region and a larger pressure difference across the vortex above the wall. As a result, there would be an increase in the acceleration of the vortex towards the wall, resulting in the shorter reattachment length measured by Kiya *et al.* (1999).

4 CONCLUSIONS AND FUTURE WORK

The outcomes from the study are summarized and suggestions for future work are given in the following sub-sections. Both static pressure and unsteady surface pressure measurements were analyzed. PIV measurements will be analyzed in future papers.

4.1 Conclusions

The surface-pressure and velocity field of the structure within the separating/reattaching flow region of a splitter-plate-with-fence configuration were measured using simultaneous wall-pressure array and PIV. A comprehensive database was compiled using an 80-microphone array embedded in the wall of the splitter plate along with a PIV system focused on the centerline plane perpendicular to the splitter plate. Only the time-averaged space-time statistics of the surface pressure measurements have been presented in this paper. In general, the results from this spatio-temporal analysis compared well with available literature in related, but not exactly similar flow geometries.

A splitter-plate-with-fence model was designed and constructed in order to complete the study. The fence had a step height, h_f , of 8 mm, a total fence height, $2H$, of 35 mm, and was attached upstream perpendicular to the splitter plate. The plate measured $160h_f$ in length with microphones spaced $1.2h_f$ apart, starting at $0.6h_f$ from the fence and spanning $33h_f$ in the streamwise direction. In the spanwise direction, microphones covered a distance of $25h_f$. Endplates were

positioned on the sides of the splitter plate, resulting in an aspect ratio of 36. Static pressure taps were also placed on the splitter plate for characterization of the mean flow surrounding the model.

The mean pressure distribution in the streamwise direction was used to determine the reattachment length ($25.8h_f$) based on a comparison with similar results from Castro and Haque (1987). Spanwise distribution of C_p (mean pressure coefficient) values showed good two dimensionality of the mean flow. However, the spanwise distribution of RMS pressure fluctuations indicated the existence of three-dimensional effects that were particularly significant near the sidewalls. In the streamwise direction, there was a rise in C_p , indicating the start of 'transition' (formation of vortices in the shear layer) around $\frac{1}{4}x_r$, in the RMS pressure values with the peak value occurring in the vicinity of reattachment.

The region extending up to $\frac{1}{4}x_r$ was also identified in the auto-correlation function analysis, which showed decreasing time scales with downstream distance. The $R_{p,p'}$ contour plot revealed that upstream, within the $\frac{1}{4}x_r$ region, the surface-pressure signature was dominated by large time scales; and farther downstream, near reattachment, smaller time scales were prominent in the wall-pressure measurements. Transition between the two different time scales occurred in a region extending from $0.25x_r$ to $0.7x_r$. Integral time scale (τ^*) analysis shows long time scales of $\tau^*U_\infty/2H = 36.7$ in the region stretching from the fence to $0.25x_r$ and shorter time scales ($\tau^*U_\infty/2H = 6.8$) in a $0.6x_r$ range around the mean reattachment point. The inverse of these timescales ($f = 1/\tau$) gives approximately the peak frequency values determined in the power spectra.

The peak energy in the power spectra for microphones close to the fence is concentrated at very low-frequencies ($f(2H)/U_\infty = 0.02 - 0.03$), which has been attributed by many researchers to the 'flapping' of the shear layer. Farther downstream near the mean reattachment location, the concentration of peak energy in the power spectra is seen at a higher frequency ($f(2H)/U_\infty = 0.1$), relating to the highly turbulent structures within the shear layer. The findings from the auto-correlation function and power spectra analyzes were consistent.

From the cross-correlation function analysis, with respect to a reference microphone located closest to reattachment, the wall-pressure signature of the downstream convective motion of shear-layer structures, described by Cherry *et al.* (1984) amongst others, was found to travel at a convection velocity of $0.57U_\infty$. Phase angle information, obtained from the cross-correlation of the signal between neighboring pairs of microphones and constrained to frequencies up to $f(2H)/U_\infty = 0.3$ (range of high signal coherence), revealed an upstream convecting velocity of $0.21U_\infty$ at low frequencies within the $1/4x_r$ region. A cross-correlation contour plot, based on a reference microphone located near $1/4x_r$, showed the two opposing convection velocities and provided evidence that the earliest detection of the downstream-traveling turbulent structures seen near mean reattachment was around $1/4x_r$. It has also been theorized that a secondary shear layer forms from the velocity gradient between the re-circulating region and the secondary re-circulating bubble residing in the $1/4x_r$ region. This secondary shear layer could become unstable, developing vortical structures that convect

upstream giving reason to the upstream propagation velocity seen in the cross-correlation function contour plots.

Overall, two distinctive regions emerged from the spatio-temporal analysis of the surface pressure measurements in both the time and frequency domains. Upstream, from the fence to $\frac{1}{4}x_r$, the surface-pressure signature was dominated by large time scale disturbances and an *upstream* convecting velocity of $0.21U_\infty$. Beyond the $\frac{1}{4}x_r$, turbulent structures with small time scales and a downstream convection velocity of $0.57U_\infty$ generated most of the pressure fluctuations.

4.2 Future Work

There is still extensive work to be done on the sizeable database collected, including an instantaneous analysis on the surface pressure measurements as well as on the PIV images acquired. The results of these can be utilized in the development of low-dimensional models for predicting the flow state above the surface from wall-pressure measurements. The PIV data will also be used to determine the actual reattachment point more precisely from the flow streamlines, which can be compared to the x_r approximated from the average C_p^* value at reattachment. Additionally, the flow state surrounding the splitter-plate-with-fence geometry needs to be characterized in even greater detail.

Unanswered questions remain about where the roll-up of vortical structures begins, whether there is a secondary reattachment point on the fence as suggested by Spazzini *et al.* (2001), and what type of activity persists in the

$\frac{1}{4}x_r$ region containing the secondary separation point and re-circulation bubble. More detailed measurements within that $\frac{1}{4}x_r$ region may provide some answers. It would also be interesting to instrument the fence at the front face and in the back with static pressure taps and surface pressure sensors to detail the flow characteristics in terms of the stagnation point and the possible secondary reattachment point. Finally, further analysis is needed to determine if the source of the upstream convection velocity, seen in the $\frac{1}{4}x_r$ region, is traveling structures within a secondary shear layer; PIV images may be able to provide this information.

APPENDIX A: Microphone Coordinates

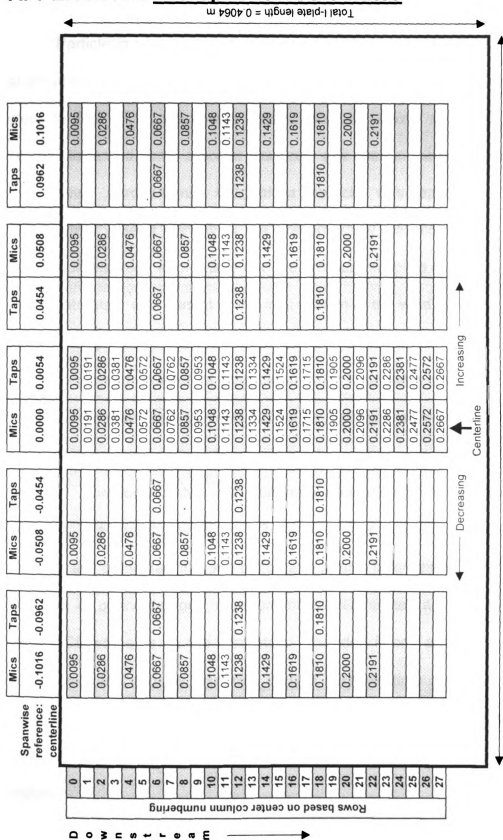


Figure A.1: Microphones and static pressure tap dimension spreadsheet (all dimensions are in meters) - streamwise dimensions reference upstream edge of I-plate to center of microphone or tap hole and spanwise dimensions reference centerline of I-plate to center of microphone or tap hole (Mics = microphones and Taps = static pressure taps)

APPENDIX B: Particle Image Velocimetry

Particle image velocimetry (PIV) measures two-velocity field components at a number of points in a plane (Humphreys *et al.* (2001)). There are four basic steps to PIV. First, the flow is seeded; bis(2-ethylhexyl) sebacate, also called DEHS, dispersed using a six-jet atomizer, was used in the present experiment. The mean aerodynamic size of a particle was approximately 0.9-1.0 micrometers. Seed density in the present study was controlled through the number of jets used at one time and the pressure supplied to each individual jet. The jet atomizer was placed at the inlet section of the wind tunnel, thus allowing the incoming flow to carry the seed into the test section. The seed must be evenly dispersed as best as possible in order to obtain useable images. If the seed is too dense, then particles cannot be distinguished from one another; and if the seed is sparse, then there will not be enough particles to complete the analysis. The second step is to illuminate the particles in the flow region being studied. The illumination is from 2 Nd: YAG laser systems. Beams from the systems are combined through optics and form a laser sheet that is focused in the area of concentration. A record of this illuminated area is then captured using CCD cameras as the third step. The idea is one of the laser beams is pulsed and an image is captured, then at a known time delay the other laser beam is pulsed and another image is taken. Within the minute time delay, the particles in the flow have moved slightly, but not out of view of the illuminated region.

The PIV records acquired are stored and analyzed to create a velocity vector field of the flow. The analysis requires locating the particles in one image and matching them with the particles in the time-delayed image. The particles are matched by taking a small interrogation window (e.g., 16 by 16 pixels) and calculating a two-dimensional cross correlation. The off-set between the two images at which the highest correlation is found gives the average particle displacement. The distance the particle moved is then determined in the x direction. Knowing the distance the particles moved over a period of time allows for the calculation of the velocity term. The direction of the flow is also known depending on which way the particles shift. Figure B.1 shows an example of a PIV system set-up.

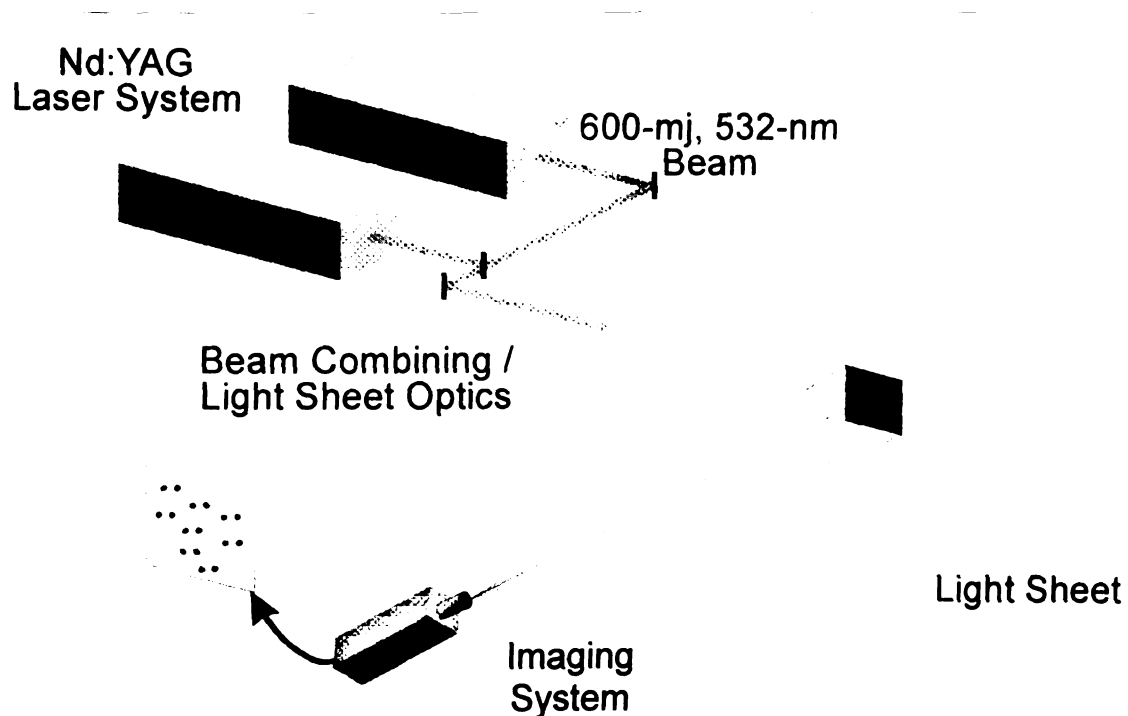


Figure B.1 Example of set-up for a typical PIV system [Humphreys 2000]

B.1 Experimental Set-up

The PIV system used in this study was composed of two lasers, four cameras, and optical equipment components. The two lasers were ND:YAG from the Continuum Powerlite series. Each laser was capable of producing up to 600 mJ per pulse of green light (wavelength of 532 nm) at a nominal frequency of 10 Hz. The nominal pulse width for both lasers was 10 ns, and they were pulsed in synchronization with a 40 μ s separation between the lasers. The laser-lit particles were captured by four Hitachi (KP-F100) CCD cameras. Each camera had a detector size of 1300 pixel wide by 1030 pixel high with a pixel size of $6.7\mu^2$ with a 100% fill, meaning no gap between pixels. The four cameras, shown in Figure B.2, were used to obtain simultaneous PIV measurements over two planes that overlapped partially (about 1/8th of the image width). This enabled coverage of most but not all of the streamwise extent of the separating/reattaching flow region.

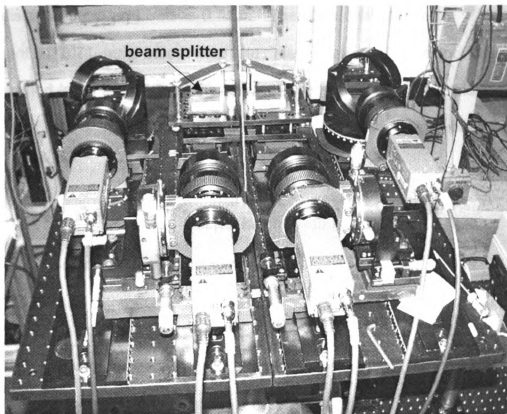


Figure B.2 Camera set-up used in experiment

Measurements over each plane were accomplished using two cameras in cross-correlation mode. The two cameras were made to image the same plane using a polarizing beam splitter (Figure B.2). The beam splitter allowed scattered laser light with vertical polarization to go to one of the cameras but not to the other. The opposite camera captured images from a horizontally polarized laser beam. Therefore, by polarizing one of the laser beams in the vertical plane and the other in the horizontal plane, it was possible to acquire two images of the particle seed, one by each camera separated by $40\ \mu\text{s}$.

The $40\ \mu\text{s}$ was determined based on the pixel size, the magnification factor, and the PIV equation. The CCD size is 1300 pixels by 1030 pixels and

the distance between pixels is 6.7 μm . Therefore, the total height of the CCD element is 8.71 mm, also called the image view. The field of view was determined to be 99 mm from the ruler calibration process to be explained later. From the field of view and the image view, the magnification can be calculated as follows:

$$\text{Magnification} = \frac{\text{image height (width)}}{\text{object height (width)}} = \frac{8.71 \text{ mm}}{99.06 \text{ mm}} = 0.088. \quad (\text{B1})$$

The PIV equation is defined accordingly

$$\bar{V} = \frac{\bar{d}}{m\Delta T} \quad (\text{B2})$$

where vector V represents the speed in meters per second, vector d represents the vector displacement in μm , m is the magnification, and ΔT is the laser pulse separation in μs . A 64 by 64 interrogation box was used for the cross correlation and the maximum displacement was 8 pixels, or 12.5% of the interrogation window width. This was less than the maximum 25% displacement recommended by Adrian (1991). Eight pixels equal 53.6 μm and the test speed was 15 m/s. Using the PIV equation and solving for ΔT , the laser pulse separation was calculated to be 40 μs .

The optics used to change the polarization of the lasers, form the light sheet, and direct the beam into the test section consisted of a variety of components. Turning mirrors, from CVI Laser Optics (Y2-2037-45-UNP), were used to redirect the path of the two lasers. The mirrors were 50.8 mm in diameter with 9.5 mm thickness, allowing a wavelength of 532 nm to pass through with a minimum un-polarized reflectance of 99%. This means that 99%

of the laser light received by the mirror is reflected, resulting in 1% loss of energy, but the mirror does not affect the polarization of the beam. A $\lambda/4$ waveplate from Newport was used to rotate the polarization of one of the beams before combining at the thin, film-plate polarizer. The combined beams had perpendicular polarization with respect to each other. The CVI Laser Optics thin, film-plate polarizer (TFP-1053-PW-2025-C) had a transmission efficiency of 95% at a wavelength of 1053 nm. Two BK7 rectangular singlet lenses, cylindrical plano-concave from CVI Laser Optics were used to widen and lengthen the laser sheet. One of the lenses has a focal length of -38 mm and was used to control the height of the laser sheet. The other lens, with a focal length of -50 mm, was used to determine the width of the laser sheet. The spherical bi-convex lens from Newport had BK7 optical glass, a focal length of 250 mm, and a diameter of 50.8 mm. It was used to limit the width of the laser sheet in the z direction and the height in the y direction and focus the laser sheet on the model. Finally, an airfoil with a turning mirror embedded on its surface was placed in the tunnel downstream of the model in order to turn the laser beam upstream, towards the measurement region behind the fence. Figure B.3 shows the optics set-up for the PIV system.

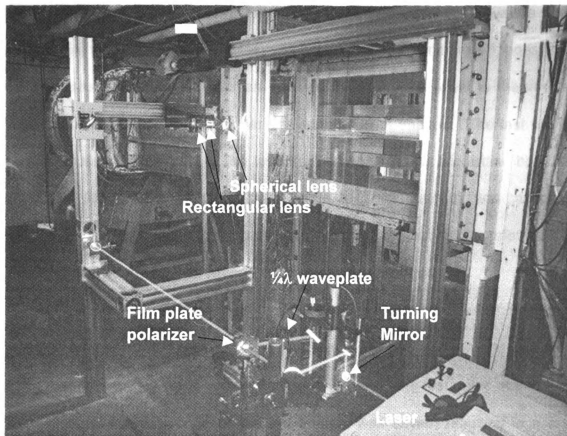


Figure B.3 Optics set-up used for PIV system

B.2 Experimental Procedure

Synchronization of Microphone and PIV

A master pulse generator (Stanford Research Systems (SRS) 535) produced a 10 Hz TTL pulse train that was used to run the lasers continuously and to provide the primary synchronization signal for the PIV and microphone systems. This signal was sent to the external trigger input of a second 'slave' SRS 535 unit. External triggering of the slave unit was disabled until a button on the front panel was manually pressed. When the button was pushed, three different 5V pulse train outputs were generated from the slave pulse generator in

100

1
2
3
4
5
6
7
8
9
10
11
12
13
14
15
16
17
18
19
20
21
22
23
24
25
26
27
28
29
30
31
32
33
34
35
36
37
38
39
40
41
42
43
44
45
46
47
48
49
50
51
52
53
54
55
56
57
58
59
60
61
62
63
64
65
66
67
68
69
70
71
72
73
74
75
76
77
78
79
80
81
82
83
84
85
86
87
88
89
90
91
92
93
94
95
96
97
98
99
100

synchronization with the master SRS 535 signal. The first output was a non-inverted 5V that went to all four frame grabbers to capture and store images from the cameras. The second was an inverted 5V signal that went to the vertical drive on all four cameras to trigger the acquisition of images. The last output was an inverted 5V signal to the last channel on the data acquisition board in order to record the camera pulse train. This channel was acquired simultaneously with the microphones and provided the necessary reference to identify the points in time at which PIV images were captured.

Typically, microphone data acquisition was started 2-3 seconds before pressing the external trigger button on the slave SRS 535 unit. Once this button was pressed, images were acquired starting with the very first pulse at a rate of 10 Hz. However, only one of the ten images was saved, resulting in a one image/second PIV acquisition rate for a total of 20 images per microphone time series. For each image, the first laser was Q-switched (output) after a few microsecond delay of receiving the rising edge of the master pulse signal. The second laser was Q-switched 40 microseconds later. The 40-microsecond laser pulse separation was checked using a photo diode with nanoseconds rise time and a wide bandwidth oscilloscope. Meanwhile, the camera exposure time started at the falling edge of the inverted slave pulse train (the same time as the rising edge of the master pulse train). The shutter opening time was one millisecond, which was much greater than the 40-microsecond delay between the lasers. This ensured that both lasers fired once while the cameras were open, generating the two images for PIV processing. A number of preliminary

checks were conducted before collecting PIV data including dot card, ruler, background, and zero separation pulse as described below.

Dot Card

The dot card was used in the alignment of the four cameras. Each of the two pairs of cameras constituted a unit, and each unit provided a single vector field. Two units were used because the reattachment area was too long for one unit (i.e., single view) to capture it. By using all four cameras the field of view was almost doubled. Each pair of cameras had to be aligned with respect to each other to ensure that both cameras captured the same field of view. Then the two units had to be adjusted so that one unit captured one area and the other set captured the adjoining area. The field of view for the two units overlapped by 12.7 mm, ensuring that no gap between the two views and enabling a smooth transition in between the vector fields.

The flow region of interest was divided in two overlapping sections as shown in Figure B.4: upstream and downstream. At the upstream position, one unit was placed so that the field of view spanned a distance of 185 mm, which is the total length captured by the two camera sets (how the total length was determined is covered in the next section) in the downstream direction. In this field of view, the measurements in front of the fence were recorded. At the downstream position, one unit was positioned so that the field of view captures the edge of the last microphone; hence, a total distance of 185 mm was imaged upstream. Overall, because of the overlap, the region of interest was divided in thirds in order to record the whole field of interest.

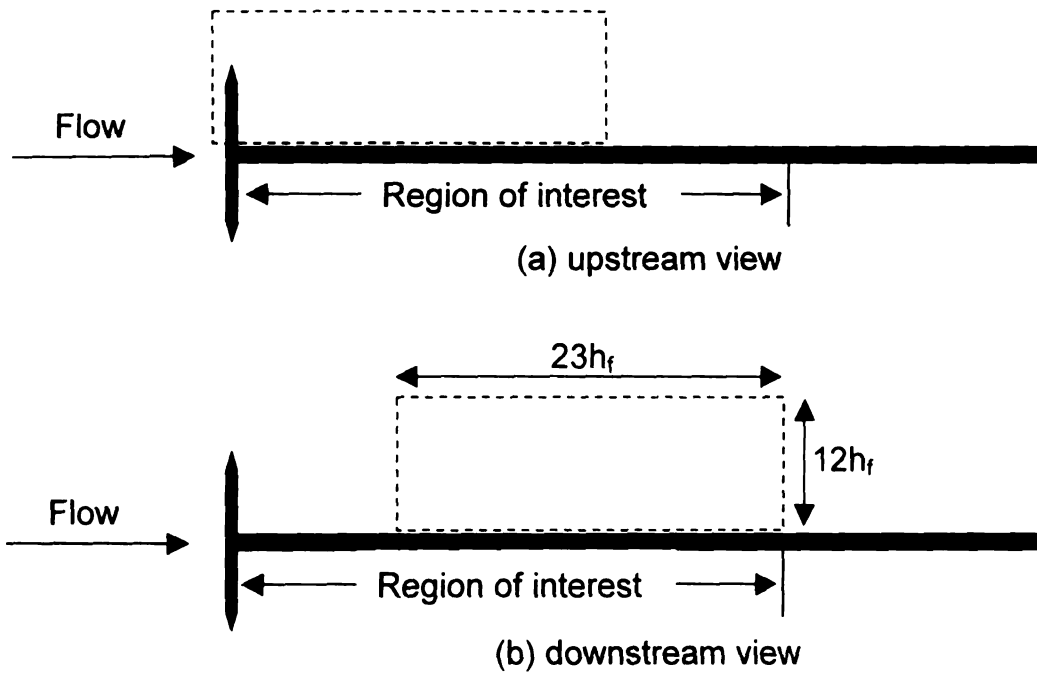


Figure B.4 Flow regions captured by the two camera positions used

In order to align the cameras, the left side of a dot card positioned upside-down (Figure B.5) was placed at the edge of the last microphone (#27) in the downstream position.

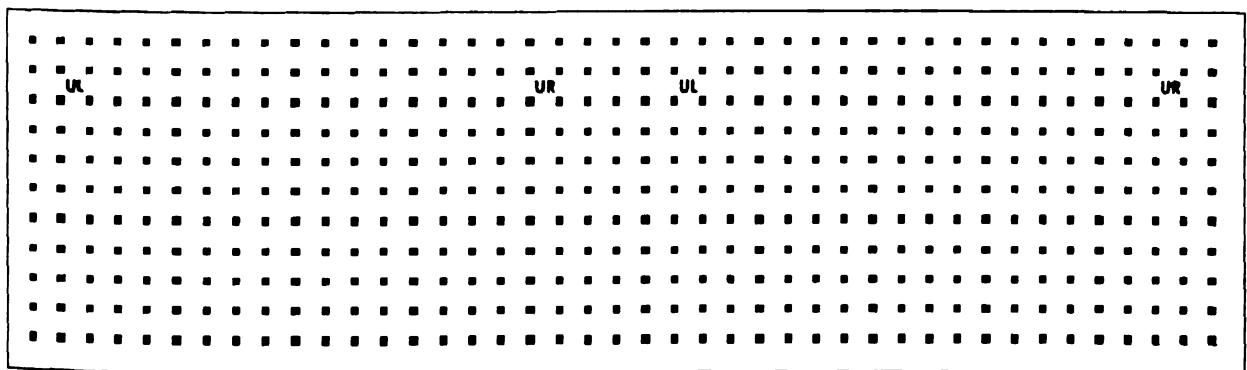


Figure B.5 Sample of the dot card used to align the two pairs of cameras

On the dot card, there was a circled UL marker that indicated whether the two cameras were seeing the same rows and columns of dots. The dot pitch spacing was 5.7404 mm. This was the average spacing between dots and was measured with a precision ruler. The two cameras were adjusted such that the dots were parallel to the sides of the PC screen. An alignment program, written by William Humphreys, was then used to align the dots between the two cameras by subtracting the images from the camera pairs in each unit. Theoretically, the screen should be consistently black or white, meaning the dots line up on top of each other. Once this alignment was achieved, then there was good confidence that the cameras were taking a picture of the same area. The two center cameras were aligned so there was $\frac{1}{2}$ " overlap on the dot card with respect to each other. Therefore, when processing the data, all four cameras should see the same $\frac{1}{2}$ " area and produce the same velocity vectors in this same overlap area. To figure out the exact overlap, the UL in the right and left cameras should be located. The images should then be shifted pixel by pixel until the two ULs line up perfectly with each other. The number of shifted pixels translates to the amount of overlap.

Ruler

The ruler was used to calibrate the field of view of the cameras in order to determine the physical units per pixel. To do this, a lab ruler was placed in the field of view (Figure B.6) and the tick marks were counted.

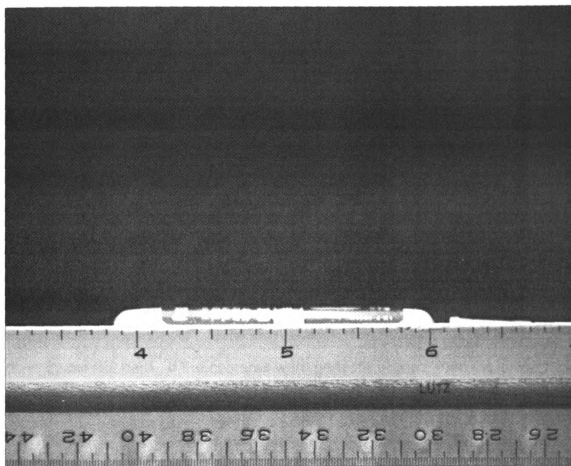


Figure B.6 Image of ruler used in calibration of PIV system

The measurement recorded was about 99.06 mm within the camera range, 0.0762 mm per pixel. With two cameras, the distance captured in one position was 185.42 mm and the total width of interest was 258.8 mm. Therefore, the cameras had to be moved to two positions in order to capture the whole reattachment area, as previously discussed.

Background Run

A 'background run' was also done of the zero-pulse separation with no seed. Five runs were recorded. These will be averaged and subtracted out pixel

by pixel from the recorded images in order to remove any flare in the images from the window and the aluminum splitter plate.

Zero-Pulse Separation

A zero-pulse separation run was recorded as a double check of the dot card. In a zero-pulse separation run, both lasers are fired in unison, while the flow was seeded. As explained by Humphreys *et al.* (2001), this removes motion induced by the flow from the images and leaves only the distortion of the optical field and the camera misalignment as explanation for any movement of particles observed between the PIV image pair. Thus, this is a check on the alignment done by the dot card. If the cameras were perfectly aligned, then the image from one camera should exactly match the image from the other camera. If there is any difference, this indicates misalignment of the cameras. The misalignment can be corrected through data processing technique called piecewise, bilinear dewarping [Meyers *et al.* 1992]. This technique was originally designed for Doppler Global Velocimetry and is effective in removing distortions due to optics and camera misalignment.

APPENDIX C: Microphone Contamination Testing

Microphones were contaminated with DEHS and were compared to 'clean' microphones to determine the change in response of the microphone due to contamination. To contaminate the microphones, each was held near the exit of a six-jet atomizer, filled with the DEHS seed. The microphones were held there for a series of times ranging from 5 to 20 minutes. Calibration of these contaminated microphones was done in the same fashion as described in Section 2.1.3. The results showed that the sensitivity was attenuated in the contaminated microphone compared to an uncontaminated one, but that the frequency response stayed flat up to 6 kHz. However, in the case that the microphones do become contaminated in the PIV runs, a correction to the data can be done by taking the RMS of clean microphones and multiplying the data of the seeded microphones by an RMS to time series ratio. If the microphones do become contaminated, a difference should be seen in the RMS pressure fluctuations. As for the phase, the time delay for uncontaminated microphones was on the order of 10 microseconds, which is relatively small compared to the frequency magnitude of the structures being measured. The time delay for contaminated microphones actually decreased. Therefore, the concern was minimal for the microphone measurements in the event that one or all became contaminated during PIV data collection.

APPENDIX D: Error Estimation for Integral Time scales

In order to estimate the error, it seemed reasonable to assume that the correlation peak can be identified provided that the variation in the correlation function in the vicinity of the peak is larger than the associated data scatter. Since first order variation of a function in the neighborhood of a peak is described by the function second derivative, or curvature, rather than the first derivative (which is equal to zero), the lowest order polynomial describing variation in the vicinity of a peak is that of a parabola. Hence, the equation of a parabola of the form

$$(y - y_0) = C(x - x_0)^2 \quad (D1)$$

was fitted to data points in the vicinity of the negative correlation peak. Figure D.1 shows the parabolic curve for reference.

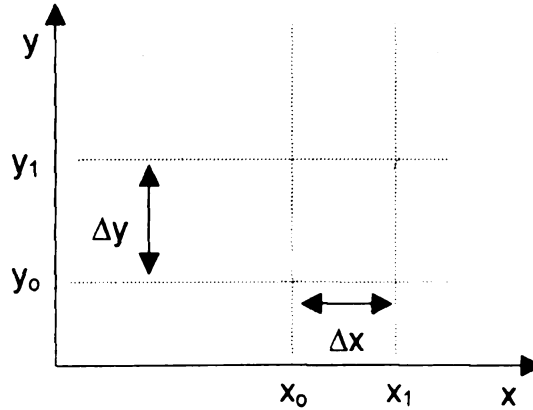


Figure D.1 Parabola

The parabola equation can be rewritten as

$$\Delta y = C(\Delta x)^2 \quad (D2)$$

where C represents one half of the curvature of the parabola. Rearranging the equation yields the error estimate (Δx) in the peak location associated with 'just observable variation' in the parabola (Δy).

$$\Delta x = \sqrt{\frac{\Delta y}{C}} \quad (D3)$$

The Δy error percentage used was 5%, which was slightly larger than twice the RMS of the data scatter surrounding the zero auto-correlation value (i.e., at very large time shift). This percentage accounts for 95.45% of the variation in R_{pp} because of random scatter (assuming Gaussian-distribution error). Therefore, equation (25) states that the error in the location of the peak is equal to the square root of 0.05 divided by half the curvature of the parabola. The more curved the parabola, as seen near reattachment in the auto-correlation plots, the larger C is, and the smaller the calculated error. In the same sense, if the parabola is fairly flat, then the calculated error will be larger because of the smaller C value.

The error was calculated by locating the maximum negative peak in each auto-correlation. Utilizing a polynomial fit function in Matlab, a parabola was then fit to the data using a defined number of points. These points were selected based on an estimate of where the auto-correlation function crossed the abscissa. For the first nine microphones, 420 points were used because the parabola was broad and crossed the abscissa roughly around $\tau U_\infty / 2H = 10$ and 25. For the remaining microphones, 140 points were used between non-dimensional time shift values of 5 and 10. These parabolas were narrower and

had more well-defined negative peaks. The value of C obtained from the polynomial fit function was then used in equation (25) to calculate the error (with Δy set to 0.05 as mentioned above).

BIBLIOGRAPHY

- Adrian RJ** (1991) Particle-imaging techniques for experimental fluid mechanics. *Annu. Rev. Fluid Mech* 23: 261-304
- Arie M; Rouse H** (1956) Experiments on two-dimensional flow over a normal wall. *J Fluid Mech* 1: 129-142
- Castro IP; Haque A** (1987) The structure of a turbulent shear layer bounding a separation region. *J. Fluid Mech* 179: 439-468
- Cherry NJ; Hillier R; Latour MEMP** (1984) Unsteady measurements in a separated and reattaching flow. *J Fluid Mech* 144: 13-46
- Chun KB; Sung HJ** (1998) Visualization of a locally-forced separated flow over a backward-facing step. *Experiments in Fluids* 25: 133-142
- Coller BD; Noack BR; Narayanan S; Banaszuk A; Khibnik AI** (2000) Reduced-basis model for active separation control in a planar diffuser flow. *AIAA paper 2000-2562, AIAA Fluids 2000, 19-22 June, Denver, CO.*
- Corke TC; Glauser MN; Berkooz G** (1994) Utilizing low-dimensional dynamical systems models to guide control experiments. *Applied Mechanics Reviews*, 1994
- Driver DM; Seegmiller HL; Marvin JG** (1987) Time-dependent behavior of a reattaching shear layer. *AIAA J* 25: 914-919
- Eaton JK; Johnston JP** (1981) A review of research on subsonic turbulent flow reattachment. *AIAA J* 19: 1093-1100
- Farabee TM; Casarella MJ** (1986) Measurements of fluctuating wall pressure for separated/reattached boundary layer flows. *J of Vibration, Acoustics, Stress, and Reliability in Design* 108: 301-307
- Fricke FR** (1971) Pressure fluctuations in separated flows. *J Sound Vib* 17: 113-123
- Glauser M; Eaton E; Taylor J** (1999) Low-dimensional descriptions of turbulent flows: experiment and modeling. *30th Annual Fluid Dynamics Conference, June 28 – July 1, 1999, Norfolk, VA*

- Guezennec YG** (1989) Stochastic estimation of coherent structures in turbulent boundary layers. *Phys. Fluids A*, Vol. 1, No. 6
- Hancock PE** (1999) Measurements of mean and fluctuating wall shear stress beneath spanwise-invariant separation bubbles. *Experiments in Fluids* 27: 53-59
- Heenan AF; Morrison JF** (1998) Passive control of pressure fluctuations generated by separated flow. *AIAA J* 36: 1014-1022
- Howerton BM** (1998) Development of a passive horseshoe vortex control device as applied to semi-span wind tunnel testing. Masters thesis. North Carolina State University.
- Humphreys WM** (2000) "Introduction to Particle Image Velocimetry." Presented at the Wind Tunnel University workshop, NASA Langley Research Center
- Humphreys WM; Bartram SM** (2001) Measurement of separated flow structures using a multiple-camera DPIV system. Presented at the 19th International Congress on Instrumentation in Aerospace Simulation Facilities
- Hwang KS; Sung HJ; Hyun JM** (2000) Visualizations of large-scale vortices in flow about a blunt-faced flat plate. *Experiments in Fluids* 29: 198-201
- Kiya M; Sasaki K; Arie M** (1982) Discrete-vortex simulation of a turbulent separation bubble. *J Fluid Mech* 120: 219-244
- Kiya M; Sasaki K** (1983) Structure of a turbulent separation bubble. *J Fluid Mech* 137: 83-113
- Kiya M; Shimizu M; Mochizuki O** (1997) Sinusoidal forcing of a turbulent separation bubble. *J Fluid Mech* 342: 119-139
- Kiya M; Mochizuki O; Kudo D** (1999) Active control of turbulent separated flows. *Proceedings of FEDSM'99*: 1-9
- Lee I; Sung HJ** (2001) Characteristics of wall pressure fluctuations in separated and reattaching flows over a backward-facing step: Part I. Time-mean statistics and cross-spectral analyses. *Experiments in Fluids* 30: 262-272
- Lorber P; McCormick D; Anderson T; Wake B; MacMartin D; Pollack M; Corke T; Breuer K** (2000) Rotorcraft retreating blade stall control. *AIAA paper 2000-2475*, *AIAA Fluids 2000*, 19-22 June, Denver, CO.
- Meyers JF** (1992) Doppler Global Velocimetry – The Next Generation?. *AIAA Paper* 92-3897

Naguib AM; Gravante SP; Wark CE (1996) Extraction of turbulent wall-pressure time-series using an optimal filtering scheme. Experiments in Fluids 22: 14-22

Rivir RB; Sondergaard R; Bons JP; Lake JP (2000) passive and active control of separation in gas turbines. AIAA paper 2000-2235, AIAA Fluids 2000, 19-22 June, Denver, CO.

Roos FW; Kegelmann JT (1986) Control of coherent structures in reattaching laminar and turbulent shear layers. AIAA J 24: 1956-1963

Roshko A; Lau JC (1965) Some observations on transition and reattachment of a free shear layer in incompressible flow. In Proc. 1965 Heat Transfer and Fluid Mech. Inst.

Ruderich R; Fernholz HH (1986) An experimental investigation of a turbulent shear flow with separation, reverse flow, and reattachment. J Fluid Mech 163: 283-322

Saathoff PJ; Melbourne WH (1997) Effects of free-stream turbulence on surface pressure fluctuations in a separation bubble. J Fluid Mech 337: 1-24

Smits AJ (1982) Scaling parameters for a time-averaged separation bubble. AIAA J 104: 178-184

Spazzini PG; Iuso G; Onorato M; Zurlo N; Di Cicca GM (2001) Unsteady behavior of back-facing step flow. Experiments in Fluids 30: 551-561

Willmarth WW; Yang CS (1970) Wall-pressure fluctuations beneath boundary layers on a flat plate and a cylinder. J Fluid Mech 41: 47-80

Wynnanski I (1997) Boundary layer and flow control by periodic addition of momentum. AIAA paper 97-2117. 28th AIAA Fluid Dynamics Conference, June 29-July 2

General References

Munson BR; Young DF; Okiiski TH (1990) Fundamentals of fluid mechanics. New York: John Wiley & Sons, Inc.

Proakis JG; Manolakis MG (1988) Introduction to digital signal processing. New York: Macmillan

White FM (1994) Fluid Mechanics. New York: McGraw-Hill, Inc.

MICHIGAN STATE LIBRARIES



3 1293 02177 4256